UNIVERSITÀ
DEGLI STUDI
DI PADOVA

Tesi di dottorato

Sede Amministrativa: Università degli Studi di Padova

Dipartimento di Biologia

CORSO DI DOTTORATO DI RICERCA IN: BIOSCIENZE E BIOTECNOLOGIE

CURRICOLO: BIOLOGIA CELLULARE

CICLO: XXIX

In silico analysis of membrane transport/permeability mechanisms

Coordinatore: Ch.mo Prof. Paolo Bernardi

Supervisore: Ch.mo Prof. Paolo Bernardi

Co-supervisore: Ch.mo Prof. Silvio C.E. Tosatto

Dottorando: Claudio Bassot

“The true definition of science is this: the study of the beauty of the world. As soon as one thinks about it, it becomes obvious. Matter, blind force are not the object of science. Thought is incapable of reaching out to them; they fly ahead of it. The savant's thought is never able to reach beyond relations in which matter and force are knit into an invisible, impalpable and unalterable pattern of order and harmony. “Heaven's net is vast”, says Lao-Tse; “its meshes are wide; yet nothing gets through.”

Simone Weil, “*The Need for Roots: prelude towards a declaration of duties towards mankind”,* 1949.

INDEX

Abbreviations used

CsA, cyclosporin A

CyP, cyclophilin

ER, endoplasmatic reticulum

IMM, inner mitochondrial membrane

Inw, inward facing

Lip, lipid facing

HMMs, Hidden Markov Models

MSA, multiple sequence alignment

MCU, mitochondrial Ca2+ uniporter

MD, Molecular Dynamics

ns-EVA, non-syndromic hearing loss with enlarged vestibular aqueduct

NSHL, non-syndromic hearing loss

OMM, outer mitochondrial membrane

OSCP, oligomycin sensitivity conferring protein

PDB, Protein Data Base

PM, plasma membrane

PS, pendred syndrome

PSSMs, position-specific scoring matrices

PTP, permeability transition pore

ROS, reactive oxygen species

SLC, Solute Carrier

SDPLP, sensorineural deafness with palmoplantar lichen planus

TM, transmembrane

TSPO, translocator protein of 18 kDa (TSPO)

VDAC, voltage-dependent anion channel

List of publications

1) Bassot C, Minervini G, Leonardi E, Tosatto SCE. Mapping pathogenic mutations suggests an innovative structural model for the pendrin (SLC26A4) transmembrane domain. Biochimie. 2017;132:109–20.

2) Giorgio V, Burchell V, Schiavone M, Bassot C., Minervini , Petronilli V, Argenton F, Forte M, Tosatto S, Lippe G., Bernardi P. Ca^{2+} binding to F-ATP synthase β subunit triggers the mitochondrial permeability transition. EMBO Reports. *Submitted*

Summary of the research

Lipid membranes are a fundamental component of living cells, mediating the physical separation of intracellular components from the external environment, as well as the different cellular organelles from cytoplasm. Transmembrane transport proteins confer permeability to lipid membranes, which is essential for nutrient translocation and energy metabolism (1). Crystallography of transmembrane proteins is a particularly challenging problem. Due to their natural localization and chemical properties only a limited number of structures are to date available at atomic resolution (2). *In silico* analysis can be successfully applied to address the structure and to propose testable models of transporters and pores and of their function. My PhD work focused on two main models: Pendrin (SLC26A4) and the Permeability Transition Pore (PTP). These two systems allowed me to investigate different membrane types and permeation mechanisms, i.e. the plasma membrane-specific anion exchange (SLC26A4) and the inner mitochondrial membrane (IMM) unselective PTP.

Pendrin mutations are estimated to be the second most common genetic cause of human deafness, but a precise 3D structure of the protein is still missing. Aim of my work was to obviate the absence of structural information for pendrin transmembrane domain and to give a functional explanation for mutations collected in the MORL Deafness Variation Database. The human pendrin 3D model was inferred by homology with SLC26Dg (3) and then validated analyzing the surface distribution of hydrophobic residues. The resulting high quality model was used to map 147 pathogenic human mutations. Three mutation clusters were found, while their localization suggested an innovative 14 transmembrane domain structure for pendrin.

The nature of PTP has long remained a mystery. In 2013 Giorgio *et. al.* (4) suggested dimers of F_1F_O (F)-ATP synthase to form the pore, however the exact PTP composition and how can a pore form from the energy-conserving enzyme is still matter of debate. PTP opening is triggered by an increased Ca^{2+} concentration in the mitochondrial matrix, and is favored by oxidative stress. To shed light on PTP function, I investigated the effect of Ca^{2+} binding to the Me^{2+} binding site of the F_1 domain of F-ATP synthase

through molecular dynamics (MD) simulations. A similar approach was also applied to the F-ATP synthase β subunit mutation T163S, which alters the relative affinity for Mg^{2+} and Ca^{2+} (5). Experimental data show that Ca^{2+} binding stiffens the complex structure and that the T163S mutation induces resistance to PTP opening. Further, catalytic site rearrangement induced from different ion occupancy, as well as the mutation T163S, yields relevant variation of the interaction between F_1 domain and OSCP subunit. I suggest that an unstructured loop between residues 82-131 of the β subunit transmits the structural rearrangement originated into catalytic site to the OSCP subunit and then to the inner membrane through the rigid lateral stalk.

The critical role emerging for OSCP in the PTP regulation opens two parallel questions, i.e. (i) how the OSCP-mediated opening signal is transmitted to the trans-membrane region and (ii) what are the transmembrane PTP components. Variation in pore conductivity among species suggested that the putative pore-forming subunits may be different in different species. Sequence alignment was performed for all the subunits of F-ATP synthase, but we mainly focused on subunits e, g and b due to their localization in the complex and sequence conservation. Specific mutations affecting F-ATP synthase were collected and their functional effect is currently under analysis. In parallel, the presence and features of e, g and f subunits across eukaryotes was investigated by mean of phylogenetic analysis. Protein homologues of these specific subunits were found to be widespread in eukaryotes from yeast to plants while we found that *Oomycetes* lack subunits e and g and green algae subunit e. This observation suggest an ancient evolution for the F-ATP synthase dimerization subunits and possibly for the PTP. Further analysis and experimental validation are planned to clarify this aspect.

Riassunto della ricerca

Le membrane lipidiche sono una componente fondamentale delle cellule viventi, separano fisicamente le componenti intracellulari dall'ambiente esterno e i diversi organelli del citoplasma.

Le proteine di trasporto conferiscono permeabilità alle membrane lipidiche, proprietà essenziale per la traslocazione di nutrienti e la conservazione dell'energia (1).

La cristallografia di proteine transmembrana è problematica a causa della loro localizzazione e proprietà chimiche, e solo un numero piuttosto ridotto di strutture è disponibile (2). L'analisi i*n silico* può essere applicata con successo per investigare le strutture e il funzionamento proporre modelli testabili di trasportatori e delle loro funzioni. Il lavoro del mio dottorato sì è focalizzato su due modelli: la pendrina (SLC26A4) e il poro di transizione di permeabilità (PTP). Questi due sistemi proteici mi hanno permesso di studiare due differenti tipi di membrana e meccanismi di permeabilità: la membrana plasmatica con scambio specifico di anioni (SLC26A4) e la membrana interna mitocondriale con la permeabilità non selettiva mitocondriale (PTP).

Le mutazioni della pendrina sono stimate essere la seconda causa genetica più comune della sordità umana, ma la struttura della proteina non è stata ancora determinata. Scopo del mio lavoro è stato quello di sopperire all'assenza di informazioni strutturali per il dominio transmembrana della pendrina e di dare una spiegazione funzionale per le mutazioni raccolte nel MORL Deafness Variation Database.

Il modello 3D della pendrina è basato sull'omologia con SLC26Dg (3) ed è stato validato analizzando la distribuzione sulla superfice dei residui idrofobici. L'alta qualità risultante dal modello è stata usata per mappare 147 mutazioni patologiche umane. Tre cluster di mutazioni sono stati trovati e la loro localizzazione suggerisce per pendrina un innovativa struttura a 14 domini transmembrana.

Anche la natura del PTP è rimasta a lungo misteriosa. Nel 2013 Giorgio *et al.* (4) hanno suggerito che i dimeri di F_1F_O (F)-ATP sintasi formino il poro, tuttavia l'esatta composizione e il modo in cui il poro di transizione si possa formare è ancora materia di dibattito. L'apertura del PTP è innescata da un aumento della concentrazione di Ca^{2+}

nella matrice mitocondriale ed è favorita dallo stress ossidativo. Per fare luce sul funzionamento del PTP ho studiato l'effetto del legame del Ca^{2+} al sito per i cationi divalenti (Me^{2+}) nel dominio F_1 attraverso la dinamica molecolare (MD). Un approccio simile è stato anche applicato alla mutazione T163S, che fa variare l'affinità relativa per Mg^{2+} e Ca^{2+} (5). I dati sperimentali mostrano come la mutazione induca resistenza all'apertura del PTP. La MD ha dimostrato come il legame del Ca^{2+} irrigidisca la struttura del complesso. Il riarrangiamento del sito catalitico indotto dai differenti ioni che lo occupano, così come la mutazione T163S, causa rilevanti variazioni delle interazioni tra il dominio F_1 e la subunità OSCP. Suggerisco che un loop non strutturato tra i residui 82-131 della subunità β trasmetta il riarrangiamento strutturale originato nel sito catalitico a OSCP e quindi alla membrana interna attraverso il rigido stalk laterale.

Il ruolo critico che emerge per OSCP nella regolazione del PTP apre due domande collegate: (i) come il segnale di apertura mediato da OSCP venga trasmesso alla regione trans-membrana e (ii) quali siano i componenti transmembrana del PTP.

Le variazioni di conduttanza del poro osservate in specie diverse suggeriscono che le subunità che formano il canale debbano avere delle differenze significative. E' stato prodotto un allineamento di sequenze per tutte le subunità della F-ATP sintasi. I risultati preliminari ci hanno spinto a focalizzarci sulle subunità e, g e b a causa della loro localizzazione e conservazione di sequenza. Basandomi sugli allineamenti multipli ho suggerito mutazioni puntiformi per testare l'importanza di specifici residui ai fini dell'apertura del poro. In parallelo la presenza delle subunità e e g tra gli eucarioti è stata indagata attraverso un analisi filogenetica. Proteine omologhe di queste specifiche subunità sono presenti in tutti gli eucarioti: dai lieviti alle piante, tuttavia gli Oomiceti sono risultati mancanti delle subunità e e g e le alghe verdi della subunità e.

Questi risultati suggeriscono un'origine antica per le subunità di dimerizzazione della F-ATP sintasi e probabilmente anche del PTP. Per chiarire questo aspetto saranno necessarie ulteriori analisi e verifiche sperimentali .

1.INTRODUCTION

1.1 Cell membranes and membrane proteins

Phospholipid membranes are a fundamental component of both Prokaryotic and Eukaryotic cells. Their functions are crucial, dividing the cell from the external environment, maintaining the differences in solutes concentrations and electrostatic potentials and permitting the compartmentation of the cell (6). The chemical exchange of the cell with the environment or between cytoplasm and organelles is essential for life. Evolution solved the permeability problem by incorporating complex transmembrane protein machineries, providing in turn specific transport capabilities (1). The importance of this function is apparent, given that approximately 25% of all proteins are membrane proteins (7) and that solute carriers (SLCs) are the second largest family of membrane proteins with at least 384 proteins in humans (8).

Here I will present two systems involved in cell homeostasis: (i) Pendrin (SLC26A4), an anion exchanger located on the plasma membrane, (ii) and the PTP of the IMM.

1.2 Pendrin (SLC26A4)

Pendrin is an anion exchanger of the apical cell membrane and a member of the SLC26A family (SLC26A4) (9,10). It mediates the transport of Cl^-, HCO_3^-, OH^-, I^- ions, as well as of formate, nitrate and thiocyanate. The SLC26A4 gene is mostly expressed in the inner ear, thyroid and kidney, while different tissue-specific specializations were reported in the literature (11–14).

1.2.1 Pendrin pathophysiology

Reduction in pendrin function causes endolymph acidification and is thought to be responsible for Ca^{2+} re-absorption inhibition, yielding auditive sensory transduction defects (12). In the inner ear, pendrin was found in endolymphatic sac and hair cells

(11), where it is involved in pH homeostasis, acting as a HCO_3^-/Cl^- exchanger (12). In the thyroid, pendrin is expressed in follicular cells (15), where it operates as an electroneutral I^-/Cl^- exchanger allowing I^- efflux from the cell to the follicular lumen (13,16). The presence of a low concentration of Cl^- in the thyroid follicular lumen is necessary to support I^- efflux by the pendrin exchanger (16). However the $K_{0.5}$ of I^- is lower that of Cl^- favoring the $[Cl^-]_o/[I^-]_i$ over $[Cl^-]_o/[Cl^-]_i$ exchange (16) .

In kidney, pendrin was found in both type B and non-A-non-B cells of cortical collecting ducts (17), either as Cl^-/OH^- or Cl^-/ HCO_3^- exchanger (14).

Mutations of the SLC26A4 gene cause Pendred Syndrome (PS), as well as non-syndromic hearing loss with enlarged vestibular aqueduct (ns-EVA) (18). Biallelic SLC26A4 mutations are thought to affect I^- efflux, promoting a localized defect of I^- organification, which is believed to be one the causes of typical Pendred syndrome, characterized by congenital fluctuating and progressive hearing loss associated with vertigo and/or goiter (19).

A number of monoallelic mutations have been associated with ns-EVA (20). However, previous experiments aimed at shedding light on ns-EVA pathogenesis suggested that a minimal retained transport ability is sufficient to prevent thyroid dysfunction but not sensorineural deafness (21). ns-EVA patients with no or biallelic mutations in SLC26A4 have been reported (18,22–24). On the other hand, cases of Pendred syndrome and ns-EVA associated to a more complex genetic scenario are described in the literature, i.e. double heterozygosity between SLC26A4 and other genes, such as FOXI1 (25) and KCNJ10 (26).

1.2.2 Pendrin domain organization

As already mentioned experimental information on protein structure is still missing,. Some mutations have been analyzed for their effects on anion transport (Table 1), however the precise molecular mechanisms underlying pendrin function remain largely unknown. Like the SulP transporters, pendrin comprises a transmembrane domain and an intracellular Sulfate Transporter–AntiSigma factor agonist (STAS) domain, regulating anion trafficking, stability and transport (16). The transmembrane domain of 423 amino acids presents a conserved “SulP sulfate transport signature” at

the N-terminus of the transmembrane (TM) region (27), and a “Saier motif”, conserved among all SLC26A family members, located at the C-terminus of the TM domain (9,28). Finally, two glycosylation sites at Asparagines N167 and N172, probably located on an extracellular loop of the TM domain, have been experimentally determined (29).

In 1997 Everett et al. proposed a topology model of the transmembrane region characterized by 11 transmembrane (TM) segments (30), while Royaux et al. demonstrated the cytosolic localization of the N- and C- termini suggesting 12 TM segments (31,32). Recently, Gorbunov *et al.* proposed an innovative 14 TM model for prestin (SLC26A5), a member of the SLC26/SulP family and paralog of pendrin (33). This model was constructed using a high-resolution structure of the bacterial uracil transporter UraA (34). The authors predicted the two conserved SulP and Saier motifs to be in direct contact, overlapping two functionally relevant regions distant in sequence, termed Non Linear Charge domains NLC1 and NLC2, respectively. Very recently, the structure of SLC26Dg, a prokaryotic member of the SLC26 family, was solved. SLC26Dg adopts the same fold observed for UraA, with a slightly higher sequence identity with pendrin (SLC26Dg 19%, UraA 14%, respectively (3)).

1.3 Mitochondrial Permeability Transition Pore

The Permeability Transition Pore (PTP) is an unselective channel located in IMM (35). The PTP may regulate mitochondrial Ca^{2+} homeostasis, through transient openings (36), while long-lasting PTP openings cause depolarization, ATP depletion, osmotic swelling of the matrix leading to rupture of the outer mitochondrial membrane (OMM) with release of pro-apoptotic factors thus contributing to cell death (37).

1.3.1 Mitochondria

Mitochondria evolved from a bacterial progenitor via symbiosis within an eukaryotic host cell. The development of genomics, strongly supported the monophyletic origin of mitochondria from α-Proteobacteria with Rickettsiales often identified as the closest phylogenetic order related to mitochondria (38).

Besides their central role in ATP synthesis and oxidative metabolism, mitochondria contribute to intracellular Ca^{2+} homeostasis and generation of reactive oxygen species (ROS) and are determinant for cell death. Mitochondrial processes are highly compartmentalized due to the existence of two membranes and to the quite selective localization of proteins, nucleotides and coenzymes in the intermembrane and matrix spaces (37).

The OMM is characterized by a high content of phosphatidylcholine, phosphatidylinositol and triglyceride (39). OMM prevents the release of cytochrome c and other mitochondrial proteins involved in apoptosis (40).

The IMM is rich of cardiolipin (39), its permeability is strictly controlled by highly specific transporters and by tightly regulated channels. IMM indeed is the site where the coupled processes of respiration and ATP synthesis (oxidative phosphorylation) occur. Oxidative phosphorylation is a sequence of energy conversion processes through which the exergonic flow of electrons along the respiratory complexes produces the endergonic pumping of protons from the mitochondrial matrix to the intermembrane space. The subsequent proton gradient, formed by two components namely $\Delta\psi_m$ and ΔpH, generates a proton motive force (Δp) that is used by F-ATP synthase to synthetize ATP. Furthermore, the proton gradient is also utilized for the uptake of phosphate, the exchange of ADP/ATP and for the maintenance of ion homeostasis.

The IMM is characterized by the presence of invaginations named cristae. Electron cryomicroscopy of mitochondria (41) revealed that F-ATP synthase, organized in dimers, is essential to maintain a high local curvature of the IMM (42) and normal cristae morphology (43) and that dimers associate to form long rows of oligomers at the cristae edges of mitochondria. It was suggested that in areas of sharp membrane curvature the charge density is higher and hence a higher proton concentration could drive F-ATP synthase (44).

1.3.2 Ca^{2+} homeostasis in mitochondria

The proton motive force across the IMM is utilized to maintain mitochondrial Ca^{2+} homeostasis. The mitochondrial Ca^{2+} uniporter (MCU) mediates Ca^{2+} uptake down its

electrochemical gradient (45). Release of Ca^{2+} from the matrix to the intermembrane space is mediated by the mitochondrial Na^{+}/Ca^{2+} exchanger, which is functionally coupled with the Na^{+}/H^{+} exchanger. This coupling makes matrix Ca^{2+} release dependent on H^{+} reuptake (46). An increase in the intramitochondrial Ca^{2+} concentration activates enzymes involved in oxidative metabolism as pyruvic, isocitric and oxoglutaric dehydrogenases as well as F-ATP synthase (47). This increase could reflect the ability of mitochondria to buffer undesired elevation in cytosolic Ca^{2+} concentration. However, a recent quantitative analysis has indicated that mitochondria do not appear to represent a significant dynamic buffer of cytosolic Ca^{2+} under physiological conditions while they might shape cellular Ca^{2+} concentration dynamics upon prolonged elevations of cytosolic Ca^{2+} concentration (48).

The uptake of Ca^{2+} may lead to opening of the PTP, an unselective channel of high conductance (40). Transient opening of PTP permits depolarization (49) with release of mitochondrial Ca^{2+} (36) even for small Ca^{2+} gradients. Consistently, treatment of cardiomyocytes with cyclosporin A (CsA), which desensitizes the PTP by inhibiting the binding of cyclophilin (CyP) D, a PTP enhancer, causes the increase of Ca^{2+} in mitochondria (48), and the same result was obtained with the genetic deletion of CyP D (50). On the other hand, long-lasting PTP opening causes matrix swelling, rupture of the OMM and release of proapoptotic factors causing cell damage which can result in cell death (37).

1.3.3 Mitochondrial permeability transition pore

The PTP is an unselective channel located in the IMM with a radius of 1.4 nm in mammals (35) and a conductance between 0.9 and 1.5 nS (51,52). The existence of the mitochondrial permeability was discovered very early, and in the 1970s Haworth and Hunter coined the term “permeability transition” and suggested that the permeability increase was due to the opening of a protein channel in the IMM (53–56). For a long time the structural composition of PTP remained a mystery. A variety of proteins have been claimed to be responsible for pore formation: the Pi carrier and the adenine nucleotide translocator (ANT) in the IMM and TSPO (translocator protein of 18 kDa) and VDAC (voltage-dependent anion channel) in the OMM (57). Only in 2013

Giorgio *et. al.* identified the F-ATP synthase dimer as the channel-forming component of the PTP. This finding was based on two sets of results: (i) the interaction of CyPD with F-ATP synthase and the recognition of OSCP as the binding partner of CyPD. CyPD is a matrix protein that has peptidyl-prolyl *cis-trans* isomerase activity that assists in protein folding (58). Its binding with F-ATP synthase was favored by Pi and was counteracted by CsA. CyPD sensitizes the PTP to Ca^{2+} and reduces by 30% ATPase activity. Treatment with CsA, which induces the detachment of CyPD, reestablishes the F-ATP synthase activity (59). The binding of CyPD occurs on the lateral stalk on OSCP subunit (25), and OSCP is also the binding site of Bz-423, which also partially inhibits F-ATP synthase and induces PTP opening (4,60).

Gel-purified dimers of F-ATP synthase form channels triggered by Ca^{2+}, Bz-423 and oxidative stress, and inhibited by Mg^{2+}/ADP in *Bos taurus* (4), *Saccharomyces cerevisiae* (61) and *Drosophila melanogaster* (62), demonstrating their role in PTP formation.

The mechanism of PTP formation is still the subject of active investigation. Bernardi *et al.* proposed that the channel forms starting from dimers of F-ATP synthase after a conformational change that would follow replacement of Mg^{2+} with Ca^{2+} at the catalytic site, which is consistent with the literature on the F-ATP synthase. Indeed, when Ca^{2+} replaces Mg^{2+} ATP hydrolysis is not coupled to the formation of a H^+ gradient (63,64) suggesting that a conformational change leads to the apparent uncoupling of chemical catalysis from H^+ transport. Bernardi and coworkers suggest that the conformational change leads to PTP opening, and the lack of measurable H^+ translocation is due to H^+ backflow through the pore (37).

In this scenario the binding of CyPD to OSCP would cause a conformational change affecting the accessibility of Me^{2+} to the catalytic binding sites, favoring the possible occurrence of Ca^{2+} binding when its matrix concentration increases. The conformational change would also be favored by ROS-dependent thiol oxidation and counteracted by thiol reduction.

As described in the previous paragraph opening of the PTP is reversible, and probably follows the replacement of Ca^{2+} by Mg^{2+} in the catalytic binding site (2).

1.3.4 Regulation of the PTP

PTP formation and regulation appear to be well conserved among species. PTP so far was detected in mitochondria from *Bos taurus*, *Saccharomyces cerevisiae* and *Drosophila melanogaster* as well as fish and plants (4,61,62). In all these organisms PTP Ca^{2+}-dependent channel formation took place under condition of oxidative stress (thiol oxidation or cross-linking) and was inhibited by Mg^{2+}, adenine nucleotides and acidic pH.

However differences exist between species, in terms of channel unit conductance, sensitivity to Pi, presence of a mitochondrial CyPD and inhibition by CsA.

In bilayer experiments with dimers of the F-ATP synthase, channel conductance varies between 53 pS in *Drosophila melanogaster* to 300 pS in yeast and 500 pS in mammals (4,61,62) suggesting structural differences in the channel. Only mammals and *Saccharomyces cerevisiae* possess mitochondrial matrix CyPs but the PTP is inhibited by CsA only in mammals. However, *Drosophila melanogaster* does not possess a mitochondrial CyP, yet expression of human CyPD in Drosophila $S2R^{+}$ cells sensitizes the PTP to Ca^{2+} in a process that is insensitive to CsA (62).

Pi favors the opening of PTP increasing the binding of CyPD to OSCP on F-ATP synthase. In keeping with the effect of CyPD, Pi enhances PTP opening (65) only in mammals while in yeast and *Drosophila melanogaster* it acts as a PTP inhibitor. These sets of data suggest that CyPD is able to regulate PTP only in mammals.

As mentioned before an essential permissive factor to trigger PTP opening is the presence of matrix Ca^{2+}, which binds a Me^{2+} binding site where also other ions (Mg^{2+}, Sr^{2+} and Mn^{2+}) can bind resulting in PTP inhibition (37).

PTP is strongly affected by matrix pH and mitochondrial depolarization. The pH optimum for PTP opening is 7.4, while the open probability decreases below pH 7.4 through protonation of histidine residues that can be prevented by diethylpyrocarbonate (66,67). This effect is present also in CyPD null mitochondria, indicating that the histidine isn't located on CyPD (68). Finally IMM depolarization increases the probability of pore opening (67,69,70) in a process where arginine residues may play a critical role (71–73).

1.3.5 Structure of F-ATP synthase

F-ATP synthase is a multiprotein complex found in bacterial energy-transducing membranes, mitochondria and chloroplasts (74). It consists of two functional domains: the membrane extrinsic F_1 and the membrane intrinsic F_O connected by central and peripheral stalks. Seventeen distinct subunits form the eukaryotic complex (Fig. 1). F_1 domain is composed by five type of globular proteins α, β, γ, δ and ϵ. Three α and β subunits are present in each domain giving a total mass of approximately 350 kDa (75). Walker compared the F_1 domain of F-ATP synthase to "an orange made of six segments (αβ) arranged around the central pith stalk of the fruit (γ, δ and ϵ)" (74) .

The F_1 domain contains a total of six Me^{2+}-adenosine phosphate binding sites, three catalytic and three non-catalytic. ATP catalysis requires the binding of the adenosine phosphate in complex with Mg^{2+} (76) that is fundamental in the β subunits substrate recognition. Mg^{2+} is hexa-coordinated by βThr_{163} (in the bovine enzyme), and by 3 ordered water molecules coordinated by βArg_{189}, βGlu_{192} and βAsp_{256} (77). Mg^{2+} can be replaced by other divalent cations like Co^{2+}, Zn^{2+}, Fe^{2+}, Mn^{2+}, Cd^{2+}, Ni^{2+}, Ca^{2+} but the catalytic activity is inversely proportional to the ionic radius of the metal (78). Ca^{2+} ions support γ subunit rotation and ATP hydrolysis, but not H^+ translocation and ATP synthesis, as found both in bacteria (63) and mammals (64), suggesting that the catalytic site is subject to a rearrangement when occupied by Ca^{2+}.

ATP catalysis is mediated by the rotation of the F_O domain generated by the proton motive force. Rotation of subunit γ takes each of the 3 catalytic sites through at least 3 major functional states denoted as β_E, β_{DP} and β_{TP}, thereby supporting the synthesis of 3 ATP molecules for each 360° rotation (79–81).

The rotation of subunit γ depends on rotation of the c-ring. The latter is formed by a variable number of c subunits (8 in bovine mitochondria (82) 10 in *Saccharomyces cerevisiae* (83), 11 in *Ilyobacter tartaricus* (84), 13 in *Caldalkalibacillus thermarum* (85), 14 in spinach chloroplast (86) and 15 in *Spirulina platensis* (87)). Each subunit has two transmembrane segments connected by a loop exposed in the matrix connecting the c-ring with the central stalk. The N-terminal α-helix forms the core of the c-ring while aspartate or glutamate residues located around the midpoint of the C-terminal helix mediate the passage of H^+(88). The proton motive force generates a clockwise rotation

with an estimated rotary speed of approximately 100–150 rev/s depending on the species (74). However, under anaerobic conditions, the energy that drives the rotation is provided by the hydrolysis of ATP, which drives the rotor in a counter clockwise direction and pumps protons across the energy transducing membrane in the outward direction (74). The c ring is in contact with the a subunit and rotates against its hydrophobic surface. Recently Allegretti *et all*. using electron microscopy resolved the structure finding a fold never observed before composed by horizontal membrane-intrinsic α-helices, arranged in two hairpins at an angle of approximately 70° relative to the c-ring helices (89). An arginine (R210 in *Escherichia coli* protein), strictly conserved in homologs of a subunit, participates in the transport of protons through the F_O domain (90) allowing protons to access the external surface of the c-ring in the rotor, where two polar residues (an aspartate and a glutamine residue) have been proposed to mediate the process (91–93).

The F_1 domain is strongly connected with the transmembrane region through the peripheral stalk. In eukaryotes the peripheral stalk is formed by OSCP, d, F6 and b subunits (94). OSCP is located on top of the F_1 domain and is connected at the C-terminus with the b subunit and F6 (95). b subunit has a long coiled coil region and at the level of the membrane continues with two transmembrane domains, the first of which is involved in the dimerization of the F-ATP synthase complex (42).

Hahn *et al.* recently obtained by cryo-EM a 7Å structure of the IMM region (96). Subunits e and g occupy a density on the dimer interface next to the N-terminal trans-membrane helices of subunit b, with a narrow extension that protrudes 40Å into the inner mitochondrial space.

Subunit e and g are predicted to have a single transmembrane helix with a conserved GxxxG motif, known to facilitate oligomerization of transmembrane proteins (97), and indeed e and g subunits may tightly interact through this motif (98). Furthermore, subunit e holds a hydrophilic coiled coil region at the C terminus that would account for the IMS extension and appears to be involved in F-ATP synthase oligomerization (99). The g subunit interacts with the N terminus of b subunit in the matrix (100). In cryomicroscopy subunit f appears as a curved density at the base of the peripheral

stalk, and the charged C-terminal domain seems to form the most prominent dimer contact (96).

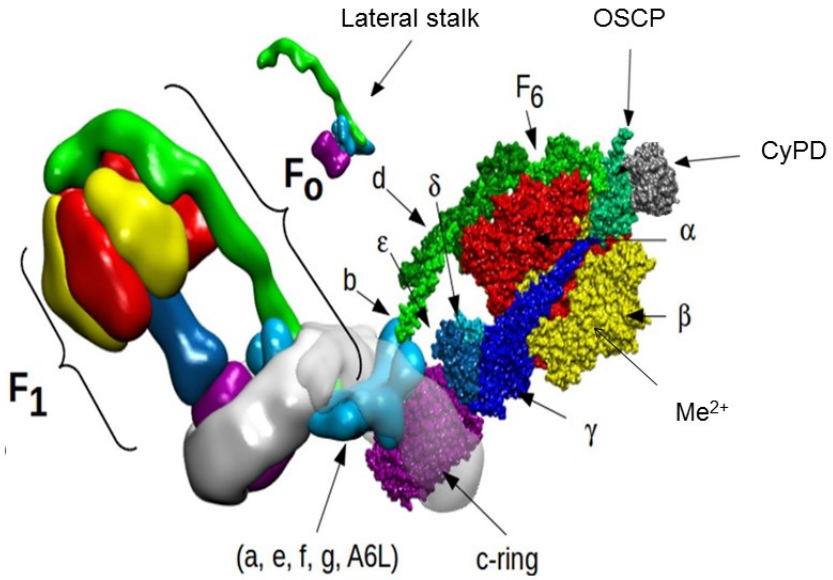

Figure 1 Model of the structure of F-ATP synthase dimer, modified from Bernardi et. al. (40). The F_1 and F_O domains and the lateral stalk are highlighted on the left monomer,while in the left monomer the single subunis are shown. The F_1 α and β subunits are colored in red and yellow, respectively. The F_1 γ, δ, and ε subunits are colored in shades of blue, the peripheral stalk subunits b, d, F6 and OSCP in shades of green, and the c-ring in purple. The remaining F_O subunits a, e, f, g, and A6L are colored in light blue. The intramembrane F_O is surrounded by detergent, shown in white. The PTP regulatory protein cyclophilinD is shown in grey on bound to OSCP. The localization of Me^{2+} in the β subunit is indicated.

1.3.6 F-ATP synthase and PTP formation

The mechanism for PTP channel formation is still an open question. Two sites were proposed as pore forming in F-ATP synthase: the c-ring (101) and the F-ATP synthase dimers at the interface between monomers (4). This second hypothesis was used as the basis for the present work.

c-ring

Jonas and coworkers 2014 (102) reconstituted the c subunit in liposomes observing the formation of a Ca^{2+}-activated channel with properties similar to those described in our labotarory for F-ATP synthase dimers. It was proposed that the channel of the PTP

forms within the c-ring itself after Ca^{2+}-dependent release of F_1 domain. The "F_O channel" could not be closed by subunits γ, δ, or ε, while it was blocked by subunit β.

However, it should be considered that displacement of F_1 from F_O requires very drastic conditions, like treatment with 2 M urea. Furthermore such a dramatic change in the F-ATP synthase complex is hardly compatible with the PTP flickering between open and closed states, characteristic of the Ca^{2+} release.

Another weak point of the c-ring hypothesis is the finding that the *Drosophila melanogaster* F-ATP synthase forms channels with a unit conductance of 53 pS (62), while the mammalian one has a conductance of 500 pS. Since the c-ring of both *Drosophila melanogaster* and mammals belongs to the c_8 set it is quite difficult to see how c-rings of the same size can form 500-pS channels in mammals and 53-pS channels in drosophila.

F-ATP synthase dimer

The Bernardi laboratory observed channel formation after incorporation of gel-purified F-ATP synthase dimers of mitochondria from *Bos taurus* hearts, *Saccharomyces cerevisiae*, and *Drosophila melanogaster* in asolectin bilayers, while channel formation was not observed when monomers were used (4,62,103). The dimer hypothesis is also strongly supported by the effects of genetic ablation of the e and/or g subunits on the yeast PTP (61). The dimerization subunits e and g are not involved in the ATP catalysis process, in keeping with the fact that the catalytic activity of F-ATP synthase can be inhibited (e.g., with oligomycin) without affecting PTP formation. At the same time PTP opening can be inhibited (e.g. by CsA) without affecting the activity of F-ATP synthase (40).

1.4 Are pendrin and F-ATP synthase dimers moonlighting proteins?

Moonlighting proteins are multifunctional proteins able to perform multiple autonomous, often unrelated, functions without partitioning these functions into different protein domains. Indeed both functions are independent meaning that

inactivation of one of the functions (e.g. by mutation) should not affect the second function and vice versa. Moonlighting proteins are usually well conserved and ancient proteins (104). The typical example of moonlighting protein is cytochrome c. Indeed, when located in mitochondrial intermembrane space cytochrome c is part of the electron transport chain, while when released into the cytosolic space after permeabilization or rupture of OMM the protein plays an important role in apoptosis. Indeed, cytosolic cytochrome c forms a complex with the apoptotic protease-activating factor 1 (Apaf-1) starting a signalling cascade that results in apoptotic cell death (105). The respiratory and pro-apoptotic functions are completely independent (106,107).

The proteins studied in my work don't fit perfectly with the definition of moonlighting proteins, but they share several features with this protein class. Pendrin is an anion exchanger and a member of the ancient SLC26 gene family encoding anion exchangers and anion channels (10), however it shows a high variability in the transported substrates depending on the local concentration of the anionic species. Pendrin is a pH regulator in kidney and inner ear, exchanging HCO_3^-/Cl^-, while in the thyroid gland pendrin plays a fundamental role in the efflux of I^-, which is necessary for the synthesis of the thyroid hormone. The transport of I^- apparently could be separated by the HCO_3^- transport. Indeed in ns-EVA only the HCO_3^- transport is compleatly lost while a residual I^- efflux persists. However future studies are needed to clarify the rationale of the different functions.

F-ATP synthase is one of the oldest protein complexes known (108). The proton transport and ATP catalysis are conserved in eukaryotes and prokaryotes while PTP is a feature present only in eukaryotes, suggesting that PTP formation was acquired at a later time. Indeed catalytic activity of F-ATP synthase can be inhibited (e.g., with oligomycin) without affecting PTP formation and *vice versa*. However in contrast with the definition of moonlighting proteins F-ATP synthase is a complex and not a single protein and different subunits are involved in different functions.

1.5 Theoretical introduction to the methods used

1.5.1 Transmembrane domain prediction

The typical transmembrane (TM) segment is a stretch of residues in α-helix folding, crossing a phospholipid membrane. Due to the lipid environment the transmembrane domains are characterized by the predominant presence of hydrophobic amino acids (109). This feature, easily recognizable from the primary structure, encouraged the development of transmembrane domain predictors from the early 1980s (110). An example of the use of this simple approach is the *Kyte-Doolittle* algorythm, based on a simple hydropathy scale of the lateral chains (111). Slightly more complex is the Goldman-Engelman-Steitz algorithm that considers the TM segment as α-helix and also takes into account the presence of polar or charged residues in the TM domains (e.g. pore lining helices or internal salt bridges).

Over the years, with the increased availability of transmembrane protein sequences, other features were recognized as useful to predict the arrangement of transmembrane segments. In particular: clustering of tryptophans and tyrosines at the end of the transmembrane segment, TM specific sequence motifs (eg. GxxxG), different composition of the inside or outside facing connecting loops (109,110).

The inclusion of these rules improves the predictions (112), however a more significant evolution in TM domains predictors was made possible with the use of Hidden Markov Models (HMMs) and other machine learning techniques. With HMMs it is possible to model more precisely the length of the transmembrane α-helices compared with the simplest sequence-based methods, where the length of the membrane helix is defined *a priori* by setting upper and lower limits for the length. Indeed HMMs permit the incorporation of hydrophobicity, charge bias, helix lengths, and grammatical constrains into a single model (113). Another significant increase in the quality of the prediction of transmembrane segments comes from the use of more than one predictor in consensus algorithms (114,115).

1.5.2 Homologue search

A necessary step for different computational analysis (multiple sequence alignment (MSA), homology model, phylogenetic analysis) is the search of homologues protein in databases. Nowadays two algorithms are mostly used for homologous search BLAST, and HMMER.

BLAST

BLAST (basic local alignment search tool), was developed by Altschull in 1990 (116). It is a heuristic algorithm that directly approximates alignments optimizing a measure of local similarity. The BLAST algorithm is composed of three steps:

The query is divided in different “words” of 3 amino acids (or nucleosides). A list of alternative words per each word of the query is built using a substitution matrix. Only the words with a score above an established threshold are considered.

Each word of the alternative words list is searched in the database. When a word matches with the database, the algorithm tries to extend the hit in both directions. If the extensions reach a threshold value “S”, the sequence is named HSP (High Score Segment Pair) and defines a zone of local homology. The “S” value is calculated as a function of the “E” value that describes the number of hits one can "expect" to see by chance when searching a database of a particular size. A high E values and a low S lower the threshold reach increasing the sensitivity but reducing the selectivity. The extension of the homologous segment continues until the local maximum score is reached.

To search homologous sequences in proteins the **Position Specific Iterated** (**PSI-BLAST**) version of the BLAST algorithm was used. Compared with pBLAST, PSI-BLAST is less specific but more sensitive, allowing the identification of proteins with a distant evolutionary relationship. PSI-BLAST uses position-specific scoring matrices (PSSMs) to score the matches between query and database, in contrast to pBLAST which uses pre-defined scoring function. Indeed, PSI-BLAST uses a standard scoring matrix only in the first round while in the next steps PSSMs are generated using MSA of the sequences

found in the previous round, and the process can be iterated until no new sequences are found (116).

HMMER

HMMER is an algorithm analogous to BLAST in the function, but different in the approach used. HMMER indeed converts the query sequence into a HMM profile. The HMM profile residue probabilities are set considering the probability of a standard score matrix such as BLOSUM62 with empirically set insertion/deletion transition probabilities (117). Similarly the iterative method called JackHMMER builds a HMM profile with all the sequences of the first search that reach an E score inclusion threshold. The obtained HMM profile is used for a second search round in the database. With the new HMM profile it is normally possible find more distant homologous that can be iteratively used to build the next profile and perform a new search. The search converges when no new sequences can be found (118).

JackHMMER is able to recover a larger number of sequences with a bigger evolutive distance than PSI-BLAST, with a 28% increase in remote homolog detection (118).

HHpred

HHpred algorithm starts from a query sequence or a MSA, to build an alignment of the target homolog protein by multiple iterations of PSI-BLAST. A HMM profile is generated from the MSA and is then compared with each HMM in the selected database. HHpred possesses a higher sensitivity and alignment accuracy when compared to PSI-BLAST and HMMER (119). The use of more sensitive fold identification techniques are useful to retrieve significant structural relationships when sequence identity between the target and the template is below 25% (120).

1.5.3 Multiple sequence alignment

MSA of protein sequences are important for many applications in computational biology. In this work, the MSA were used to build up phylogenetic trees, identify

important residues in proteins lacking resolved structures, as well as profile-based homolog search.

Several different algorithms to estimate MSA are available (121). Generally they try to maximize the summed aligned score of each sequence pair (122). A popular strategy is the progressive method. This approach can be divided in two steps: (i) a phylogenetic tree is built for the sequences, (ii) the two closer objects are aligned two by two. At first these are single sequences, but progressively groups of still aligned sequences are aligned together.

T-Coffee

T-Coffee is an algorithm based on the progressive method. A global alignment between each pair of sequences is generated using ClustalW, while a local pairwise alignment is performed by Lalign. The local and global pairwise alignments are weighed by sequence identity and the resulting alignments are combined together by addition.

The alignment is extended until the final weight for any pair of residues reflects the information contained in the whole library. This permits the alignment between two sequences to be influenced by the overall alignment. A neighbor-joining tree is built with the pair-wise alignment. Subsequently the tree is used in the final alignment. (123)

MUSCLE

MUSCLE algorithm is composed by three stages:

1) A progressive alignment is performed based on a tree built using UPGMA or neighbor-joining.
2) A second tree is built using a Kimura distance matrix and applying a clustering method to this matrix. The obtained tree is compared with the first one, identifying the set of internal nodes for which the branching order has changed. New alignments are created for the changed tree nodes.
3) The edges are deleted from the tree and the sequences are divided in two disjoint subsets. The MSA for of each subset is extracted and the empty

columns are removed. The next step is the re-alignment of the two subsets one against the other. If the score increase the new alignment is retained while the process is iterated with lowered value.

1.5.4 Protein Homology Modelling

Knowledge of protein structure has a primary importance in modern biochemistry. Improper folding of proteins is associated with many diseases, and this information is critical for the rational design of new drugs. However only a limited number of protein structures is available. The X-ray based structure determination of transmembrane proteins is particularly challenging, due to their peculiar physicochemical properties (124).

In the absence of a resolved protein structure, a possible approach is the homology modeling. In this method a target sequence is aligned with the sequence of a resolved structure called template. To generalize homology modeling can be divided in different steps:

1) **Choice of template and sequence alignment.** The target sequence is used to search the template with the highest similarity. In our case we perform the template search in Protein Data Bank (PDB) (125) througth HHpred (119). The choice of the best template is a critical step for the homology model, because the higher the similarity between target protein and template the higher is the final accuracy of the model. The alignments have then to be evaluated and optimized.
2) **Backbone Generation.** The backbone coordinates of the template are copied in the model.
3) **Loop and side chain modeling.** When the alignment contains gaps the backbone is modified. If the gap is in the target sequence the missing part can be modeled *ab initio,* or can be searched in PDB only for the missing sequence and added to the obtained sequence in the model.

The side chains placement is performed by extraction from a large library of side chian rotamers derived from X-Ray structures. Different rotamers are placed and ranked using energy functions.

4) **Model optimization and validation.** The placing of the side chains easily produces clashes between residues, requiring structure optimization. In this work optimization was achieved by energy minimization using Chimera (126). The quality of the model was investigated with *Qmean* (127), while manual inspection was used to evaluate the expected features of a transmembrane protein, e.g. the final position of transmembrane domains, localization of known pathological mutations, as well as hydrophobicity pattern.

1.5.5 Molecular Dynamics Simulation

The first MD simulation was performed on the bovine pancreatic trypsin (BPTI) in 1977. From the early simulations MD has rapid evoled from the initial 10 ps (30) to the millisecond range (57). MD simulations allow *in silico* investigation of the motions of a protein as function of time. MD can be used to address specific questions about the features of the model and in particular on its protein functions (30).

All simulations in this work were carried out with NAMD (129). The atoms of our protein model follow the Newtonian equation of motion.

$$m_\alpha \ddot{\vec{r}}_\alpha = -\frac{\partial}{\partial \vec{r}_\alpha} U_{\text{total}}(\vec{r}_1, \vec{r}_2, \dots, \vec{r}_N), \qquad \alpha = 1,2 \dots N$$

Where m_α is the mass of atom α, $\vec{r}_\alpha$ is its position, and U_{total} is the total potential energy that depends on all atomic positions and thereby couples the motion of atoms (130).

The potential energy (U_{total}) is calculated through the Force Field CHARMM-27(131). Potential energy consists of the sum of the different force components acting on each atom. Indeed it can be represented as:

$$\mathrm{U_{total}} = \mathrm{U_{\ bond}} + \mathrm{U_{\ angle}} + \mathrm{U_{dihedral}} + U_{vdW} + \mathrm{U_{Columb}}$$

The first three terms represent the energetic component of the covalent bonds. In particular the potential energy generate by the stretching of covalent bond is expressed as:

$$\mathrm{U_{\ bond}} = \sum_{bonds\ i} k_i^{bond}(r_i - r_{0i})^2$$

The component of the angles between two covalent bonds is expressed as:

$$\mathrm{U_{\ angle}} = \sum_{angle\ i} k_i^{angle}(\phi_i - \phi_{0i})^2$$

The torsional bonded interaction :

$$\mathrm{U_{\ dihedral}} = \sum_{dihedral\ i} k_i^{dihe}[1 + \cos(n_i\phi_i - \gamma_i)^2$$

The last two terms describe the interactions resulting from nonbonded atom pairs, i.e. the van der Waal's and the electrostatic contributions. These are respectively derivation of Lennard-Jones potential equation and of Coulomb's law:

$$\mathrm{U_{\ vdW}} = \sum_i \sum_{j>i} 4\varepsilon_{ij}\left[\left(\frac{\sigma_{ij}}{r_{ij}}\right)^{12} - \left(\frac{\sigma_{ij}}{r_{ij}}\right)^{6}\right]$$

$$\mathrm{U_{\ Coulomb}} = \sum_i \sum_{j>i} \frac{q_i\, q_j}{4\pi\varepsilon_0 r_{ij}}$$

The production is carried on in a cell with periodic boundary conditions: the particles are enclosed in the cell that is replicated to infinity by periodic translations. If a particle leaves the cell during the simulation it is copied and replaced at the opposite side. This expedient is used to simulate a large volume of solvent.

Each step of the simulation correspond to 2fs. For each step, the Potential Energy and forces acting on each atom are used to determine the new atom positions. These process is iterated until the end of the molecular dynamics.

1.5.6 Phylogenetic tree

The phylogenetic tree represents the evolutionary relationship of genes or proteins among organisms. Darwin's "Origin of the Species" contains one of the first examples of an evolutive tree, but the use of this analytical tool underwent a dramatic increase with the development of molecular biology. The growth of available DNA and protein sequences dramatically increased the possibility to infer phylogenesis (132). Several methods were developed for phylogenetic tree construction. These can be divided in: **distance methods,** where the aligned sequences are converted into a distance matrix of pairwise differences between the sequences; **character-based methods,** where the characters of each column of the multiple alignment are directly compared between the sequences. Distance methods are Neighbor Joining and UPGMA. Character-based methods include Parsimony, Maximum Likelihood, Bayesian Interference.

Among these methods we chose the Bayesian Inference, which with our samples resulted in more stable trees. Bayesian Inference is based on the Bayes's theorem.

$$\Pr[\text{Tree}|\text{Data}] = \frac{\Pr[\text{Data}|\text{Tree}] \times \Pr[\text{Tree}]}{\Pr[\text{Data}]}$$

The Bayes's theorem combines the prior probability of phylogeny Pr[Tree] (determined from a probability distribution over all possible trees given before the data are examined (133)) with the likelihood Pr[Data|Tree] to produce a posterior probability distribution on trees Pr[Tree|Data]. The posterior probability of a tree is the probability that the tree is correct. The tree with the highest posterior probability might be chosen as the best estimate of phylogeny. Markov chain Monte Carlo (MCMC) method simplifies significantly the calculation of posterior probability. MCMC algorithm involves two steps: (i) A new tree is proposed by stochastically perturbing the current tree. (ii) This tree is then either accepted or rejected. If the new tree is

accepted, then it is subjected to further perturbation. The proportion of the time that any tree is visited is a valid approximation of the posterior probability of that tree (132).

2. Materials and methods

2.1 Transmembrane domains predictions of pendrin

In the work described in this thesis for the transmembrane domains of pendrin I used a consensus approach between nine different predictors: HMMTOP (134), DAS-TM filter (135), Phobius (136), TMHMM (113) OCTOPUS(137), SCAMPI-seq(138), SCAMPI-msa(138), PRODIV(139), PRO(139). The same weight was given to all the predictors. The states of each residue (transmembrane, or not) were determined by a consensus of at least five predictors. The choice of the predictors fulfills the need of a wide range of different methods: HMMTOP, Phobius, TMHMM, SCAMPI, PRO and PRODIV are based on Hidden Markov model, OCTOPUS uses a combination of Hidden Markov model and artificial neural networks, while DAS-TM filter is based on hydrophobicity profile.

2.2 Pendrin homologous search and multiple alignment

Pendrin homolog sequences were retrieved with three iterations of PSI-Blast (140) on the non-redundant database and aligned using T-Coffee (141) (both used with standard parameters). The alignment was manually refined using the Jalview viewer (142).

2.3 Pendrin Homology Modelling

A template search for homology modelling was performed with HHpred (143) from the manually curated alignment using default parameters.

At first the bacterial uracil transporter UraA (144) (which shows 14% identity with pendrin) resulted as the best template for the transmembrane domain, subsequently the resolution of SLC26Dg, a prokaryotic member of the SLC26 family (3) offered a better template for pendrin with 19% identity.

Three different softwares were used for homology modeling: **SwissModel** (145), **Modeller** (146) and **I-Tasser** (147). SwissModel and Modeller use a similar approach of homology modeling in which the loops are retrieved from a database/set of experimental structures. I-Tasser models the loops by *ab-initio* modelling. All the softwares were used starting from the same target template alignment.

2.4 Structure preparation and molecular dynamics

Chains A, B, C, D, E, F, G, S of bovine F-ATP synthase membrane extrinsic region published by Rees *et al.* (95) (PDB code: 2WSS) were used as starting point of simulations. The structure consists of 3 α-subunits (chains A, B, C) and 3 β-subunits (chains D,E,F) crystallized in three catalytic states "Empty" (E), ATP bound (TP) and ADP bound (DP), respectively. The crystal structure also includes subunits γ (chain G) and OSCP (chain S). Although this currently represents the most complete high resolution structure available for F-ATP synthase complex, some protein fragments were not resolved at atomic resolution. Chains presenting unresolved segments were removed and not included in our simulations. The final system consisted of 8 chains contain the following 3,273 resolved residues: α_E, 1–510; α_{TP}, 23–401 and 410–510; α_{DP}, 27–510; β_E, 9–474; β_{TP}, 9–474; β_{DP}, 9–475; γ, 1–61, 70–96, and 101–272; OSCP, 1–146. The phosphoaminophosphonic acid-adenylate ester (ANP) present in the crystal structure was substituted with adenosine triphosphate (ATP). Parameters for ATP were included in the force field as described in *Polticelli et al.* (148).

The β subunit T163S mutation was introduced on all three β subunits binding sites. Mutation placement was performed with Bluues (149). Two metals were tested in the Me^{2+} nucleoside binding sites: Mg^{2+} (originally present in the protein structure) and Ca^{2+}. No specific restrictions were applied to the metal ions binding sites during MD run.

The simulations of all four models were carried out on GPUs with NAMD (129) using the CHARMM-27 force field. The TIP3p water model was used to simulate the explicit solvent in a cubic box of 141.5 x 160.2 x 162.5 Å. Each simulation run consisted of 100

conjugate gradient minimization steps, 100 ps in NVT conditions, and 50 ns of MD. The temperature was kept at 310 K and pressure at 1.01325 bar in all simulations, excluding the NVT pre-simulation steps. A 2 fs integration timestep was used with a Verlet method integrator (129).

2.5 Mrbayes tree building

A search of homologous protein for the b subunit was performed using the human sequence (Uniprot ID P24539) as query in a 5 iterations search of Jackhmmer setted to E score at 0.01 the 14 march 2016. Six hundred thirty-four sequences were obtained from the search. Because of the absence of vegetal organisms the search was repeated for 3 interactions using as query the previously identified *Arabidopsis thaliana* F-ATP synthase b subunit homolog (Uniprot ID G1C2W7), collecting 78 new sequences.

All 712 sequences were manually refined: removing fragmented or biased sequences, deleting redundant sequences (more than 98% identity), selecting the isoform (if more than one) with the lowest E score. After this filtrations 228 sequences were selected.

The sequences where used in Mrbayes to build the phylogenetic tree of b subunits. The alignment obtained with Muscle was converted in a nexus file format and copied in the execution file. The mixed model for amino acids sequences with gamma lset rates. Ten million maximum of generation were setted. A single chain was used with a temperature of 0.2.

3.RESULTS AND DISCUSSION

3.1 PENDRIN (SLC26A4)

3.1.1 Aim of the project

Pendrin is an anion exchanger of the apical cell membrane and a member of the SLC26A family (SLC26A4) (9,10). The SLC26A4 gene is mostly expressed in the inner ear, thyroid and kidney, while different tissue-specific function were reported in the literature (11–14). Precise information of protein structure is still missing, although SLC26A4 mutations are estimated to be the second most common genetic cause of human deafness. In the absence of structural information for pendrin transmembrane domains, aim of my work was to provide a working model for protein topology and a functional explanation for mutations collected in the MORL Deafness Variation Database. The structure of pendrin was modelled by homology and used to map the pathological mutations. Using our model we suggest a putative functional and structural effect for the mutations. A paper originated form this project was published (150).

3.1.2 Background and state of the art: preliminary mutation mapping reveals the presence of three mutations clusters

One hundred and forty-seven pathological missense point mutations, found in patients with Pendred syndrome or ns-Eva were selected in MORL Deafness Variation Database (URL:http://www.deafnessvariationdatabase.org/). All these mutations affecting the transmembrane region of pendrin were preliminarily mapped on the topology obtained by Uniprot (151). The map (Fig. 2) highlights the presence of three mutation clusters marked with the capital letters A, B, C. In the Uniprot based transmembrane

topology, mutations clusters are localized respectively on: 3rd transmembrane domain (TMD), on the external loop between the 9th and the 10th TMD, on the internal loop between the 10th and the 11th TMD.

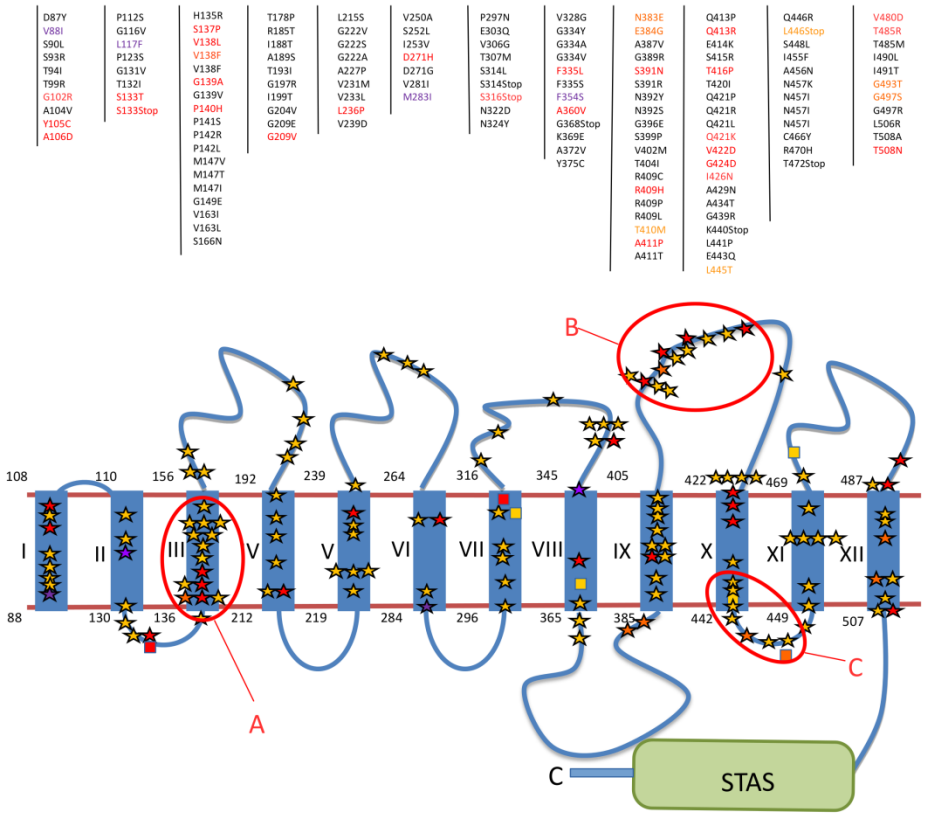

Figure 2 Uniprot 12 TMDs model of pendrin. The TM helices are indicated as rectangles. The pathological mutations are listed above the corresponding TM domain. In TM domains the point mutations are indicated with stars while the stop codon mutations are indicated with squares. The colors change with the caused pathology: red for the mutations found in Pendred syndrome, yellow for the mutations found in ns-EVA, orange for the mutations found in both pathologies. Purple denotes mutations with a mild phenotype. The mutation clusters are indicated with the letters A,B,C .

3.1.3 Trasmembrane prediction

The human pendrin sequence was retrieved from Uniprot (152) (accession code: O43511-1) and used as query in nine different transmembrane domain predictors. The results of the predictors were used for the construction of a consensus (Fig. 3). The results show substantial differences between the different predictors. The number of predicted TMDs vary between the 9 predicted by TMHMM and the 14 predicted by

HMMTOP with a relative majority of a 12 TMD predictor. The consensus between the major predictors confirms 12 TM domains.

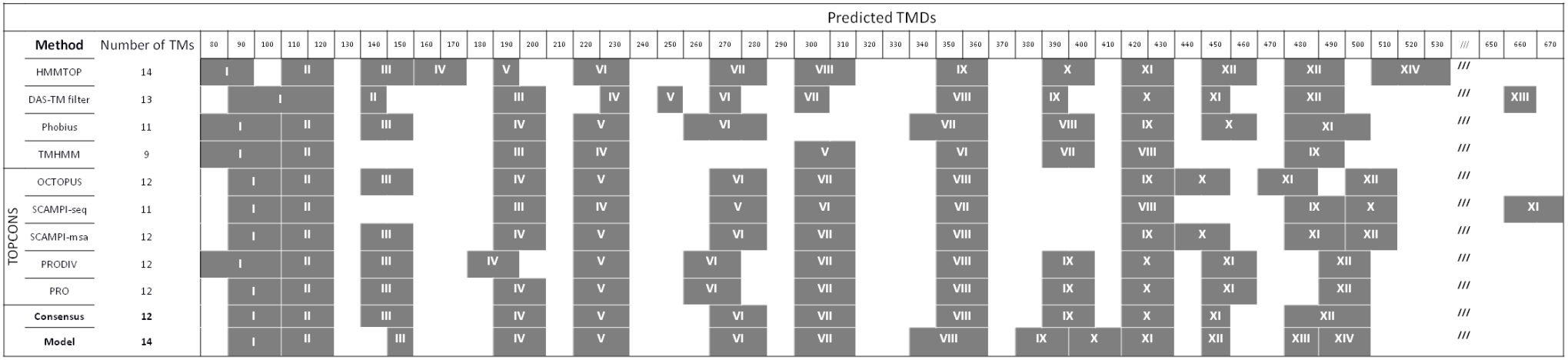

Figure 3: Results obtained from TM predictors for pendrin. The number of the first and the last residues of the TM segment are shown according to different methods. Consensus is established between at least 5 predictors and compared to the homology model.

3.1.4 Homology modelling

A prokaryotic member of the SLC26 family SLC26Dg (PDB code: 5DA0) (3) was used as template for pendrin. The alignment is shown in Fig. 4. It appears that pendrin contains two sequence insertions not present in SLC26Dg, corresponding to two loops between TM3-TM4 and TM5-TM6.

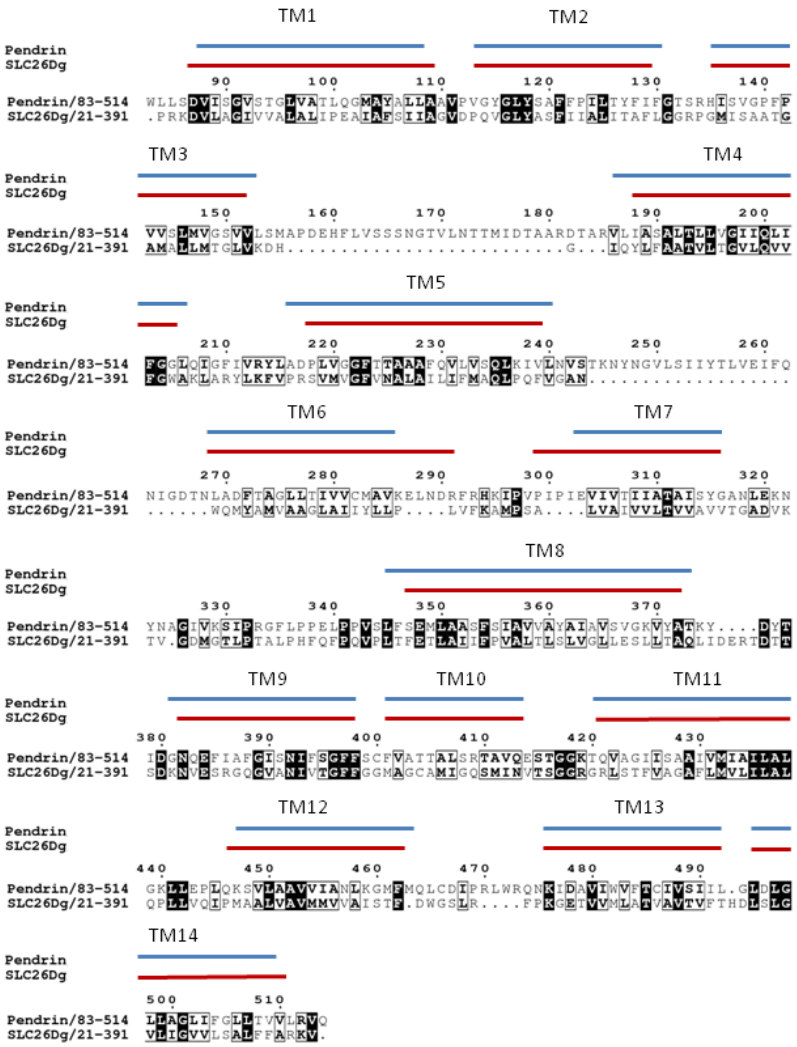

Figure 4. Alignment between SLC26Dg and Pendrin performed by ESPript, modified adding in blu TM domains of Pendrin model and in red TM domains for SLC26Dg template. For SLC26Dg the TM domains where assigned based on PDB structure (ID 5DA0), while for pendrin by our model inspection.

The alignment was used in three different homology modelling softwares: SwissModel. I-Tasser, and Modeller. Fig. 5 shows the three structures superimposed.

As expected the number and the position of the TMDs are conserved in all the models, while only the conformations of loops 154-186 and 241-269 show significant differences.

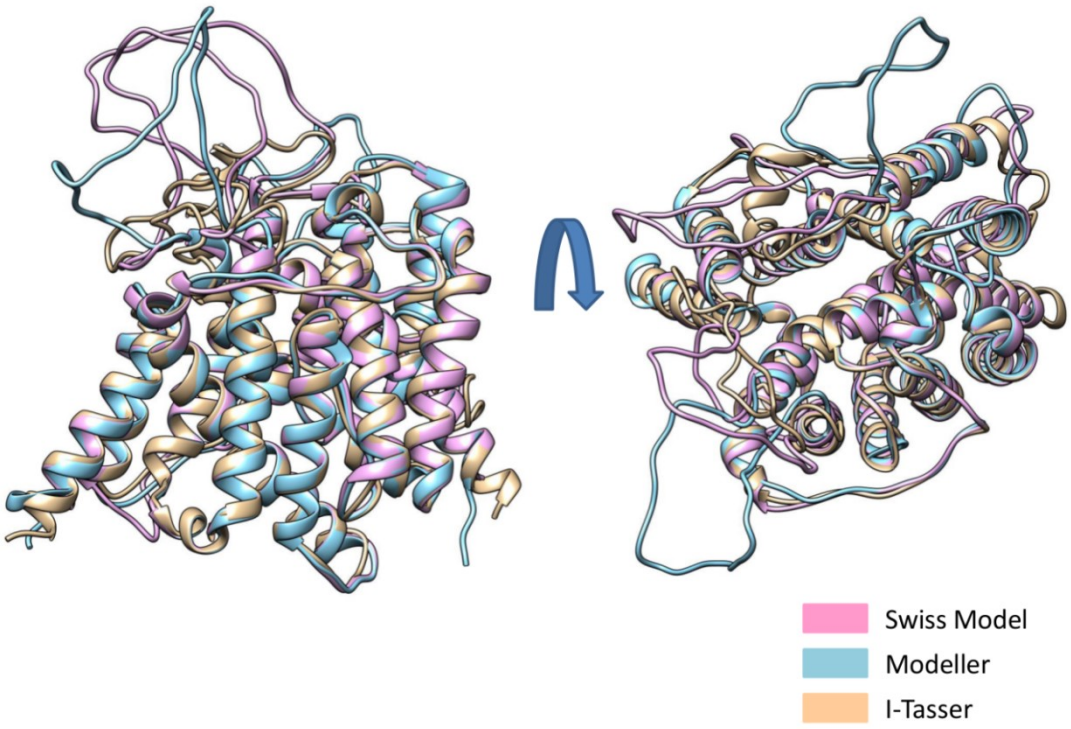

Figure 5 Superposition of pendrin structures obtained using different softwares.

The pendrin model (Fig. 6) is characterized by 14 TMs 12 of which are classic transmembrane α-helices, while the third and tenth TM present a peculiar structure (Fig. 6, panel A). In these segments, the α-helices are shorter and preceded by loops. In our model, the peculiar fold of TM3 and TM10 contributes to form a central cavity in the structure. The same cavity was experimentally determined in the SLC26Dg template and in UraA, where the antiparallel β-strands plays a fundamental role in the uracil transport mechanism (34). In UraA, the E290 residue located in TM10 is known to directly mediate uracil transport (34) while in SLC26Dg residues E38, E241 and Q287, located in TM1 and TM8, are supposed to form the fumarate binding site (3). Coherently with the different substrates specificity, these residues are not conserved in pendrin. Indeed, the pendrin model presents a Serine-Arginine pair (S408, R409) at

the position corresponding to the SLC26Dg G286 and Q287, which are suspected to mediate anion translocation through the transporter (33).

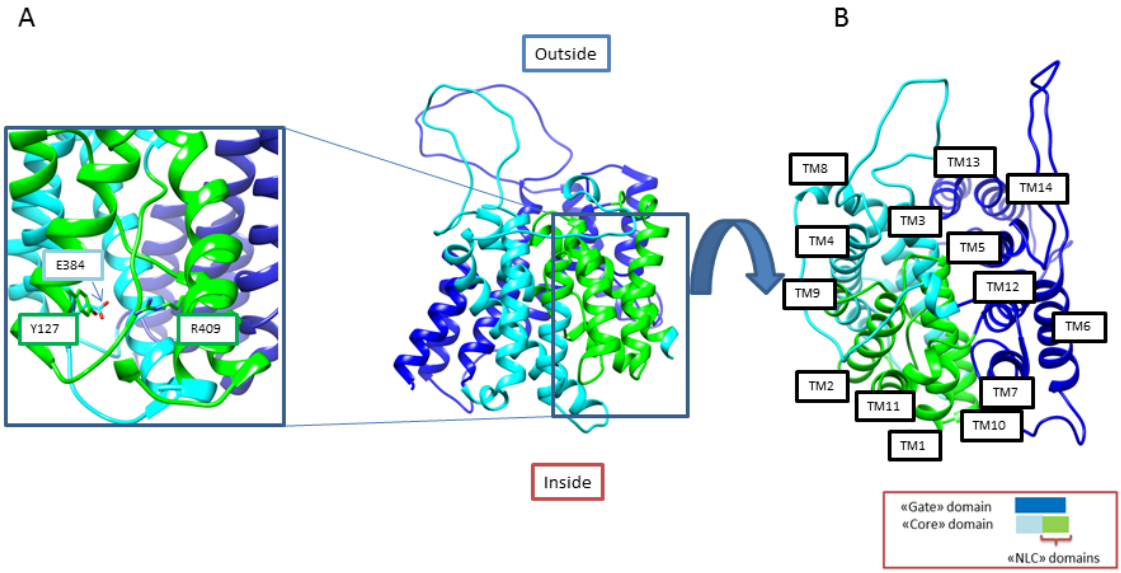

Figure 6 Representation of the pendrin model. The NLC domains are shown in green, the rest of the core domain in light blue and the gate domain in deep blue. A) Zoom on TM3 and T10 (TM11 is hidden) B) Transmembrane segments (TM) labelled and numbered from the N- to the C- terminus.

The TMDs topology obtained by homology modelling differs from the consensus of the transmembrane domain predictors. Although predicted TM residues are very similar in the 3D model and the TM consensus map, all prediction methods failed to predict TM10 and the majority of methods predicted TM13 and TM14 as a single TM domain.

A core and gate domain were found in both the prestin model and SLC26Dg crystal structure (Fig. 6). In pendrin, the core domain is composed of TM1-TM4 and TM8-TM11, while TM5-TM7 and TM12-TM14 form the “gate” domain. We believe that changes in the arrangement of the core and the gate domains allow the substrate binding site to be exposed to the two sides of the membrane, as also suggested for SLC26Dg (3) and UraA (153). The pendrin TM domain shows a tertiary structure pseudo-symmetry, with two groups of seven TM segments facing the two opposed

membrane sides. Sequence conservation mapped on the pendrin model shows that conserved regions in the structure are close to the exchanger core (Fig. 7).

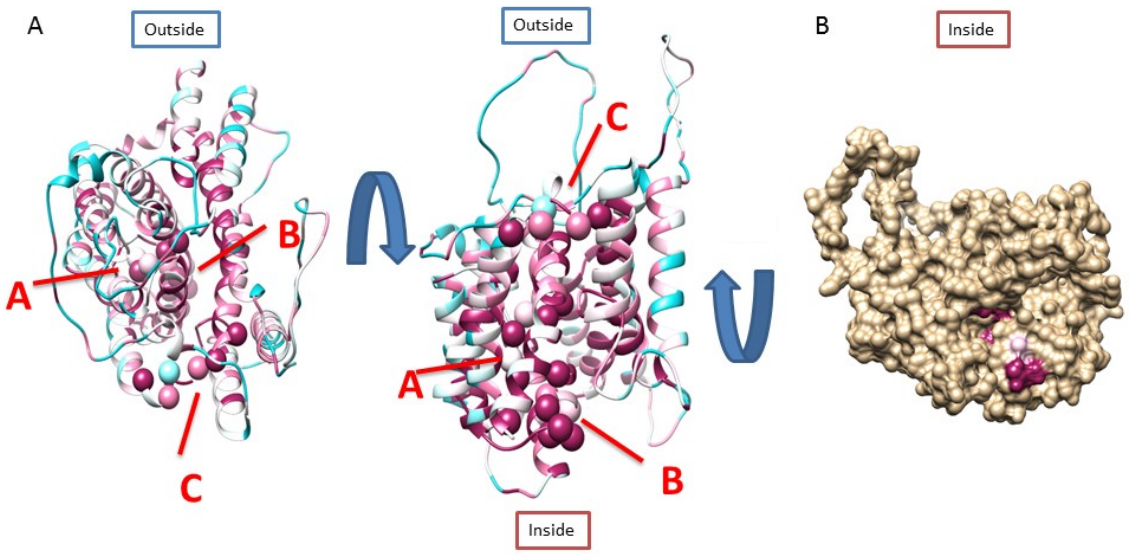

Figure 7 Panel A, 14 TM model coloured using the Consurf schema. Highly conserved residues are show in purple, and less conserved in light blue. Spheres show the location of mutations in clusters indicated with the letters A,B, C. Panel B, Mutated residues lining the central cavity (S93, T105, F141, P142, R409, V402, E414, N457) coloured using Consurf schema on the surface of the structure.

Indeed, as seen in prestin, the SulP and Saier motifs are close in structure and TM2 and TM9 are in direct contact. A sequence alignment between pendrin (UniProt accession: O43511-1) and prestin (UniProt accession: P58743) shows an overall global identity of 38%, raising to 58% and 41% when restricted to residues 89-142 and 393-448, corresponding to the functionally relevant prestin NLC1 and NLC2 domains (33,154). This suggests that the structurally peculiar TM3 and TM10 as much as the SulP and Saier motifs are involved in pendrin anion transport. As expected for a TM protein, amino acid composition for the membrane-facing surface is highly hydrophobic compared to the cytosolic and luminal portions (Fig. 8).

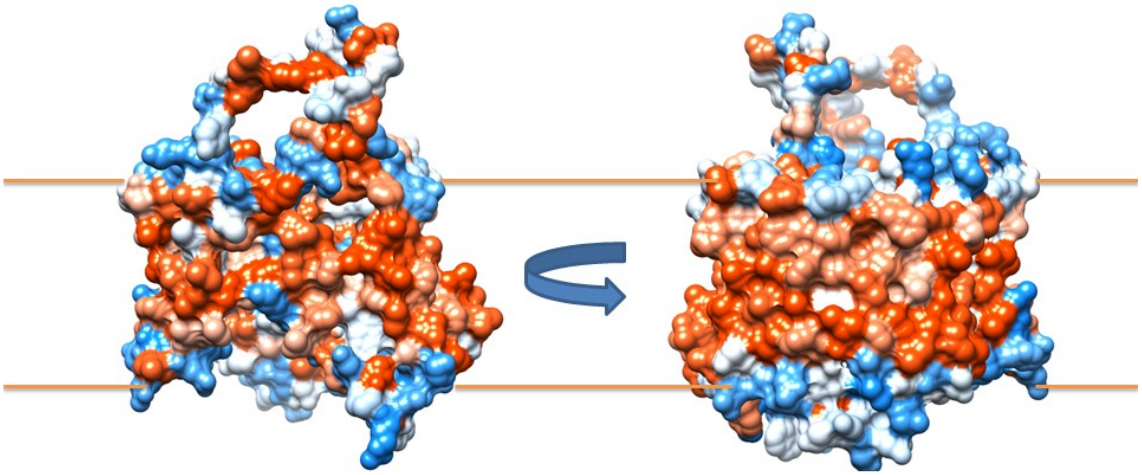

Figure 8 Hydrophobicity profile of pendrin. Red lines delimit the putative lipid bilayer. Pendrin hydrophobic and hydrophilic surfaces are shown in red and blue respectively.

3.1.5 Pathogenic mutations mapping

We mapped 147 pathological missense point mutations, found in patients with Pendred syndrome or ns-Eva, on the 3D TM domain model to gain insight about functionally relevant protein regions. The mutations were mostly found to affect residues oriented towards the TM center clustering between residues 89-142 and 393-448 (Figs. 8 and 9), forming three different clusters.

The ratio of pathogenic mutations within the region homologous to the prestin NLC domains and the entire TM domain was analyzed to investigate the functional role of these specific regions. We found 1 pathological mutation every 1.7 residues affecting NLCs, against a background of 1 mutation every 3.0 residues for the entire TM domain. As expected, structural positions of the mutation cluster vary depending on the considered topology. In the classical 12 TM topology model, mutations clusters at TM3 and in an extracellular loop between TM9 and TM10, as well as at the end of TM10 and the following cytosolic loop were found (Fig. 2). In our 14 TM topology model, the same clusters were found in TM3, TM10 and at the C-terminal of TM11 (Figs 7 and 9). This class of mutations is suspected to promote disease onset by affecting anion transport between TM3 and TM10, confirming the importance of TM3 and TM10 in SLC26 protein family (3,33). In particular, 35% of Pendred Syndrome-causative variants

localize within TM3 and TM10, suggesting that both regions are also functionally relevant for pendrin activity (Fig. 9).

A subset of 37 missense mutations has been previously tested for the ability to affect anion transport. We used the 3D model to analyze possible structural effects deriving from these amino acid substitutions to gain insight in the structure-function relationship (Tables 1 and 2). Twenty-nine missense mutations occur at conserved positions. Functional alteration is predicted to occur mainly through the following mechanisms: destabilization of the central core (e.g. L236P), steric hindrance or destabilization of the central loops (e.g. V138F), alteration of substrate binding site (e.g. R409H), altered local structural flexibility of TMs or loops involved in conformational changes (e.g. P123S), disruption of the GxxxG motif on TM14 (e.g. G497S). The energy variation induced by mutations was tested with NeEMO (155) and BLUUES (149) (see Table 1 and Table 2).

NeEMO predicts changes in internal folding energy and can be useful to identify highly destabilizing mutations. I chose this predictor because of the presence of transmembrane proteins in the training dataset. Indeed, predictor trained on dataset composed only of cytosolic protein (eg. Maestro (156)), may fail in predicting the change in stability upon mutations when applied to transmembrane proteins like pendrin.

BLUUES estimates the change in solvation energy for mutations on the protein surface, which can serve to estimate the effect on the surrounding lipids. The majority of the mutations tested show an increase in free energy which is consistent with reduced folding. A significant number of inner facing mutations cause a slightly reduction in total free energy, which may suggest a not folding-derived functional impairment.

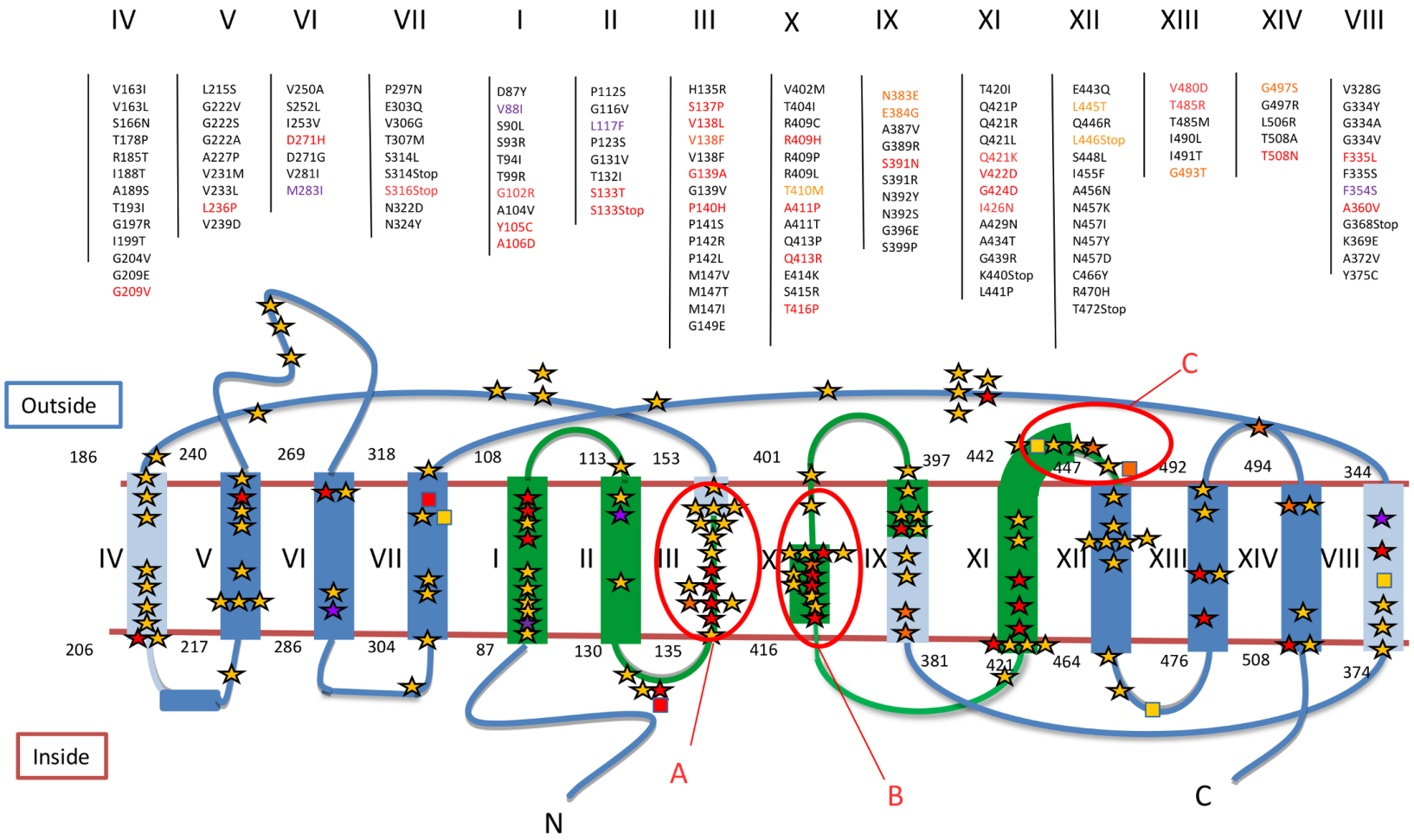

Figure 9. Mutation map on the 14 TM model. α-helices are indicated as rectangles, with the gate domain in blue, the core domain in light blue, and the NLC1 and NLC2 domains (part of the core domain) in green. The pathological mutations are listed above the corresponding α-helices. In α-helices domains point mutations are indicated with stars while stop codon mutations are indicated with a square. Colors change with the caused pathology: red for mutations found in Pendred syndrome, yellow for mutations found in ns-EVA, orange for mutations found in both. Purple denotes mutations with a mild phenotype. Mutation clusters are indicated with the letters A,B,C.

Table 1 Functionally tested mutations

Table 1. Summary of the 37 mutations tested experimentally. Missense mutations are listed with their affected nucleotide, exon and amino acid change followed by their location on the 14 TM model, conservation of the mutated residues (Cons.), and (where possible) predictions for stability with NeEMO and solvation with BLUUES. References are provided together with the cellular localization and functionality of each pathogenic variant. Where possible, a prediction of the molecular effect of the mutation based on the 14 TM model completes the information. The location column shows the position of the residue change in the 14 TM model, indicating for affected transmembrane segments whether the position is inward-looking (Inw) or lipid-exposed (Lip). The degree of conservation shown ranges from "-" (unconserved) to "+++" (highly conserved). Both NeEMO and BLUUES predict ΔΔG energies in Kcal/mol. The following acronyms are used for pathogenic effect: Pendred Syndrome (PS), enlarged vestibular aqueduct (EVA), non-syndromic hearing loss (NSHL). The cellular localization can be plasma membrane (PM), endoplasmic reticulum (ER) or intracellular (Intracell.).

Nucleoside change	Exon	Residue change	Protein Location	Cons.	NeEMO stability	BLUUES solvatation	Ref.	Pathogenic effect	Cell localization	Functionality	Predicted molecular effect
c.259G>T	3	p.Asp87Tyr	TM1 (Inw)	+++	-0.61		(157,158)	NSHL	PM	Reduction of formate uptake	Loss of a charge at the membrane interface.
c.279T>A	3	p.Ser93Arg	TM1 (inw)	++	-0.67		(157)	EVA	PM	Reduction of formate uptake	Insertion of a charged residue at the interface between gate and core.
c.296C>G	3	p.Thr99Arg	TM1 (Inw)	+	+0.5		(24)	EVA		Normal I^- transport	
c.304G>A	3	p.Gly102Arg	TM1 (Inw)	+++	+0.03		(159)	PS	ER	Loss of I^- efflux	Insertion of a charged residue in a hydrophobic region in the contact interface between TM1 and TM11
c.367C>T	4	p.Pro123Ser	TM2 (Inw)	+++	+1.22		(22,160,161)	NSHL	Intracell.	Loss of Cl^-/I^- exchange activity	Removal of proline-kink in TM2
c.412G>T	4	p.Val138Phe	TM3 (Inw)	+	-0.63		(159,162–164)	PS NSHL	ER	Loss of I- efflux	Interference with the transport mechanism
c.419C>A	5	p.Pro140His	TM3 (Inw)	++	+1.77		(165,166)	PS		Loss of I^- and cloride transport	Substitution of proline in central loops. Disruption of the local structure.
		p.Pro142Arg			-0.65		(23,167)			Loss of Cl^-	Substitution of

c.425C>T	5		TM3 (Inw)	++				EVA	Intracell.	/HCO_3^- exchange activity	proline in the loops disruption of the local structure.
c.439A>G	5	p.Met147Val	TM3 (Inw)	+++	+0.32		(22,160,167–169)	NSHL	Intracell.	Loss of Cl^- and I^- transport	Partial loss of local hydrophobic interaction
c.440T>C	5	p.Met147Thr	TM3 (Inw)	+++	+11.07		(24,167)	EVA	Intracell.	Loss of Cl^- /HCO_3^- exchange activity	Loss of local hydrophobic interaction
c.497G>A	5	p.Ser166Asn	Extracell. Loop	-	+0.12		(23,170)	EVA		Normal Cl^- /HCO_3^- exchange	
c.554G>C	5	p.Arg185Thr	Extracell. Loop	++	-0.19		(171–173)	PS	Intracell.	Reduction of I^- transport	Loss of a salt bridge with Asp182
c.626G>T	6	p.Gly209Val	Amphipatic helix	+++	+0.73		(159,162,164)	EVA NSHL PS	PM	Severe reduction of I^- transport	
c.665G>T	6	p.Gly222Val	TM5 (Inw)	+++	+1.17		(157)	EVA	PM	Reduction of formate uptake	Insertion of a side chain at the interaction interface of TM13
c.707T>C	6	p.Leu236Pro	TM5 (Lip)	+++		+0.08	(21,162,167,174,175)	PS NSHL	E.R.	Loss of I^- transport and Cl^- /I^- and Cl^- /HCO_3^- exchange activity	Insertion of a proline in α-helix
c.707T>C	6	p.Val239Asp	TM5 (Inw)	++	-0.05		(20,176,177)	PS NSHL	E.R.	Severe reduction of Cl^- and I^- transport	Disruption of an hydrophobic interaction between TM5 and TM6
c.907G>C	7	p.Glu303Gln	TM7 (Inw)	+++	+0.17		(178,179)	EVA	PM	Loss of Cl^-/I^- and Cl^-/HCO_3^- exchange activity	
c.941C>T	8	p.Ser314Leu	TM7 (Inw)	+++	-0.04		(157)	NSHL	Intracell.	Reduction of formate uptake	
c.1003T>C	9	p.Phe335Leu	External loop	+	-0.5		(180,181)	PS	PM	Reduction of Cl^- /I^- and Cl^- /HCO_3^- exchange activity	
c.1079C>T	9	p.Ala360Val	TM8 (Inw)	+++	+0.7		(157,169,182,183)	PS		Reduction of formate uptake	Larger side chain destabilization of the central loops
c.1105A>G	9	p.Lys369Glu	TM8 (Inw)	-	-0.43		(22,160,161)	EVA		Normal Cl^-/I^- exchange	Maintenance of a charged reside at the cytosolic interface.
c.1115C>T	9	p.Ala372Val	TM8	++	+0.73		(22,160,161)	EVA		Reduction in the	

			(Inw)							Cl^-/I^- exchange	
.1151A>G	10	p.Glu384Gly	TM9 (Inw)	+++	+1.82		(21,167,174,175,184)	PS NSHL	ER Intracell.	Loss of Cl^- and I^- uptake	Loss of H bonds between Glu384 and Tyr127. Necessary for TM9 and TM2 interaction.
c.1174A>T	10	p.Asn392Tyr	TM9 (Inw)	+++	-0.32		(160,169,176,185,186)	NSHL	Intracell.	Reduction in the Cl^-/I^- exchange	Clashes in the protein core.
c.1204G>A	10	p.Val402Met	TM10 (Inw)	+	+0.29		(181)	EVA	Intracell.	Loss of Cl^-/I^- and Cl^-/HCO_3^- exchange activity	Clashes in the protein core.
c.1225C>T	10	p.Arg409Cys	TM10 (Inw)	+++	+0.48		(157)	EVA	Intracell.	Loss of formate uptake	Loss of Arg409 putatively involved in anion binding
c.1226G>A	10	p.Arg409His	TM10 (Inw)	+++	+1.43		(32,162,185,187,188)	PS	Partially PM	Reduction of Cl^- and I^- transport, loss of I^- efflux	Loss of Arg409 but partial conservation of the positive charge.
c.1229C>T	10	p.Thr410Met	TM10 (Inw)	++	-1.02		(159,164,169,178,184,185,189,190)	PS NSHL	ER	Loss of I^- efflux	Alteration of the anion binding site
c.1238A>C	10	p.Gln413Pro	TM10 (Inw)	++	-0.61		(165,166)	PS		Loss of cloride and I^- transport	Insertion of a proline in the α helix
c.1246A>C	10	p.Thr416Pro	Cytosolic Interface	+++	-0.49		(21,162,164,167,174,175)	EVA	ER Intracell.	Loss of Cl^- and I^- uptake	Insertion of a proline in the loop
c.1271G>A	11	p.Gly424Asp	TM11 (Inw)	+++	+0.42		(165,166)	PS		Reduction of Cl^- and I^- transport	H Bond with His135 and destabilization of the internal loops
c.1334T>G	11	p.Leu445Trp	External Loop	+++	+1.31		(162–164,168,181)	PS NSHL	Intracell.	Loss of Cl^- and I^- transport	Change in the steric hindrance
c.1337A>G	11	p.Gln446Arg	External Loop	+	+0.10		(159,191)	EVA	ER	Loss of I^- efflux	Insertion of a charged residue
c.1439T>A	13	p.Val480Asp	TM13 (Lip)	+		-18.89	(21)	PS		Reduction of Cl^- and I^- uptake	Charged residue lipid facing
c.1454C>G	13	p.Thr485Arg	TM13 (Inw)	+	-0.46		(165,166)	PS		Reduction of C^{l-} and I^- transport	Disruption of the interaction between TM13 and TM5
c.1468A>C	13	p.Ile490Leu	TM13 (Lip)	++	-0.49		(21,192)	EVA		Mild reduction of Cl^- and I^- uptake	
c.1517T>G	13	p.Leu506Arg	TM14 (Lip)	++	-0.11		(157)	EVA	PM	Reduction of formate uptake	Insertion of a lipid facing charged residue

Table 2 not functionally tested mutations

Table 2. Summary of SLC26A4 missense variants without experimentally validated functional information. Missense mutations are listed with their affected nucleotide, exon and amino acid change followed by their location on the 14 TM model, conservation of the mutated residues (Cons.), and (where possible) predictions for stability with NeEMO and solvation with BLUUES. References are provided for the origin of each variant and their pathogenic effect is indicated. Where possible, a prediction of the molecular effect of the mutation based on the 14 TM model completes the information. The location column shows the position of the residue change in the 14 TM model, indicating for affected transmembrane segments whether the position is inward-looking (Inw) or lipid-exposed (Lip). The degree of conservation shown ranges from "-" (unconserved) to "+++" (highly conserved). Both NeEMO and BLUUES predict ΔΔG energies in Kcal/mol. The following acronyms are used for pathogenic effect: Pendred Syndrome (PS), enlarged vestibular aqueduct (EVA), non-syndromic hearing loss (NSHL), sensorineural deafness with palmoplantar lichen planus (SDPLP).

Nucleoside change	Exon	Residue change	Protein location	Cons.	NeEMO stability	BLUUES solvatation	Ref.	Pathogenic effect	Predicted molecular effect
c.262G>A	3	p.Val88Ile	TM1 (Lip)	++		+0.74	(20,165)	Benign	Maintenance of lipid facing Hydrophobic reside
c.269C>T	3	p.Ser90Leu	TM1 (Inw)	+++	-0.84		(176)	NSHL	Loss of H bond with Asp87
c.281C>T	3	p.Thr94Ile	TM1 (Inw	+++	-1.17		(179)	EVA	Loss of H bond with Ser427 of TM12
c.311C>T	4	p.Ala104Val	TM1 (Inw)	+++	+0.28		(193)	NSHL	Clash with Val454
c.314A>G	4	p.Tyr105Cys	TM1 (Inw)	++	+1.45		(180)	PS	Loss of hydrogen bond with Asn457.
c.317C>A	4	p.Ala106Asp	TM1 (Inw)	+++	+1.08		(180)	PS	Disruption of the interaction between TM2 and TM3
c.334C>T	4	p.Pro112Ser	Extracellular Loop	+++	+0.09		(179)	EVA	Loss of conserved proline
c.340G>A	4	p.Gly114Arg	TM2 (Inw)	-	-0.73		(194)	EVA	Addition of a charge in a hydrophobic poket
c.347G>T	4	p.Gly116Val	TM2 (Inw)	+++	-0.63		(195)	NSHL	Disruption of Gly-Gly interaction with Gly92 of TM1
c.349C>T	4	p.Leu117Phe	TM2 (Inw)	+++	1.37		(196)	Benign (in silico)	Maintenace of the hydrophobicity
c.392G>T	4	p.Gly131Val	Cytoplasmic Loop	+++	-0.01		(197)	NSHL	Clash with Tyr 127
c.395C>T	4	p.Thr132Ile	Cytoplasmic Loop	+++	-0.58		(198)	NSHL	Loss of H bond with Asp380
c.397T>A	4	p.Ser133Thr	Cytoplasmic Loop	+++	+0.62		(199)	PS	

c.398C>A	4	p.Ser133Stop	Cytoplasmic Loop	+++		(164,200)	PS	Protein truncation
c.404A>G	4	p.His135Arg	TM3 (Inw)	+++	+1.62	(185)	EVA	Putative anion binding site
c.409T>C	4	p.Ser137Pro	TM3 loop (Inw)	+++	-0.67	(200)	PS	Loss of anion binding cooperation?
c.412G>C	4	p.Val138Leu	TM3 loop (Inw)	+	-1.14	(201)	PS	Change in the lateral chain steric hindrance in the central loops.
c.413T>A	4	p.Val138Asp	TM3 loop (Inw)	+	+0.01	(158)	NSHL-EVA	Destabilization of the central loops.
c.416G>C	5	p.Gly139Ala	TM3 (Inw)	+++	-0.15	(162)	PS	Change in the lateral chain steric hindrance in the central loops.
c.416G>T	5	p.Gly139Val	TM3 (Inw)	+++	+0.25	(202)	NSHL	Change in the lateral chain steric hindrance in the central loops.
c.422T>C	5	p.Phe141Ser	TM3 (Inw)	+++	+3.12	(203)	NSHL	Loss of Pi stack between Phe141 and Pro142
c.425C>G	5	p.Pro142Leu	TM3 (Inw)	++	-1.20	(163)	EVA	Loss of Pi stack between Phe141 and Pro142
c.441G>A	5	p.Met147Ile	TM3 (Inw)	+++	+0.02	(204)	EVA	
c.446G>A	5	p.Gly149Glu	TM3 (Inw)	+++	-0.75	(163)	EVA	Disruption of hydrophobic interaction between TM3 and TM1
c.487G>A	5	p.Val163Ile	Extracellular Loop	-	-0.48	(197)	EVA	Interference with the glycosilatyon site Asn 167N?
c.487G>C	5	p.Val163Leu	Extracellular Loop	-	-0.27	(170)	NSHL	Interference with the glycosilatyon Asn 167N?
c.532A>C	5	p.Thr178Pro	Extracellular Loop	-	+0.35	(205)	EVA	Insertion of a proline, interference with glycosilatyon site Asn 172N?
c.554G>C	5	p.Ile188Thr	TM4 (Inw)	++	+1.38	(169)	EVA	Insertion of a polar residue in a hydrophobic pocket.
c.349C>T	5	p.Ala189Ser	TM4 (Inw)	++	+1.30	(196)	Benign	Tolerate insertion of a polar residue in a hydrophobic pocket
c.578C>T	5	p.Thr193Ile	TM4 (Inw)	+	-1.15	(163,206)	PS NSHL	Lost of H bond with Phe401 Ile383
c.589G>A	5	p.Gly197Arg	TM4 (Inw)	+++	-0.11	(169,179)	EVA	Disruption of the interaction between TM5 and TM9
c.596T>C	5	p.Ile199Thr	TM4 (Inw)	++	+0.90	(24)	EVA	Disruption of hydrophobic interaction with TM8
c.611G>T	6	p.Gly204Val	TM4	+++	-0.26	(179)	EVA	Disruption of the Gly interaction between TM4 and TM10
c.626G>A	6	p.Gly209Glu	Amphipatic helix	+++	+0.47	(179)	EVA	Clashes with TM11 and TM12

c.644T>C	6	p.Leu215Ser	Intracellular loop	+++	+0.42		(197)	EVA	Formation of H bond with Ala131
c.664G>A	6	p.Gly222Ser	TM5 (Inw)	+++	+0.72		(170)	NSHL	Formation of hydrogen bond withThr485 or Cys486
c.665G>T	6	P.Gly222Ala	TM5 (Inw)	+++	+0.57		(197)	EVA	Insertion of a side chain at the interaction interface of TM13
c.668T>C	6	p.Phe223Ser	TM5 (Inw)	+++	+2.22		(207)	NSHL	Insertion of a polar residue in a hydrophobic pocket.
c.679G>C	6	p.Ala227Pro	TM5 (Inw)	+++	+0.67		(186)	NSHL	Insertion of a proline in the α helix
c.691G>A	6	p.Val231Met	TM5 (Inw)	++	-0.32		(202)	NSHL	Clashes in the protein core.
c.697G>C	6	p.Val233Leu	TM5 (Inw)	+	-0.40		(208)	NSHL	
c.749T>C	6	p.Val250Ala	External loop	+	+0.38		(178)	NSHL	
c.754T>C	6	p.Ser252Pro	External loop	++	+0.38		(169,176,186)	NSHL	Reduction of the loop flexibility
c.757A>G	6	p.Ile253Val	External loop	++	+0.52		(157,170)	NSHL	
c.811G>C	7	p.Asp271His	TM6 (Inw)	-	+0.16		(162)	PS	Loss of a salt bridge with Lys447
c.812A>G	7	p.Asp271Gly	TM6 (Inw)	-	+0.30		(179)	EVA	Loss of a salt bridge with Lys447
c.841G>A	7	p.Val281Ile	TM6 (Inw)	++	-0.41		(172)	NSHL	
c.849G>C	7	p.Met283Ile	TM6 (Lip)	++		+1,13	(196)	Benign (in silico)	Maintenance of a hydrophobic lipid facing residue.
c.890C>A	7	p.Pro297Gln	Intracellular loop	-	-0.20		(161)	EVA	Loss of a Proline in the loop
c.917T>G	7	p.Val306Gly	TM7	++	+ 3.55		(205)	NSHL	Insertion of a Gly in alpha helix
c.920C>T	8	p.Thr307Met	TM7 (Inw)	+	-1.06		(24)	EVA	
c.941C>A	8	p.Ser314Stop					(209)	NSHL	Protein truncation
c.946G>T	8	p.Gly316Stop					(169,178)	PS	Protein truncation
c.964A>G	8	p.Asn322Asp	External loop	-	+0.34		(196)	Benign (in silico)	
c.970A>T	8	p.Asn324Tyr	External loop	++	+0.63		(196)	Benign (in silico)	
c.983T>G	8	p.Val328Gly	External loop	++	+0.71		(197)	EVA	
c.1000G>T	8	p.Gly334Trp	External loop	+++	+1.95		(194)	EVA	
c.1001G>C	8	p.Gly334Ala	External loop	+++	+2.31		(210)	NSHL	
c.1001G>T	8	p.Gly334Val	External loop	+++	+2.86		(211)	NSHL	

c.1004T>C	9	p.Phe335Ser	External loop	+	+7.49	(212)	EVA	
c.1061T>C	9	p.Phe354Ser	TM8 (Lip)	+		(196)	Benign (in silico)	
c.1102G>T	9	p.Gly368Stop				(188)	NSHL	Protein truncation
c.1124A>G	9	p.Tyr375Cys		++	-0.58	(178)	NSHL	Lost of pi stack with Tyr 371
c.1147C>G	9	p.Gln383Glu	TM9 (Lip)	+++		(213)	PS NSHL	Insertion of a negative charge at the citosololic membrane interface
c.1160C>T	10	p.Ala387Val	TM9 (Inw)	+++	+1.11	(214)	EVA	Larger side chain cause clashes with TM2
c.1165G>C	10	p.Gly389Arg	TM9 (Inw)	+++	-0.35	(164)	EVA	Disruption of the interaction site between TM9 and TM4
c.1172G>A	10	p.Ser391Asn	TM9 (Inw)	+	-0.32	(200)	PS	Formation of a H-bond with Thr126
c.1173C>A	10	p.Ser391Arg	TM9 (Inw)	+	-0.53	(24)	EVA	Charged residue in a hydrophobic pocket. Disruption of the arrangement of the central loops
c.1174A>T	10	p.Asn392Ser	TM9 (Inw)	+++	+0.38	(179)	EVA	Loss of H-bond with Ala403
c.1187G>A	10	p.Gly396Glu	TM9 (Inw)	++	-0.72	(161)	EVA	Disruption of the interaction between TM9 and TM4
c.1195T>C	10	p.Ser399Pro	Extracellular loop	-	-1.28	(32)	NSHL	Change of the local flexibility
c.1211C>T	10	p.Thr404Ile	TM10 loop (Inw)	++	-0.84	(194)	EVA	Clashes in the protein core.
c.1226G>C	10	p.Arg409Pro	TM10 (Inw)	+++	+0.53	(176)	NSHL	Loss of Arg409 putatively involved in anion binding
c.1226G>T	10	p.Arg409Leu	TM10 (Inw)	+++	-0.37	(197)	EVA	Loss of Arg409 putatively involved in anion binding
c.1231G>A	10	p.Ala411Thr	TM10 (Inw)	+	-0.26	(215)	EVA	Formation of a new H-bond with Leu407.
c.1231G>C	10	p.Ala411Pro	TM10 (Inw)	+	-0.51	(216)	PS	Insertion of a proline in the α helix
c.1238A>G	10	p.Gln413Arg	TM10 (Inw)	++	-0.56	(169,179,217)	NSHL	Loss of a H bonds with TM1, Ser432 and Tm12, Ser90. Disruption of local folding
c.1240G>A	10	p.Glu414Lys	TM10 (Inw)	+++	-0.02	(157)	EVA	Charge inversion loss of Salt bridge with Lys374
c.1245C>A	10	p.Ser415Arg	TM10 (Inw)	+++	-0.08	(157)	EVA	Charge insertion
c.1259C>T	10	p.Thr420Ile	Cytosolic loop	+++	+0.27	(211)	NSHL	
c.1261C>A	10	p.Gln421Lys	TM11 (Inw)	+++	-0.44	(218)	PS	Charge insertion
c.1262A>C	10	p.Gln421Pro	TM11 (Inw)	+++	-0.51	(164,179)	EVA	Insertion of a proline in the α helix
c.1262A>G	10	p.Gln421Arg	TM11	+++	-0.52	(193)	NSHL	Charge insertion

			(Inw)						
c.1262A>T	10	p.Gln421Leu	TM11 (Inw)	+++	-0.57		(24)	EVA	
c.1265T>A	11	p.Val422Asp	TM11 (Lip)	++		+15,17	(218)	PS	Charged residue lipids facing
c.1277T>A	11	p.Ile426Asn	TM11 (Lip)	-	+2.01		(158)	PS	Polar residue Lipid facing
c.1286C>A	11	p.Ala429Glu	TM11 (Lip)	++		+22,44	(169)	EVA	Charged residue Lipid facing
c.1300G>A	11	p.Ala434Thr	TM11 (Lip)	+	-0.14		(161,219)	SDPLP	Polar residue Lipid facing
c.1315G>A	11	p.Gly439Arg	External anphipatic helix	+++	+0.25		(161,220)	NSHL	Charged residue in hydrophobic region.
c.1318A>T	11	p.Lys440Stop	External anphipatic helix	-			(179)	EVA	Protein truncation
c.1322T>C	11	p.Leu441Pro	External anphipatic helix	+++	+0.16		(212)	EVA	Insertion of a proline in the α helix
c.1327G>C	11	p.Glu443Gln	External Loop	-	-0.02		(157)	EVA	Loss of salt bridge wiht Lys440
c.1336C>T	11	p.Gln446Stop	External Loop	+			(179)	NSHL PS	Protein truncation
c.1343C>T	12	p.Ser448Leu	TM12 (Inw)	++	-0.94		(214)	EVA	Loss of H-bond with Asp271
c.1363A>T	12	p.Ile455Phe	TM12 (Lip)	++	+0.18		(176)	NSHL	
c.1367C>A	12	p.Ala456Asp	TM12 (Inw)	++	-0.15		(170)	NSHL	Disruption of the intarction with TM6
c.1369A>G	12	p.Asn457Asp	TM12 (Inw)	+++	-0.02		(208)	NSHL	Residue putatively involve in the movement of the gate domain
c.1369A>T	12	p.Asn457Tyr	TM12 (Inw)	+++	-0.41		(203)	NSHL	Residue putatively involve in the movement of the gate domain
c.1370A>T	12	p.Asn457Ile	TM12 (Inw)	+++	-1.29		(170)	NSHL	Residue putatively involve in the movement of the gate domain
c.1371C>A	12	p.Asn457Lys	TM12 (Inw)	+++	-0.25		(176)	NSHL	Residue putatively involve in the movement of the gate domain
c.1397G>A	12	p.Cys466Tyr	Loop	-	+0.25		(170)	NSHL	
c.1409G>A	12	p.Arg470His	Loop	-	+0.05		(221)	NSHL	
c.1415G>A	12	p.Trp472Stop	Loop		-0.05		(170)	NSHL	
c.1454C>T	13	p.Thr485Met	TM13 (Inw)	+	-1.22		(222)	EVA	Disruption of the interaction between TM13 and TM5
c.1472T>C	13	p.Ile491Thr	TM 13	+	-0.30		(221)	NSHL	Protein truncation
c.1477G>T	13	p.Gly493Trp	Loop	+++	-0.08		(213)	PS NSHL	Loss of the Glycine
c.1489G>A	13	p.Gly497Ser	TM14 (Inw)	+++	0.17		(21,167,192)	EVA PS	Disruption of GXXXG motif

c.1489G>C	13	p.Gly497Arg	TM14 (Inw)	+++	0.13	(223)	EVA	Disruption of GXXXG motif
c.1522A>G	13	p.Thr508Ala	TM14	+++	-0.12	(197)	EVA	
c.1523C>A	13	p.Thr508Asn	TM14	+++	-0.09	(223)	PS	Disruption of the interaction between TM13 e TM14

3.1.6 Discussion

The X-ray-based structure determination of transmembrane proteins is challenging due to the peculiar structural and physicochemical proprieties, and to the fact that only a limited number of structures is available (224). This work aimed at generating a novel structural model, at gaining insight into the pendrin structure-function relationship, and at studying the pathogenic role of mutations present in Pendred Syndrome and ns-EVA patients. In particular, we have characterized the topology of the TM domain by *in silico* structural analysis. One of the most critical aspects of current pendrin models is the exact assignment of TM segments. Experimental procedures (e.g. x-ray crystallography) generally fail to solve transmembrane proteins due to their hydrophobic nature and TM prediction tools still have difficulty to predict the correct TM topology (114). Furthermore, TM topology does not provide information on 3D TM arrangement relative to the membrane. Several different pendrin models were presented in the literature (15,31,187). The most used model counts 12 TM segments, while several authors proposed alternative topologies (30,187), all generated by single TM predictors. Our novel pendrin TM domain homology model uses the very recent SLC26Dg protein crystal structure as template (3). The approach we adopted to build the model included construction of a TM consensus map of pendrin, based on the convergence of at least five different predictors. This was used to refine a MSA for both template search and target-template alignment in homology modeling. SLC26Dg shows only 19% sequence identity with the pendrin TM region, even though it is a member of the SLC26/SulP protein family. Comparison between the predictor consensus and our homology model revealed a good agreement in the definition of the TM-forming residues, confirming a large part of the model, except for a discrepancy in TM segment number. TM13 and

TM14 are predicted as a single TM, while TM10 is not predicted. Our model shows a short loop separating the TM13 from TM14, while TM10 was predicted as a non-canonical TM helix, instead of forming a “loop” followed by a short α-helix. The short coil between TM13 and TM14, as well as the unusual topology of TM10, are probably the reason why predictors fail to recognize the two TM domains (225).

Pathological mutations were mapped on our novel 14 TM model. We found known pathological mutations to cluster in two regions corresponding to the functionally relevant prestin NLC domains. Based on the proposed topology, pathological pendrin mutations are gathered in TM3 and TM10, as well as in TM11, suggesting their relevance for pendrin activity. TM3 and TM10 are also found to be non-canonical TM α-helices. Discontinuous helices are also found in other ion transporters, such as NhaA (226) and $LeuTA_a$ (227). In these proteins, the discontinuity has a fundamental role for the recognition of different ions and for substrate binding, conferring the required flexibility at a lower energy cost than an α-helix (228). SLC26Dg and UraA, the only two experimentally solved structures related to the SLC26 family, have a short antiparallel β-strand in TM3 and TM10 instead of the loops predicted by our model. Future studies will clarify the exact structure of these two regions, in particular, whether absence of the central β-strands in pendrin is a modeling artifact or a real peculiarity of pendrin. This may be due to P142 being located in correspondence of the β-strands present in the homologous structures. The structural rigidity of proline may alter the conformation yielding the two loops predicted by our model. The TM segments show an inverted repetition. Pseudo-symmetry is a common feature of TM proteins as half of the all known transmembrane proteins contain internal symmetrical repeats (229). In particular for ion transporters, it was suggested that inverted repeats help the protein to assume the inward and outward conformations (230). A “gate “ and “core” domain are distinguished in the structure and involved in conformational change.

Using the model, we discuss the role of 37 functionally tested pathological mutations (Table 1). For most mutations it was possible to propose a molecular mechanism explaining the observed altered anion transport. As expected, pathological mutations were found mostly facing towards the protein interior, due to the higher probability for a mutated residue to have a pathological effect when altering the protein core than

by contacting lipids. Lipid facing mutations, tested with BLUUES, promote relevant changes in solvation energy, confirming a disruptive effect on hydrophobic interactions with lipid bilayer. Most loss of function mutations are predicted by NeEMO to destabilize the protein and cause unfolding, coherently with different papers suggesting retention of improperly folded pendrin mutants in the endoplasmic reticulum as the major pathological mechanism for Pendred syndrome (231,232). The remaining inner facing mutations showed slight reduction in total free energy, probably affecting the protein functionality, but with weaker effects on protein stability. In SLC26Dg the central cavity residues E38, E241 and Q287 (located in TM1, TM8 and TM10) are supposed to form the fumarate binding site, while their role in proton symport remains to be elucidated (3). These residues are not conserved in pendrin, which presents Q101 and V367 at the same position. This arrangement in turn may explain the absence of fumarate-proton symport activity. Q287 is substituted by R409 in the pendrin model. Based on the anion binding mechanism previously proposed for prestin (33), we believe that R409 is located at the cavity center, where it mediates anion entrance. For this reason, the substitutions with three different amino acids (R409H, R409C and R409P, respectively) are of particular interest, because they are causative of both Pendred syndrome and ns-EVA. Functional assays performed on R409H show a detectable activity reduction not coupled with complete functional impairment (187). R409H does not abolish the positive charge, but may introduce a relevant pH dependence yielding a reduction in activity. This finding also suggests that a positive charge in this position is an important factor for pendrin function. Our data suggest that regions regulating core and gate mobility are mutation hotspots. Indeed, mutations affecting residues S93, T105, F141, P142, V412, E414, N457 are located in the central cavity at the cytosolic site. Similarly, pathogenic mutations were found at the C-terminus of TM11 at the extracellular membrane side between the gate and core domains (Fig. 8). These two regions were suggested to have a relevant role in anion binding as well as core and gate gating regulation.

The non-canonical transmembrane segments formed by TM3 and TM10 are delimited by TM2 and TM9, where the conserved Y127 residue belonging to the “Saier motif” and E384 in the SUL1 domain interact with each other to stabilize the protein fold.

Mutation E384G is known to cause Pendred syndrome, yielding a phenotype characterized by complete loss of Cl^- and I^- uptake (187), confirming the structural role of this residue in maintaining activity. Five pathogenic mutations are located at the C-terminus of TM11, between the gate and core domains, and their position suggests a specific role in regulating opening/closing.

Mutations in the GxxxG region suggest this specific motif to play a functional/structural role in pendrin dimerization. In membrane proteins, the GxxxG motif is known to facilitate oligomerization and to help proteins reaching the correct fold (97). In the case of pendrin, GxxxG containing domain was associated with protein dimerization (187). While pendrin appears to be mostly monomeric under physiological conditions, a dimeric form was observed by sucrose gradient centrifugation (233). Of note, oligomerization was also reported for the bacterial SLC26 protein structures (234,235). Although prestin C415 plays a role in protein oligomerization (236), we did not find relevant conservation in the phylogenetic tree for the four pendrin cysteines located in the TM domain, and only mutation C466Y is reported as pathogenic. Finally, considering the good fit between our novel 3D model, the location of mutations and hydrophobicity profile, we believe that this study will be useful to future works aimed to shed light on pendrin function.

3.2 Mitochondrial Permeabilty Transition Pore

3.2.1 Aim of the project

We tried to answer two key questions, i.e. where in F-ATP synthase is the Ca^{2+} binding site that triggers PTP opening, and which subunits are involved in the opening signal transmission and channel formation.

Matrix Ca^{2+} is a necessary trigger of the PTP opening while Mg^{2+}, Sr^{2+}, Mn^{2+} and Ba^{2+} cause an inhibition of PTP activation, suggesting competition for the same divalent metal ion (Me^{2+}) binding site (237,238). Six Me^{2+} binding sites are located in the F_1 domain of F-ATP synthase. Three catalytic Me^{2+} binding sites are located at the αβ subunits interface while other three non-catalytic Me^{2+} binding sites are at the opposite face of αβ protomers. Efficient ATP catalysis requires the binding of the nucleotide complex with Mg^{2+} to both catalytic and non catalytic binding sites.

In the α-proteobacterium *Rhodospirillum rubrum* it has been possible to modulate the relative affinity for Ca^{2+} and Mg^{2+} of F-ATP synthase with a T159S point mutation at the β subunit, which decreased Ca^{2+}-ATPase and increased Mg^{2+}-ATPase activity (63,239). This same threonine residue (T163 in the bovine sequence) was also shown to play a key role in coordinating Mg^{2+} in the catalytic site of the bovine enzyme during ATP hydrolysis (77), suggesting that it might affect the relative affinity for Me^{2+} in the mammalian β subunit as well. Indeed, experimental evidence in cells and in zebrafish embryos confirms the effect of the T163S mutation of β subunit, as the mutation results in resistance to PTP opening (5). To clarify the molecular effect of the Ca^{2+} binding and of T163S mutation on F-ATP synthase, we performed MD on four F-ATP synthase models (WT and T163S binding Mg^{2+} or Ca^{2+}). Our expectation was that simulations should highlight key differences, allowing in turn to make predictions on the mechanism through which F-ATP synthase can turn into a channel upon Ca^{2+} binding. We speculated that OSCP, known to be the target of PTP regulators, could

transmit the opening signal through the lateral stalk in the membrane region so we focused the analysis on the interactions between OSCP and the F_1 domain.

Furthermore, to answer the question of how is the signal transmitted by OSCP to the membrane region and which are the pore forming subunit a phylogenetic analysis was performed. A PTP was demonstrated in yeast (240), *Drosophila melanogaster* (62), mammals (4,102) and appears to be a feature of all eukaryotes (40), yet differences in several features including conductance were found in different species. For these reasons it could be speculated that while PTP constituents have to be conserved in eukaryotes they should be sufficiently divergent to explain the different dimensions of the pore. Starting from these assumptions I investigated the conservation of putative pore forming subunits across organisms using MSA and building phylogenetic trees.

Previous studies (240) show that the deletion of the e or/and g subunits in yeast induces a relative resistance to opening of the pore. The e and g subunits were characterized *in silico* to identify putative functionally important residues. Subsequently I expanded my analysis to the b and f subunits. A phylogenetic tree made of 228 sequences was built for b subunit. For each organism of the tree the presence of e, g and f subunit was investigated.

3.2.2 The four F-ATP synthase systems

Wild type and mutant F-ATP synthase structures described in the Material and Method section were used for MD simulation. Two metals were tested in the Me^{2+} nucleoside binding sites: Mg^{2+} (originally present in the protein structure) and Ca^{2+}. The average distance between the cation and the coordinating amino acids changes depending on the Me^{2+}, due to their different van der Waals radii (Fig. 10). This difference is present with both the adenosine nucleosides.

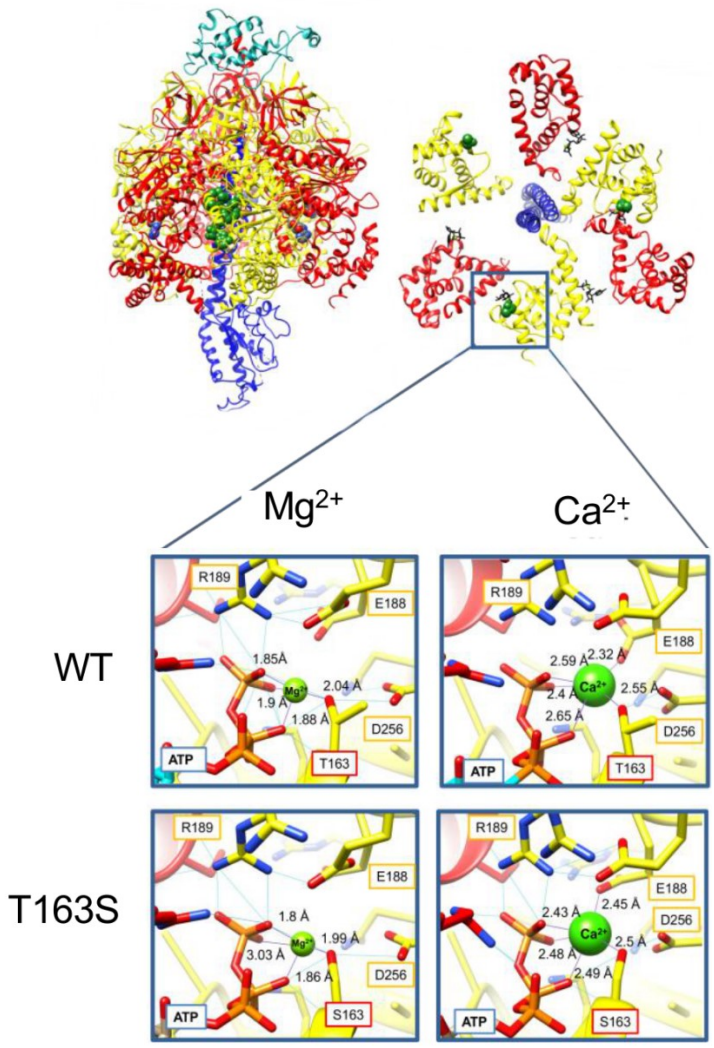

Figure 10 Lateral and top view of F_1; location of β T163 is marked by green spheres. Red, α subunits; yellow, β subunits; blue, γ subunit; turquoise, OSCP (lateral view only). The enlargement shows Mg^{2+} and Ca^{2+} bound to the Me^{2+} sites and their coordination distances. Hydrogen bonds and ion contacts are shown in blue and purple, respectively, with the distance between ion and coordinating atoms in Å.

3.2.3 Root Mean Square Deviation

Root Mean Square Deviation (RMSD) represents the structural variation between each frame of the dynamics and the starting T_0 structure. RMSD gives information about the stability of the simulated system. Indeed, if the simulated system results stable the RMSD reaches a plateau in which RMSD fluctuations remain constant during time.

The RMSD values calculated for each system (Fig. 11) present an exponential grow in the first 7ns of simulation, while plots continue to increase slightly with small fluctuations for the remaining 43ns, although never reaching a real plateau. The behavior suggests the systems to be stable enough despite the presence of broken chains (γ subunit, αTP).

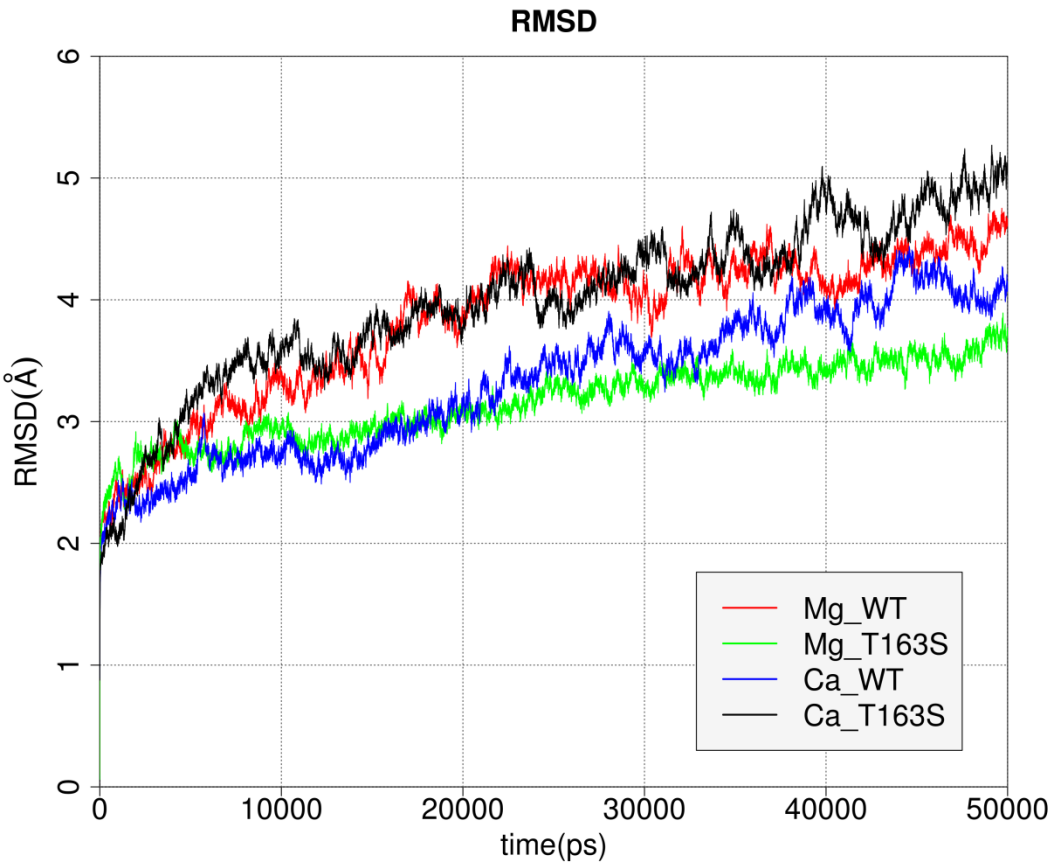

Figure 11 Root mean square deviation of coordinates for non-hydrogen atoms as a function of simulation time. Calculation was performed during 50 ns of MD simulation. The x-axis represents the simulation time (ns) and the y-axis the backbone movement (Å).

3.2.4 Root Mean Square Fluctuation

Root Mean Square Fluctuation (RMSF) shows the fluctuation of each residue in comparison to the average structure of the molecular dynamics. RMSF gives information about the mobility of the complex considering each single protein residue.

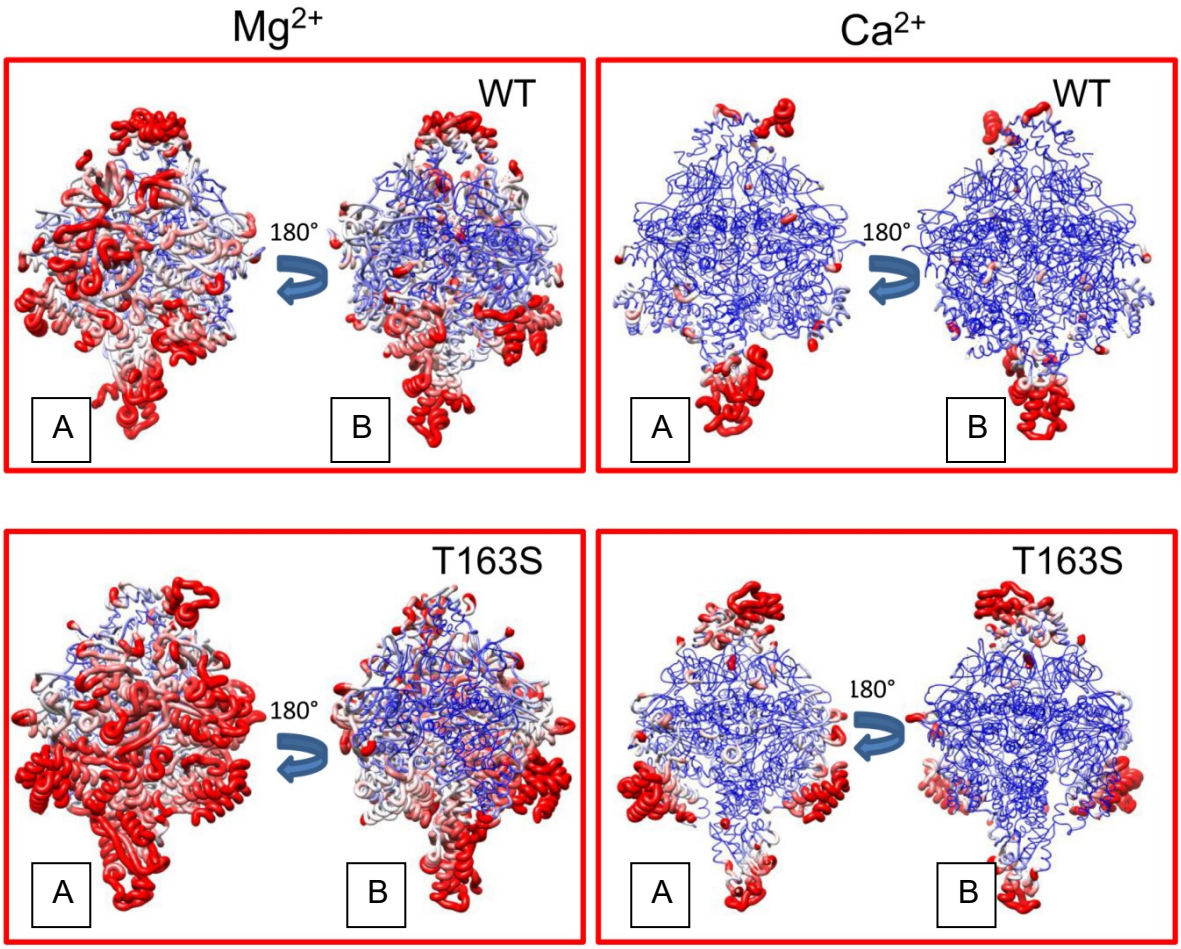

Figure 12. Backbone colouring and thickness correspond to RMSF calculated for each residue. Blue represents residues with RMSF ≤ 4Å while red is for ≥ 5,5 Å. The same range of RMSF is highlighted with the increase of the backbone thickness.

The RMSF analysis (Fig. 12) shows a clear difference in the mobility between the structure after binding Mg^{2+} or Ca^{2+}. The complex appears more flexible when bound to Mg^{2+} while, the binding of Ca^{2+} results in an higher stiffness of the structure. The average value of RMSF is 4.8 Å for both the Mg^{2+} binding system WT and T163S mutant while the structures binding Ca^{2+} have an average RMSD of 3.6 in the WT and 3.9 in the T163S. Furthermore the empty catalytic site (on the B structures of the boxes of Fig.12, and Fig 13 c) show a higher stiffness compared with the β-subunits in TP and DP conformations.

Of particular interest is the behaviour of the OSCP subunit in the MD. The partial OSCP chain remains firmly anchored to F_1 with its C-terminal tail (residues 112-146) freely fluctuating through the simulation box. Considering that the mobility of OSCP region 1-112 changes significantly in the dynamics (Fig. 13a) , and in particular in the Ca^{2+} WT

were the OSCP results “blocked” (average RMSF 4.0 Å), compared with Mg^{2+} binding complexes (WT average RMSF 5.2 Å, and T163S average RMSF 4.6 Å) and the Ca^{2+} T163S mutant (average RMSF 4.9 Å), respectively. The interactions between OSCP and the crown region of αβ subunits appears highly flexible and affected by the cation occupying the Me^{2+} metal binding site and by the T163S mutant.

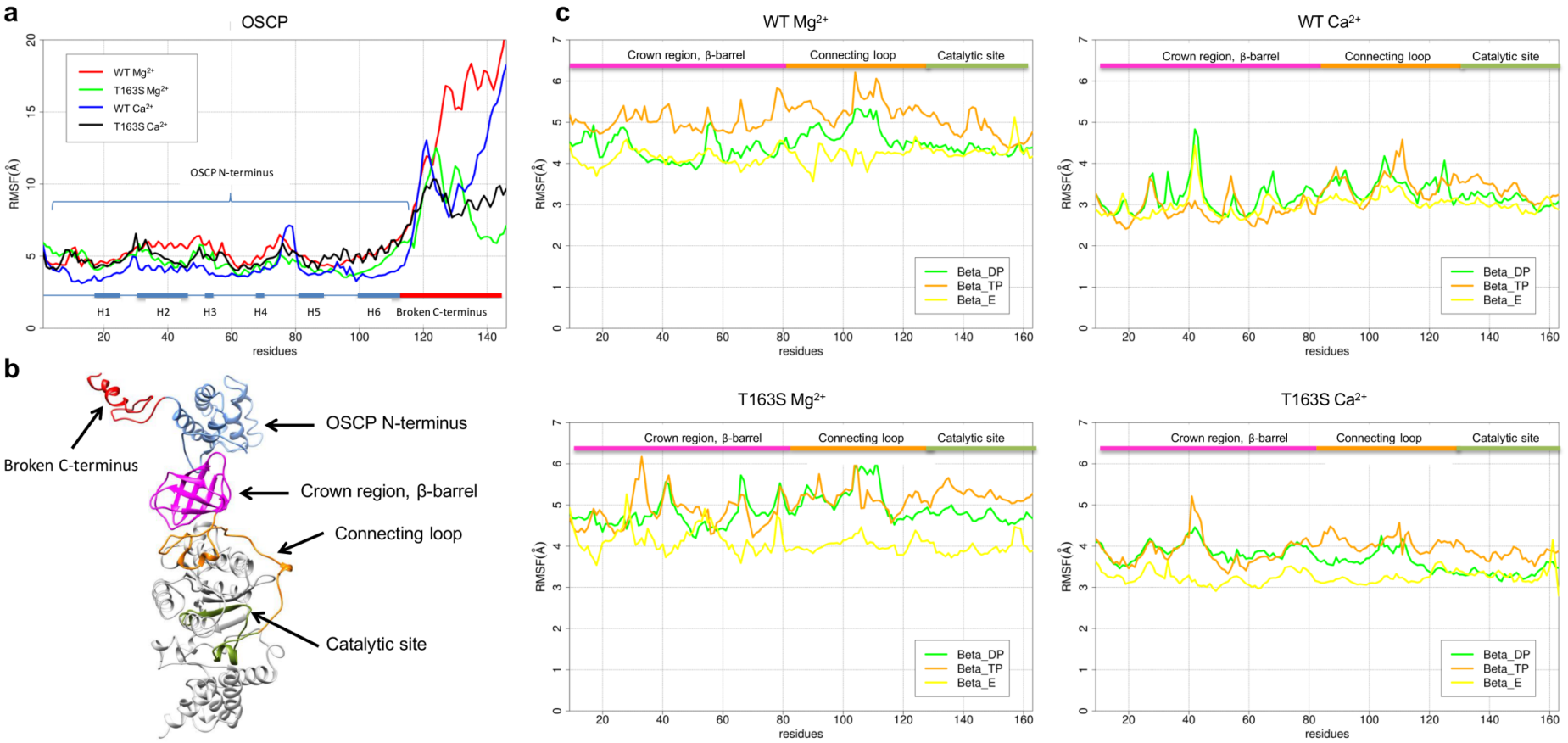

Figure 13 a) The plot show the RMSF values of OSCP interacting with wild-type (WT) and T163S mutant β subunits binding Mg^{2+} and Ca^{2+}. Rectangles below the graphs indicate the position of the α-helices (H) of OSCP and the C-terminus region. b) Focus on the structural regions of the β subunit and OSCP. c) The plots show the RMSF values of wild-type (WT) and T163S mutant of β subunit region 9-163, binding Mg^{2+} and Ca^{2+}.

3.2.5 Investigation of the OSCP crown region interactions

The interactions between OSCP and the crown region of αβ subunits were investigated using Ring2 (241). Ring2 is a software for the identification of non-covalent bonds in protein structures able to build an interactions network with charge-charge, H-bond, van der Waals, π–π stacking and π–cation interactions. Interactions networks were generated for non-covalent interactions of the four systems every 10 ns. The number of interactions during the dynamics vary between 20 and 46 Fig 14. The types of interactions are mainly van der Waals, charge-charge interactions and H-bonds (Table 3).

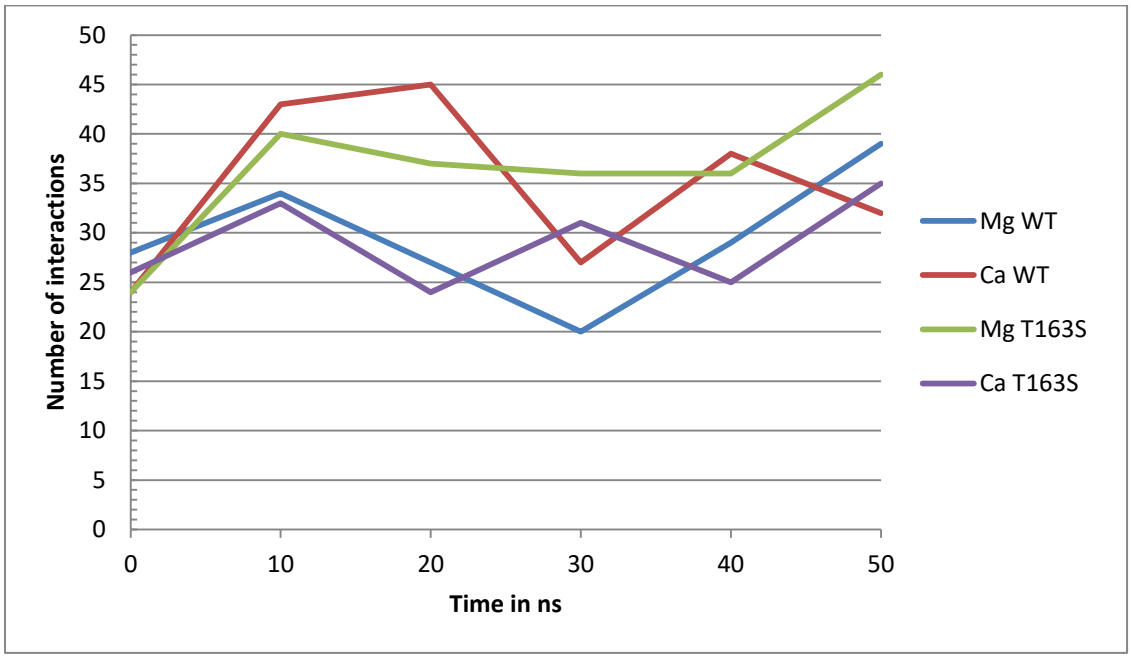

Figure 14 Interactions between OSCP and the crown region of α and β subunits calculate by RING.

Considering the number and the strength of the interactions the main contribution between OSCP and the crown region is the disruption/formation of salt bridges. Inspection of the structure, reveals the presence of charged residues (glutamic, aspartic acid, lysine and asparagine) located at the interface between OSCP and α β subunits (Fig. 15A).

Time (ns)	0	10	20	30	40	50
Mg^{2+} WT	**28**	**34**	**27**	**20**	**29**	**39**
Charge- charge	3	6	8	4	7	11
H-bond	10	13	2	5	2	4
π–π /π–cation	2					1
Van der Waals	13	15	17	11	20	23
Mg^{2+} T163S	**24**	**40**	**37**	**36**	**36**	**46**
Charge- charge	1	6	5	6	5	6
H-bond	9	5	9	7	6	6
π–π /π–cation	2		1	1		
Van der Waals	12	29	22	22	25	34
Ca^{2+} WT	**24**	**43**	**45**	**27**	**38**	**32**
Charge- charge	5	5	5	3	9	5
H-bond	7	8	9	6	8	6
π–π /π–cation	1					
Van der Waals	11	30	31	18	21	21
Ca^{2+} T163S	**26**	**33**	**24**	**31**	**25**	**35**
Charge- charge	4	5	7	6	5	10
H-bond	8	7	6	6	9	10
π–π /π–cation						
Van der Waals	14	21	11	19	11	15

Table 3 Interactions between OSCP and the crown region divided by type and frame.

These residues form a highly dynamic network of salt bridges that rearranges significantly during the simulations. Only the salt bridge between α_E-subunit E13 and OSCP K28 was always found in all the steps of the four simulated systems. Indeed the N-terminus of subunit α_E (in red in Fig. 15B) interacts with helices 1 and 5 of OSCP probably accounts for the high-affinity site (95).

A

B

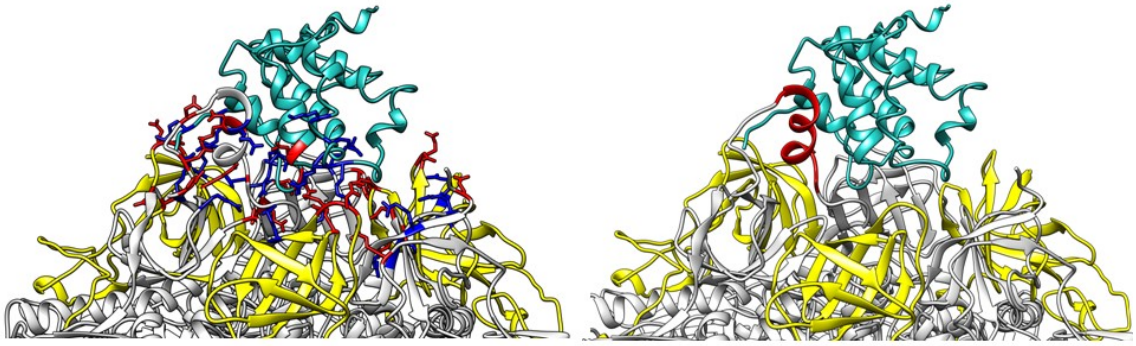

Figure 15 OSCP is colored in light sea-green, α and β subunits in white and yellow, respectively. A) the Positive charged residues (Arg, Lys) are blue and negative charged (Glu, Asp) in red at the interface between OSCP (sea green) and F_1 domain (white). B) The N-terminus of subunit α_E interacting with OSCP is highlighted in red.

To verify if the T163S mutation affects the interaction network of OSCP, complexes binding Ca^{2+} and Mg^{2+} were compared Fig. 16 and Table 4. From the analysis it appears that at T0 35% of the interactions are shared by the WT and T163S mutant when Mg^{2+} is bound while the common interactions between WT and T163S mutant are only 18% when Ca^{2+} is bound, suggesting that the T163S mutation has a stronger effect in the dynamics of OSCP in Ca^{2+}-binding F-ATP synthase.

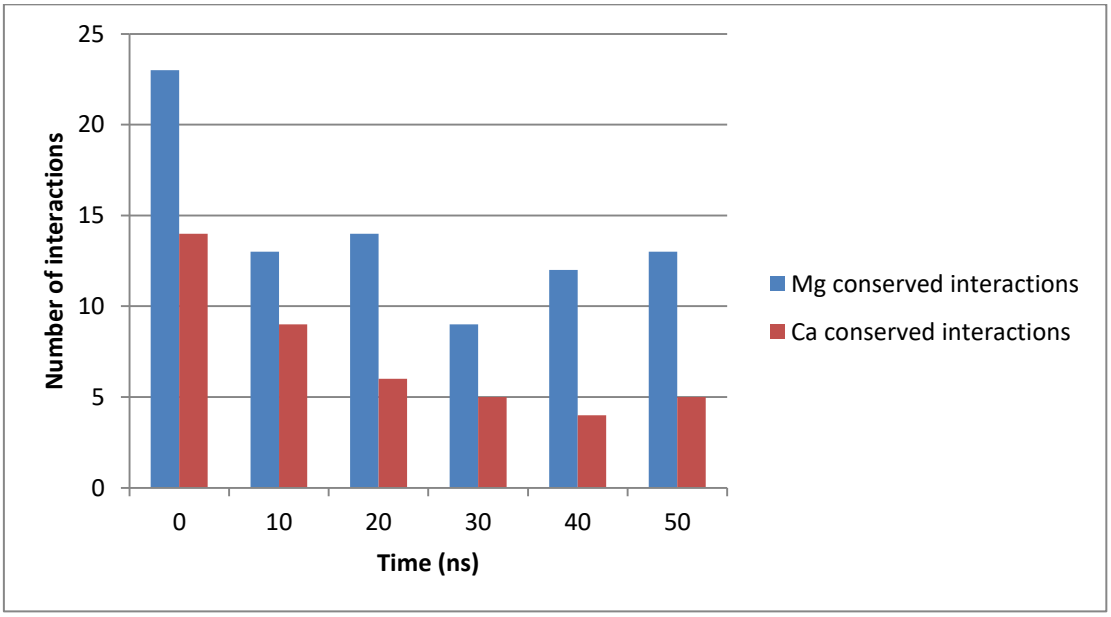

Figure 16 Number of interactions conserved between WT and T163S mutant system binding Ca^{2+} and Mg^{2+}.

Time (ns)	0	10	20	30	40	50
Interactions conserved in Mg^{2+} WT and T163S mutant	**23**	**13**	**14**	**9**	**12**	**13**
Charge- charge	1	3	4	4	3	4
H-bond	8	4				1
π–π /π–cation	2					
Van der Waals	12	6	10	5	9	8
Interactions conserved in Ca^{2+} WT and T163S mutant	**14**	**9**	**6**	**5**	**4**	**5**
Charge- charge	3	4	3	2	3	2
H-bond	4	2		1		
π–π /π–cation						
Van der Waals	7	3	3	2	1	3

Table 4 Interactions between OSCP and the crown region conserved in WT and Mutant binding the same metal divided by type and frame.

3.2.6 The catalytic site-crown region connection loops

The previous results, in keeping with the experimental data of Giorgio *et al.* suggest that a long range transmission of a conformational change between the catalytic site and OSCP is possible. The connection between the mutant residue and the N-terminus β barrel appears in the structure as a long unstructured loop (residues 82-131) (Fig. 17a). We suggest that through this loop a small change due to binding of Ca^{2+} can be amplified at the level of the crown region inducing a conformational change on OSCP. To investigate the behaviour of the connection loops in the four systems we consider the RMSF values of residues 9-163 of β subunit and OSCP. In Fig. 17c the colour and the thickness of the backbone of these regions correspond to the RMSF calculated for each residue of the sequence.

The RMSF values Fig.17c and Fig.13c of the connecting loop and of the crown regions as the complete F_1 domain are strongly influenced by the metal bound. Indeed the β subunit loops fluctuate more when Mg^{2+} is bound to the catalytic site, while in the

presence of Ca^{2+} fluctuations are limited to the β chain connecting loop segment N96-E112 and to the crown region Q39-R44.

Interestingly, the mobility of the loop is dependent on the occupancy of the catalytic site. The fluctuation is higher in presence of ATP and ADP and lower when the site is empty. The RMSF values of the 9-163 regions of the β subunits are reported in Fig. 13c. Comparing the wild type and the mutated complex in the presence of Mg^{2+} the motility appears to be decreased in the β 82-131 loop and crown region in the TP conformation, while the motility increased in the DP conformation. Indeed, we found that the mutation affects the catalytic site, with increased distance of β side chains F418, F424 and Y345 from ADP and decreased surface contact with the adenosine ring. A smaller effect was observed for the ATP binding site, suggesting that the T163S mutation favors ADP release during hydrolysis. Simulations of the T163S mutant with Ca^{2+} show an increase of the mobility of both the DP and TP conformations.

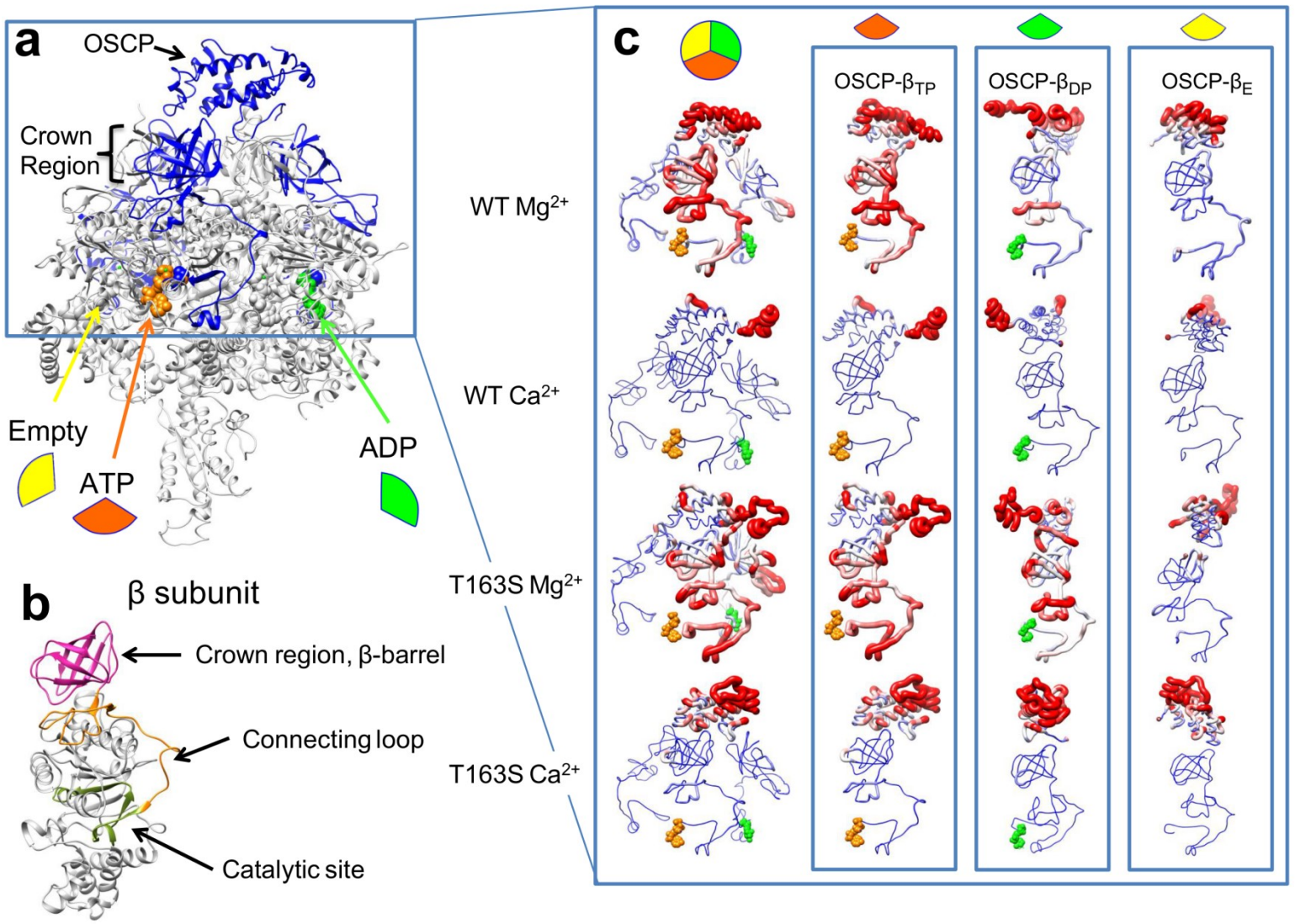

Figure 17 a) F-ATP synthase extrinsic domain highlighting the relative position of OSCP and the β subunits region 9-163 in the empty, ATP- and ADP-bound states. B) Focus on the structure of the β subunit c) The enlargement to the right shows a front view of wild-type (WT) and T163S mutant with Mg^{2+} and Ca^{2+}. The first column shows a structural superposition of all β subunits, while the next 3 columns show front views of individual β subunits in the ATP-bound (TP, *orange wedge*), ADP-bound (DP, *green wedge*) or empty (E, *yellow wedge*) state. Backbone colouring and thickness correspond to RMSF calculated for each residue. Blue represents residues with RMSF ≤ 4 Å while red is for ≥ 5.5 Å. The same range of RMSF is highlighted with the increase of the backbone thickness. Notice the increased rigidity of the Ca^{2+}-containing structures.

3.2.7 Multiple sequence alignment of e, g and b subunits

Homologs of F-ATP synthase subunits from: *Homo sapiens, Bos taurus, Mus musculus, Sarchophilus harrisii, Danio renio, Oreochromis niloticus, Anolis carolinensis, Gallus gallus, Drosophila melanogaster, Saccharomyces cerevisiae* were retrieved by BLAST and aligned using T-COFFEE Fig. 18. These organisms were chosen in order to be representative of eukaryotes in which PTP has more extensively addressed (*Homo sapiens, Bos taurus, Mus musculus, Drosophila melanogaster, Saccharomyces cerevisiae).* I focused on subunits e, g and b because experimental evidence (103) showed their involvement in PTP formation, as well as because subunit e from *Drosophila melanogaster* is markedly different from that of other superior eukaryotes. Indeed, in *Drosophila melanogaster* the C terminus has a unique insertion of 10 residues in a coiled coil region which is rather conserved in other eukaryotes. Subunits g and e present conserved GxxxG motifs, which are known to facilitate oligomerization of membrane proteins (137) and is also thought to permit different subunits to interact with one another.

Surprisingly, both the e and g subunits possess conserved charged residues (Arg 8 in subunit e and Glu 102 in subunit g) in the middle of the transmembrane domain (TM). Charged residues in a TM segment are due to the hydrophobic environment. We speculated that these residues could have a relevant role in the PTP formation. Currently, we are in the process of testing experimentaly the Arg8Ala and Glu102Ala mutations in *Saccharomyces cerevisiae*.

We also propose that the b subunit acts as a transducer of the opening stimulus, which is transferred from the OSCP through a long coiled coil segment. The first TM domain interacts with both subunits e and g (96,242) and is necessary for F-ATP synthase dimerization (42). Based on this evidence, we suggest that the first TM domain is involved in formation and modulation of PTP. The effect of the deletion of the first TM domain in subunit 4 (a *Saccharomyces cerevisiae* homolog of subunit b) is under investigation.

Subunit e

Subunit g

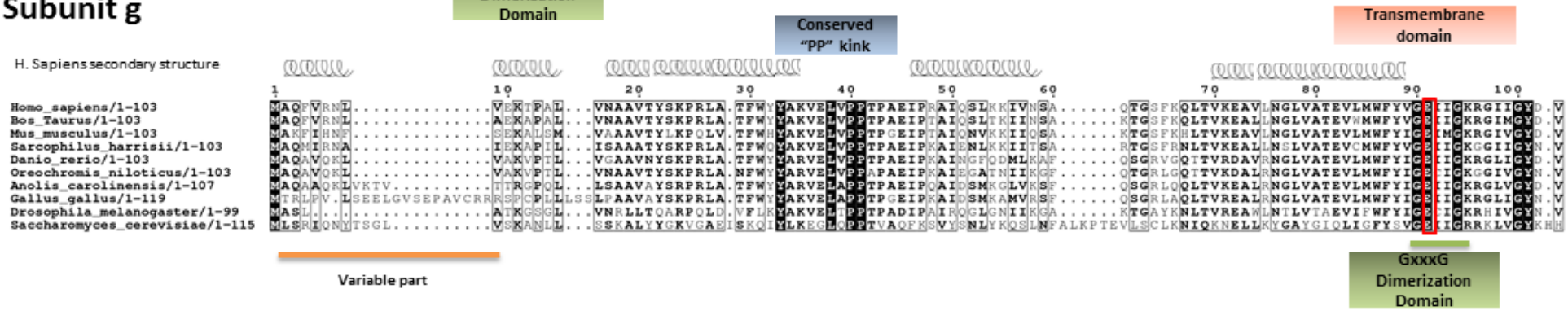

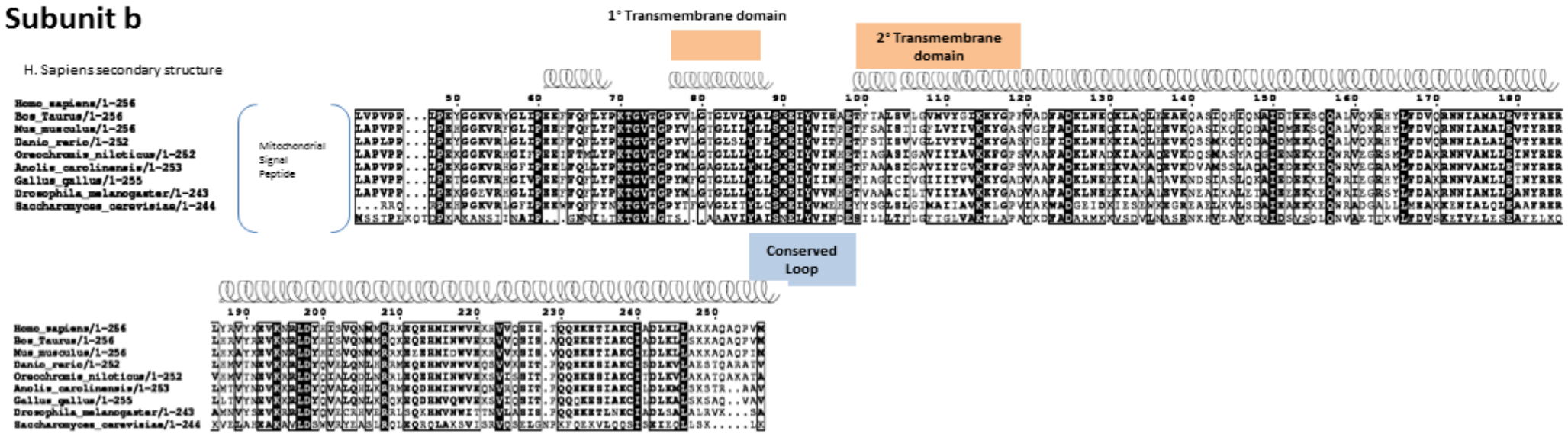

Figure 18 Subunits e, g, and g alignment in *Homo sapiens, Bos taurus, Mus musculus, Sarchophilus harrisii, Danio renio, Oreochromis niloticus, Anolis carolinensis, Gallus gallus, Drosophila melanogaster, Saccharomyces cerevisiae*. Secondary structure of *Homo sapiens,* structural and functional domains are presented on the top, while conserved charged residues found inside transmembrane domains are highlighted by coloured boxes.

3.2.8 F-ATP synthase b subunit phylogenetic tree

I start the phylogenetic analysis from the b subunit. The rationale of this choice rests on the hypothesis that this subunit could mediate the transmission of the opening signal from the catalytic site to the transmembrane domain.

To retrieve homologous sequences from a number of eukaryotic organisms a preliminary search was performed. Multiple searches from different databases shown the "55rp" from Uniprot (243) as the best representative set for the aims of this research. This subgroup was then further filtered with JackHMMER as described in material and method section. A final dataset composed of 228 sequences was finally built.

Interestingly, the final dataset is mainly composed of eukaryotic sequences, with the inclusion of three members of a α-proteobacteria family, i.e. *Rhodospirillum centenum*, *Rhizophagus irregularis* and *Rickettsia prowazekii.*

The b subunit seems to vary among different organisms. In superior eukaryotes and in fungi it presents two transmembrane domains, while in plants and algae only one is recorded. In the case of α-proteobacteria, b subunit is a homodimer formed by two b subunits forming a single TM domain. To better clarify the evolutionary role of these findings, a multiple sequence alignment was performed using Muscle, while an evolutionary tree was built using MrBayes. Based on our calculation, the b subunit clusters fit with the currently accepted evolutionary relationship among organisms. Of particular interest is the localization of the α-proteobacteria clusters which appear to be evolutionarily closer to plants, Oomycota and green algae.

3.2.9 F-ATP synthase e, g and f subunits homologous search

The presence of e, g and f subunits across the 228 organisms was investigated through a phylogenetic analysis. Using human sequences of e, g and f subunits as query, a five

iterations search was performed with JackHMMER. The sequences belonging to the 228 organisms were extracted and used to build up a MSA. The alignment was used in a new search profile based on HMM to mine the proteomes of organisms in which sequence was missing.

The three subunits appear to be highly conserved across the 228 organisms (Fig. 19) with notable exceptions. The three α-proteobacteria miss the three dimerization subunits. This finding, which is not completely unexpected, is in line with the absence of subunits e, g and f in the bacterial F-ATP synthase.

Of interest is the absence of these subunits in an eukaryotic group of fungi, i.e the Oomycotes, where both e and g are missing despite the presence of a conserved *f* subunit. Furthermore, in the green algae *Micromonas sp*. (MICSR) and *Ostreococcus tauri* (OSTTA) only subunit e homologs are missing, while a homolog of g subunit was recovered. Interestingly, it is known in the literature that F-ATP synthase dimer followed a very different evolution path in green algae *Chlamydomonadaceae* family (species not included in this study) (244). In this class, the dimerization process is mediated by a class of unique proteins, i.e the F-ATP synthase-*Associated proteins* (ASA) which have no equivalents in mitochondrial F-ATP synthases from mammals, plants, or fungi (245).

Furthermore, subunits e, g and f were not found in other isolated eukaryotic organisms in the tree. However, based on the data collected in this study we could not decide whether this absence is real or it is due to other reasons, such as incomplete sequencing, poor data available in current databank and possible errors in protein sequence annotation.

Figure 19 shows the phylogenetic tree obtained for the b subunit, with colored boxes indicating the organisms apparently lacking subunits e, g or f. Different color was used for organisms without the complete sequenced genome (see legend for further details). A complete list accounting for organisms in which subunits sequences could not be obtained is reported in Appendix A.

continued on the next page

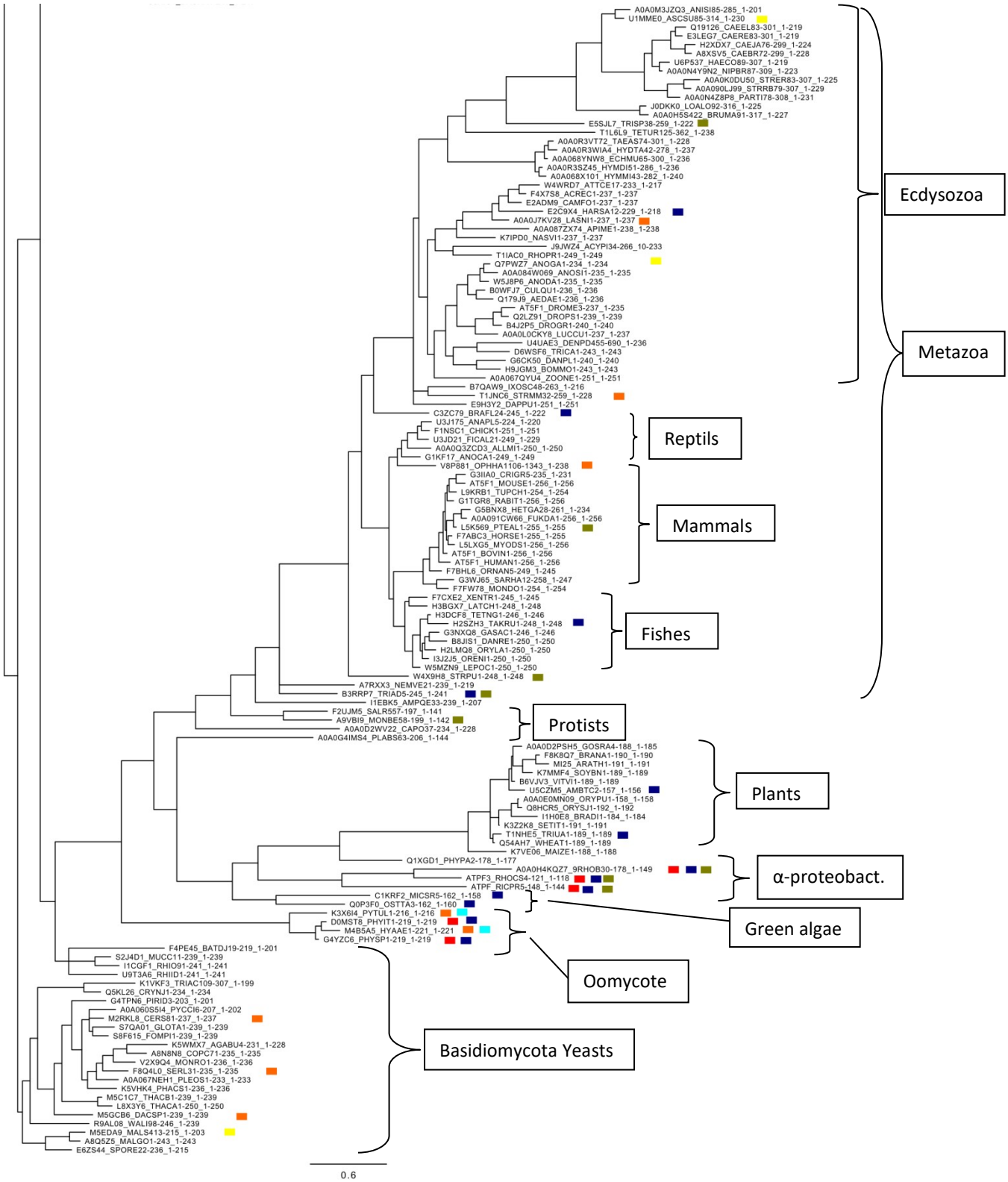

Figure 19 b subunit phylogenetic tree. The identifier for each sequence is in the form UniprotID_TaxonID_startingAA_finalAA of the sequence. Boxes near the name of the organisms indicate if one between e, g, f subunits was not found; g subunit (red if the genome of the organism is completed sequenced, orange if not), e subunit (blue if the genome of the organism is completed sequenced, light blue if not), f subunit (dark green if the genome of the organism is completed sequenced, yellow if not)

3.2.10 Discussion

MD of the F_1-domain and OSCP subunits has provided key insights into a potential mechanism through which Ca^{2+} binding to the catalytic sites is transmitted via OSCP to the peripheral stalk and thence to the inner membrane. Indeed (i) all MDs show a significant stiffening of the F-ATP synthase complex in response to Ca^{2+} binding and rearrangement of Me^{2+} binding site, (ii) the 82-131 unstructured loop may transmit the rearrangement of the Me^{2+} binding site to the crown region, (iii) interactions between the crown region and OSCP are influenced by Ca^{2+} and T163S mutation.

The decreased flexibility of F-ATP synthase after Ca^{2+} binding might transmit mechanical energy to OSCP, which could be transferred to the inner membrane (where the PTP forms) through the lateral stalk (96,242). Consistent with this possibility, combined conformational changes of the peripheral stalk at OSCP/F6 and b subunit at its point of entrance into the membrane have been observed (242). Indeed T163S mutation in presence of Ca^{2+} displayed large fluctuations at the level of OSCP, comparable to those observed for the wild-type protein in the presence of Mg^{2+}. Therefore the mutation appears to prevent the Ca^{2+}-dependent conformational events that, through the connecting loop and the crown region, affect OSCP motility in the wild-type β subunit. These findings may explain the increased resistance to PTP opening of the mutants.

Concerning the F_O region, a phylogenetic tree was built for subunit b and the distribution of subunits e, g and f was studied. We are in the process of testing alanine mutants in yeast for residues eArg8 and gGlu102 and for the deletion of the first TM domin of subunit b.

b subunit displayed great variability in structure and sequence. Form the phylogenetic tree plants, green algae and Oomycetes appear to be the closest eukaryotic b subunit to the α-proteobacteria counterpart. Indeed, plants are the closer sub-kingdom to bacteria possessing all the dimerizations subunits.

In green algae, subunit e homologs are missing and in Oomycetes both e and g subunits are lacking. The genetic code suggests that mitochondria of Oomycota share a direct common ancestor with mitochondria of algae and plants. These clades acquired

mitochondria in a second endosymbiotic event, which occurred later than the acquisition of other eukaryotes (246). These pieces of evidence could justifie a different composition and rearrangement of F-ATP synthase and consequently on the presence of PTP.

Subunits e, g and f are missing as well in other isolated eukaryotes among the tree but it is difficult to distinguish if the reported lack of the subunits is real or is rather due to the limits of the database.

4. Conclusions

Transmembrane proteins play a fundamental role in nutrient translocation and energy conservation (1). In this work I investigated membrane proteins involved in permeability of respectively of PM and IMM.

From my analysis Pendrin SLC26A4 appears to be a 14 transmembrane domain protein. The innovative topology is confirmed by the distribution of the pathological mutations, which cluster in the predicted central loops of the protein and in between the core and the gate domains. One hundred forty-seven pathogenic mutations were mapped on the model. This model fits very well with the known functional important regions and residues of SLC26 family, and will be useful for future work on pendrin function.

For decades the nature of the PTP was a mystery, and only in 2013 dimers of F-ATP synthase were recognized as PTP constituents (4) yet the opening mechanism and the pore forming subunits remain unclear. A T163S mutation in the catalytic β subunit induces resistance to PTP opening. Here we performed MD simulations on the extrinsic region of F-ATP synthase, finding that Ca^{2+} binding in the Me^{2+} binding site of the complex stiffens the structure. Further, catalytic site rearrangement induced from different ion occupancy, as well as the mutation T163S, yields relevant variation of the interaction between F_1 domain and OSCP subunit. We found that the interactions are highly dynamic and mostly dependent on salt bridges. We suggest an unstructured loop between residues 82-131 of the β subunit to transmit to OSCP the structural rearrangement originated from the catalytic site. These pieces of evidence suggest that the Ca^{2+} binding event able to trigger PTP opening occurs in the catalytic sites of F-ATP synthase.

OSCP is known to have a key role in PTP regulation, and CyP D interacts directly with this subunit (59). We speculate that an OSCP conformational change triggered by Ca^{2+} binding could propagate to the lateral stalk and be transmitted to the trans-membrane region.

Future studies will identify the transmembrane PTP components. These investigations appear feasible in the light of the variation in pore conductivity among species, which

suggests that sequence alignment will help identify the critical sites. Our current study has focused on subunits e, g and b due to their localization in the complex and sequence conservation. Specific mutations that may affect PTP opening were collected and their functional effect is currently under analysis.

Proteins homologs of e, g and f subunits were found to be widespread and well conserved in eukaryotes. On the other hand we found that Oomycetes lack of subunit e, and that in green algae both subunits e and g are missing. The b subunit displayed great variability. The plant b subunit show a single transmembrane domain and appear to be closest to their α-proteobacteria counterpart. This finding allow us to suggest an ancient evolution for the F-ATP synthase dimerization subunits and, possibly, for the PTP. Further analysis and experimental validation are planned to clarify this aspect.

Both Pendrin and PTP are associated to widespread diseases. Pendrin mutations cause non-syndromic hearing loss and Pendred syndrome (18) while PTP is involved in huge number of pathologies like myocardial ischemia-reperfusion injury, ischemic and traumatic brain damage, muscular dystrophy caused by collagen VI deficiency, amyotrophic lateral sclerosis, acetaminophen hepatotoxicity, hepatocarcinogenesis by 2-acetylaminofluorene, fulminant, death receptor-induced hepatitis and several others (247). Despite their importance for human health the structures of PTP and Pendrin long remained a mystery. This work contributed to shed light on both systems and to increase our understanding of these membrane permeability mechanisms. Due to their pathogenic relevance, these studies can be of help for new treatments.

APPENDIX A – Organisms lacking of subunit e, g and f

e subunits were not found in α-proteobacteria *(Rhodobacterales, Rhodospirillum centenum, Rickettsia prowazekii),* yeasts (*Scheffersomyces stipitis, Candida maltose***,** *Dekkera bruxellensis, Uncinocarpus reesii, Uncinula necator*, *Endocarpon pusillum),* Oomycota (*Phytophthora sojae, Phytophthora infestans, Pythium ultimum, Hyaloperonospora arabidopsidis*), Green algae (*Ostreococcus tauri, Micromonas*), Plants (*Amborella trichopoda, Tricum urartum, Physcomitrella patens subsp. patens*) and Metazoa (*Trichoplax adhaerens, Nematostella vectensis, Gasterosteus aculeatus, Takifugu rubripes, Branchiostoma floridae, Harpegnathos saltator, Lasius niger*).

g subunits were not found in α-proteobacteria *(Rhodobacterales, Rhodospirillum centenum, Rickettsia prowazekii)* yeasts (*Scheffersomyces stipitis, Cyberlindnera jadinii, Ceriporiopsis subvermispora, Serpula lacrymans var. lacrymans, Dacryopinax primogenitus*), Oomycota (*Phytophthora sojae, Phytophthora infestans, Pythium ultimum, Hyaloperonospora arabidopsidis*) and Metazoa (*Ophiophagus hannah*, *Strigamia maritima, Lasius niger)*

f subunits were not found in α-proteobacteria *(Rhodobacterales, Rhodospirillum centenum, Rickettsia prowazekii),* yeasts (*Scheffersomyces stipitis,Gibberella fujikuroi, Colletotrichum gloeosporioides, Meyerozyma guilliermondii, Tuber melanosporum, Arthroderma benhamiae,Uncinula necator, Blumeria graminis f. sp. hordei, Cordyceps military, Malassezia sympodialis),* Plants *(Tricum urartum), Protista (Plasmodiophora brassicae, Monosiga brevicollis)* and Metazoa (*Trichoplax adhaerens, Strongylocentrotus purpuratus, Pteropus alecto, Anopheles gambiae, Ascaris suum).*

5. Bibliography

1. Mansy SS. Membrane Transport in Primitive Cells. Cold Spring Harb Perspect Biol. 2010 Aug 1;2(8):a002188.

2. Ge X, Gunner MR. Unraveling the mechanism of proton translocation in the extracellular half-channel of bacteriorhodopsin. Proteins. 2016 Feb 12;

3. Geertsma ER, Chang Y-N, Shaik FR, Neldner Y, Pardon E, Steyaert J, et al. Structure of a prokaryotic fumarate transporter reveals the architecture of the SLC26 family. Nat Struct Mol Biol. 2015 Oct;22(10):803–8.

4. Giorgio V, von Stockum S, Antoniel M, Fabbro A, Fogolari F, Forte M, et al. Dimers of mitochondrial ATP synthase form the permeability transition pore. Proc Natl Acad Sci USA. 2013 Apr 9;110(15):5887–92.

5. Giorgio V, Burchell V, Schiavone M, Bassot C, Minervini G, Tosatto S, et al. The Ca2 + regulatory site of the permeability transition pore is within the catalytic core of F-ATP synthase. Biochimica et Biophysica Acta (BBA) - Bioenergetics. 2016 Aug;1857, Supplement:e65–6.

6. Lombard J, López-García P, Moreira D. The early evolution of lipid membranes and the three domains of life. Nat Rev Micro. 2012 Jul;10(7):507–15.

7. Carpenter EP, Beis K, Cameron AD, Iwata S. Overcoming the challenges of membrane protein crystallography. Curr Opin Struct Biol. 2008 Oct;18(5):581–6.

8. Fredriksson R, Hägglund M, Olszewski PK, Stephansson O, Jacobsson JA, Olszewska AM, et al. The obesity gene, FTO, is of ancient origin, up-regulated during food deprivation and expressed in neurons of feeding-related nuclei of the brain. Endocrinology. 2008 May;149(5):2062–71.

9. Mount DB, Romero MF. The SLC26 gene family of multifunctional anion exchangers. Pflugers Arch. 2004 Feb;447(5):710–21.

10. Alper SL, Sharma AK. The SLC26 Gene Family of Anion Transporters and Channels. Mol Aspects Med. 2013 Apr;34(2–3):494–515.

11. Choi BY, Kim H-M, Ito T, Lee K-Y, Li X, Monahan K, et al. Mouse model of enlarged vestibular aqueducts defines temporal requirement of Slc26a4 expression for hearing acquisition. J Clin Invest. 2011 Nov;121(11):4516–25.

12. Wangemann P, Nakaya K, Wu T, Maganti RJ, Itza EM, Sanneman JD, et al. Loss of cochlear HCO3- secretion causes deafness via endolymphatic acidification and inhibition of Ca2+ reabsorption in a Pendred syndrome mouse model. Am J Physiol Renal Physiol. 2007 May;292(5):F1345-1353.

13. Yoshida A, Taniguchi S, Hisatome I, Royaux IE, Green ED, Kohn LD, et al. Pendrin is an iodide-specific apical porter responsible for iodide efflux from thyroid cells. J Clin Endocrinol Metab. 2002 Jul;87(7):3356–61.

14. Soleimani M, Greeley T, Petrovic S, Wang Z, Amlal H, Kopp P, et al. Pendrin: an apical Cl-/OH-/HCO3- exchanger in the kidney cortex. Am J Physiol Renal Physiol. 2001 Feb;280(2):F356-364.

15. Everett LA, Morsli H, Wu DK, Green ED. Expression pattern of the mouse ortholog of the Pendred's syndrome gene (Pds) suggests a key role for pendrin in the inner ear. Proc Natl Acad Sci USA. 1999 Aug 17;96(17):9727–32.

16. Yoshida A, Hisatome I, Taniguchi S, Sasaki N, Yamamoto Y, Miake J, et al. Mechanism of iodide/chloride exchange by pendrin. Endocrinology. 2004 Sep;145(9):4301–8.

17. Royaux IE, Wall SM, Karniski LP, Everett LA, Suzuki K, Knepper MA, et al. Pendrin, encoded by the Pendred syndrome gene, resides in the apical region of renal intercalated cells and mediates bicarbonate secretion. Proc Natl Acad Sci USA. 2001 Mar 27;98(7):4221–6.

18. Pryor SP, Madeo AC, Reynolds JC, Sarlis NJ, Arnos KS, Nance WE, et al. SLC26A4/PDS genotype-phenotype correlation in hearing loss with enlargement of the vestibular aqueduct (EVA): evidence that Pendred syndrome and non-syndromic EVA are distinct clinical and genetic entities. J Med Genet. 2005 Feb;42(2):159–65.

19. Morgans ME, Trotter WR. Association of congenital deafness with goitre; the nature of the thyroid defect. Lancet. 1958 Mar 22;1(7021):607–9.

20. Dossena S, Nofziger C, Tamma G, Bernardinelli E, Vanoni S, Nowak C, et al. Molecular and functional characterization of human pendrin and its allelic variants. Cell Physiol Biochem. 2011;28(3):451–66.

21. Scott DA, Wang R, Kreman TM, Andrews M, McDonald JM, Bishop JR, et al. Functional differences of the PDS gene product are associated with phenotypic variation in patients with Pendred syndrome and non-syndromic hearing loss (DFNB4). Hum Mol Genet. 2000 Jul 1;9(11):1709–15.

22. Tsukamoto K, Suzuki H, Harada D, Namba A, Abe S, Usami S. Distribution and frequencies of PDS (SLC26A4) mutations in Pendred syndrome and nonsyndromic hearing loss associated with enlarged vestibular aqueduct: a unique spectrum of mutations in Japanese. Eur J Hum Genet. 2003 Dec;11(12):916–22.

23. Park H-J, Lee S-J, Jin H-S, Lee JO, Go S-H, Jang HS, et al. Genetic basis of hearing loss associated with enlarged vestibular aqueducts in Koreans. Clin Genet. 2005 Feb;67(2):160–5.

24. Albert S, Blons H, Jonard L, Feldmann D, Chauvin P, Loundon N, et al. SLC26A4 gene is frequently involved in nonsyndromic hearing impairment with enlarged vestibular aqueduct in Caucasian populations. Eur J Hum Genet. 2006 Jun;14(6):773–9.

25. Yang T, Vidarsson H, Rodrigo-Blomqvist S, Rosengren SS, Enerbäck S, Smith RJH. Transcriptional Control of SLC26A4 Is Involved in Pendred Syndrome and Nonsyndromic Enlargement of Vestibular Aqueduct (DFNB4). Am J Hum Genet. 2007 Jun;80(6):1055–63.

26. Yang T, Gurrola JG, Wu H, Chiu SM, Wangemann P, Snyder PM, et al. Mutations of KCNJ10 together with mutations of SLC26A4 cause digenic nonsyndromic hearing loss associated with enlarged vestibular aqueduct syndrome. Am J Hum Genet. 2009 May;84(5):651–7.

27. Zheng J, Shen W, He DZZ, Long KB, Madison LD, Dallos P. Prestin is the motor protein of cochlear outer hair cells. Nature. 2000 Maggio;405(6783):149–55.

28. Saier MH, Eng BH, Fard S, Garg J, Haggerty DA, Hutchinson WJ, et al. Phylogenetic characterization of novel transport protein families revealed by genome analyses. Biochim Biophys Acta. 1999 Feb 25;1422(1):1–56.

29. Azroyan A, Laghmani K, Crambert G, Mordasini D, Doucet A, Edwards A. Regulation of pendrin by pH: dependence on glycosylation. Biochem J. 2011 Feb 15;434(1):61–72.

30. Everett LA, Glaser B, Beck JC, Idol JR, Buchs A, Heyman M, et al. Pendred syndrome is caused by mutations in a putative sulphate transporter gene (PDS). Nat Genet. 1997 Dec;17(4):411–22.

31. Royaux IE, Suzuki K, Mori A, Katoh R, Everett LA, Kohn LD, et al. Pendrin, the protein encoded by the Pendred syndrome gene (PDS), is an apical porter of iodide in the thyroid and is regulated by thyroglobulin in FRTL-5 cells. Endocrinology. 2000 Feb;141(2):839–45.

32. Gillam MP, Sidhaye AR, Lee EJ, Rutishauser J, Stephan CW, Kopp P. Functional Characterization of Pendrin in a Polarized Cell System EVIDENCE FOR PENDRIN-MEDIATED APICAL IODIDE EFFLUX. J Biol Chem. 2004 Mar 26;279(13):13004–10.

33. Gorbunov D, Sturlese M, Nies F, Kluge M, Bellanda M, Battistutta R, et al. Molecular architecture and the structural basis for anion interaction in prestin and SLC26 transporters. Nat Commun. 2014;5:3622.

34. Lu F, Li S, Jiang Y, Jiang J, Fan H, Lu G, et al. Structure and mechanism of the uracil transporter UraA. Nature. 2011 Apr 14;472(7342):243–6.

35. Massari S, Azzone GF. The equivalent pore radius of intact and damaged mitochondria and the mechanism of active shrinkage. Biochim Biophys Acta. 1972;283(1):23–9.

36. Bernardi P, Petronilli V. The permeability transition pore as a mitochondrial calcium release channel: a critical appraisal. J Bioenerg Biomembr. 1996 Apr;28(2):131–8.

37. Bernardi P, Di Lisa F, Fogolari F, Lippe G. From ATP to PTP and Back: A Dual Function for the Mitochondrial ATP Synthase. Circ Res. 2015 May 22;116(11):1850–62.

38. Gray MW. Mitochondrial Evolution. Cold Spring Harb Perspect Biol. 2012 Sep 1;4(9):a011403.

39. Comte J, Maïsterrena B, Gautheron DC. Lipid composition and protein profiles of outer and inner membranes from pig heart mitochondria. Comparison with microsomes. Biochim Biophys Acta. 1976 Jan 21;419(2):271–84.

40. Bernardi P, Rasola A, Forte M, Lippe G. The Mitochondrial Permeability Transition Pore: Channel Formation by F-ATP Synthase, Integration in Signal Transduction, and Role in Pathophysiology. Physiological Reviews. 2015 Oct 1;95(4):1111–55.

41. Davies KM, Strauss M, Daum B, Kief JH, Osiewacz HD, Rycovska A, et al. Macromolecular organization of ATP synthase and complex I in whole mitochondria. PNAS. 2011 Aug 23;108(34):14121–6.

42. Davies KM, Anselmi C, Wittig I, Faraldo-Gómez JD, Kühlbrandt W. Structure of the yeast F1Fo-ATP synthase dimer and its role in shaping the mitochondrial cristae. Proc Natl Acad Sci U S A. 2012 Aug 21;109(34):13602–7.

43. Habersetzer J, Ziani W, Larrieu I, Stines-Chaumeil C, Giraud M-F, Brèthes D, et al. ATP synthase oligomerization: from the enzyme models to the mitochondrial morphology. Int J Biochem Cell Biol. 2013 Jan;45(1):99–105.

44. Strauss M, Hofhaus G, Schröder RR, Kühlbrandt W. Dimer ribbons of ATP synthase shape the inner mitochondrial membrane. The EMBO Journal. 2008 Apr 9;27(7):1154–60.

45. De Stefani D, Raffaello A, Teardo E, Szabò I, Rizzuto R. A forty-kilodalton protein of the inner membrane is the mitochondrial calcium uniporter. Nature. 2011 Aug 18;476(7360):336–40.

46. Crompton M, Heid I. The cycling of calcium, sodium, and protons across the inner membrane of cardiac mitochondria. Eur J Biochem. 1978 Nov 15;91(2):599–608.

47. McCormack JG, Halestrap AP, Denton RM. Role of calcium ions in regulation of mammalian intramitochondrial metabolism. Physiol Rev. 1990 Apr;70(2):391–425.

48. Altschuld RA, Hohl CM, Castillo LC, Garleb AA, Starling RC, Brierley GP. Cyclosporin inhibits mitochondrial calcium efflux in isolated adult rat ventricular cardiomyocytes. Am J Physiol. 1992 Jun;262(6 Pt 2):H1699-1704.

49. Bernardi P. Mitochondrial transport of cations: channels, exchangers, and permeability transition. Physiol Rev. 1999 Oct;79(4):1127–55.

50. Elrod JW, Wong R, Mishra S, Vagnozzi RJ, Sakthievel B, Goonasekera SA, et al. Cyclophilin D controls mitochondrial pore-dependent Ca(2+) exchange, metabolic flexibility, and propensity for heart failure in mice. J Clin Invest. 2010 Oct;120(10):3680–7.

51. Kinnally KW, Campo ML, Tedeschi H. Mitochondrial channel activity studied by patch-clamping mitoplasts. J Bioenerg Biomembr. 21(4):497–506.

52. Petronilli V, Szabò I, Zoratti M. The inner mitochondrial membrane contains ion-conducting channels similar to those found in bacteria. FEBS Lett. 1989 Dec 18;259(1):137–43.

53. Hunter DR, Haworth RA, Southard JH. Relationship between configuration, function, and permeability in calcium-treated mitochondria. J Biol Chem. 1976 Aug 25;251(16):5069–77.

54. Hunter DR, Haworth RA. The Ca2+-induced membrane transition in mitochondria. I. The protective mechanisms. Arch Biochem Biophys. 1979 Jul;195(2):453–9.

55. Haworth RA, Hunter DR. The Ca2+-induced membrane transition in mitochondria. II. Nature of the Ca2+ trigger site. Arch Biochem Biophys. 1979 Jul;195(2):460–7.

56. Hunter DR, Haworth RA. The Ca2+-induced membrane transition in mitochondria. III. Transitional Ca2+ release. Arch Biochem Biophys. 1979 Jul;195(2):468–77.

57. Bernardi P, Di Lisa F. The mitochondrial permeability transition pore: Molecular nature and role as a target in cardioprotection. Journal of Molecular and Cellular Cardiology. 2015 Jan;78:100–6.

58. Matouschek A, Rospert S, Schmid K, Glick BS, Schatz G. Cyclophilin catalyzes protein folding in yeast mitochondria. Proc Natl Acad Sci USA. 1995 Jul 3;92(14):6319–23.

59. Giorgio V, Bisetto E, Soriano ME, Dabbeni-Sala F, Basso E, Petronilli V, et al. Cyclophilin D Modulates Mitochondrial F0F1-ATP Synthase by Interacting with the Lateral Stalk of the Complex. J Biol Chem. 2009 Dec 4;284(49):33982–8.

60. Johnson KM, Chen X, Boitano A, Swenson L, Opipari AW, Glick GD. Identification and validation of the mitochondrial F1F0-ATPase as the molecular target of the immunomodulatory benzodiazepine Bz-423. Chem Biol. 2005 Apr;12(4):485–96.

61. Carraro M, Giorgio V, Šileikytė J, Sartori G, Forte M, Lippe G, et al. Channel formation by yeast F-ATP synthase and the role of dimerization in the mitochondrial permeability transition. J Biol Chem. 2014 Jun 6;289(23):15980–5.

62. Stockum S von, Giorgio V, Trevisan E, Lippe G, Glick GD, Forte MA, et al. F-ATPase of Drosophila melanogaster Forms 53-Picosiemen (53-pS) Channels Responsible for Mitochondrial Ca2+-induced Ca2+ Release. J Biol Chem. 2015 Feb 20;290(8):4537–44.

63. Nathanson L, Gromet-Elhanan Z. Mutations in the β-Subunit Thr159 and Glu184 of the Rhodospirillum rubrumF0F1 ATP Synthase Reveal Differences in Ligands for the Coupled Mg2+- and Decoupled Ca2+-dependent F0F1 Activities. J Biol Chem. 2000 Jan 14;275(2):901–5.

64. Papageorgiou S, Melandri AB, Solaini G. Relevance of divalent cations to ATP-driven proton pumping in beef heart mitochondrial F0F1-ATPase. J Bioenerg Biomembr. 1998 Dec;30(6):533–41.

65. Zoccarato F, Nicholls D. The role of phosphate in the regulation of the independent calcium-efflux pathway of liver mitochondria. Eur J Biochem. 1982 Oct;127(2):333–8.

66. Nicolli A, Petronilli V, Bernardi P. Modulation of the mitochondrial cyclosporin A-sensitive permeability transition pore by matrix pH. Evidence that the pore open-closed probability is regulated by reversible histidine protonation. Biochemistry. 1993 Apr 1;32(16):4461–5.

67. Bernardi P. Modulation of the mitochondrial cyclosporin A-sensitive permeability transition pore by the proton electrochemical gradient. Evidence that the pore can be opened by membrane depolarization. J Biol Chem. 1992 May 5;267(13):8834–9.

68. Basso E, Fante L, Fowlkes J, Petronilli V, Forte MA, Bernardi P. Properties of the permeability transition pore in mitochondria devoid of Cyclophilin D. J Biol Chem. 2005 May 13;280(19):18558–61.

69. Petronilli V, Costantini P, Scorrano L, Colonna R, Passamonti S, Bernardi P. The voltage sensor of the mitochondrial permeability transition pore is tuned by the oxidation-reduction state of vicinal thiols. Increase of the gating potential by oxidants and its reversal by reducing agents. J Biol Chem. 1994 Jun 17;269(24):16638–42.

70. Petronilli V, Cola C, Massari S, Colonna R, Bernardi P. Physiological effectors modify voltage sensing by the cyclosporin A-sensitive permeability transition pore of mitochondria. J Biol Chem. 1993 Oct 15;268(29):21939–45.

71. Eriksson O, Fontaine E, Bernardi P. Chemical modification of arginines by 2,3-butanedione and phenylglyoxal causes closure of the mitochondrial permeability transition pore. J Biol Chem. 1998 May 15;273(20):12669–74.

72. Linder MD, Morkunaite-Haimi S, Kinnunen PKJ, Bernardi P, Eriksson O. Ligand-selective modulation of the permeability transition pore by arginine modification.

Opposing effects of p-hydroxyphenylglyoxal and phenylglyoxal. J Biol Chem. 2002 Jan 11;277(2):937–42.

73. Johans M, Milanesi E, Franck M, Johans C, Liobikas J, Panagiotaki M, et al. Modification of permeability transition pore arginine(s) by phenylglyoxal derivatives in isolated mitochondria and mammalian cells. Structure-function relationship of arginine ligands. J Biol Chem. 2005 Apr 1;280(13):12130–6.

74. Walker JE. The ATP synthase: the understood, the uncertain and the unknown. Biochemical Society Transactions. 2013 Feb 1;41(1):1–16.

75. Walker JE, Fearnley IM, Gay NJ, Gibson BW, Northrop FD, Powell SJ, et al. Primary structure and subunit stoichiometry of F1-ATPase from bovine mitochondria. J Mol Biol. 1985 Aug 20;184(4):677–701.

76. Frasch WD. The participation of metals in the mechanism of the F1-ATPase. Biochimica et Biophysica Acta (BBA) - Bioenergetics. 2000 May 31;1458(2–3):310–25.

77. Rees DM, Montgomery MG, Leslie AGW, Walker JE. Structural evidence of a new catalytic intermediate in the pathway of ATP hydrolysis by F1-ATPase from bovine heart mitochondria. Proc Natl Acad Sci USA. 2012 Jul 10;109(28):11139–43.

78. Selwyn MJ. Model reaction for mitochondrial adenosine triphosphatase. Nature. 1968 Aug 3;219(5153):490–3.

79. Futai M, Nakanishi-Matsui M, Okamoto H, Sekiya M, Nakamoto RK. Rotational catalysis in proton pumping ATPases: from E. coli F-ATPase to mammalian V-ATPase. Biochim Biophys Acta. 2012 Oct;1817(10):1711–21.

80. Noji H, Yasuda R, Yoshida M, Kinosita K. Direct observation of the rotation of F1-ATPase. Nature. 1997 Mar 20;386(6622):299–302.

81. Nam K, Pu J, Karplus M. Trapping the ATP binding state leads to a detailed understanding of the F1-ATPase mechanism. Proc Natl Acad Sci USA. 2014 Dec 16;111(50):17851–6.

82. Watt IN, Montgomery MG, Runswick MJ, Leslie AGW, Walker JE. Bioenergetic cost of making an adenosine triphosphate molecule in animal mitochondria. Proc Natl Acad Sci USA. 2010 Sep 28;107(39):16823–7.

83. Stock D, Leslie AGW, Walker JE. Molecular Architecture of the Rotary Motor in ATP Synthase. Science. 1999 Nov 26;286(5445):1700–5.

84. Meier T, Polzer P, Diederichs K, Welte W, Dimroth P. Structure of the rotor ring of F-Type Na+-ATPase from Ilyobacter tartaricus. Science. 2005 Apr 29;308(5722):659–62.

85. Matthies D, Preiss L, Klyszejko AL, Muller DJ, Cook GM, Vonck J, et al. The c13 Ring from a Thermoalkaliphilic ATP Synthase Reveals an Extended Diameter Due to a Special Structural Region. Journal of Molecular Biology. 2009 May 8;388(3):611–8.

86. Vollmar M, Schlieper D, Winn M, Büchner C, Groth G. Structure of the c14 rotor ring of the proton translocating chloroplast ATP synthase. J Biol Chem. 2009 Jul 3;284(27):18228–35.

87. Pogoryelov D, Yildiz O, Faraldo-Gómez JD, Meier T. High-resolution structure of the rotor ring of a proton-dependent ATP synthase. Nat Struct Mol Biol. 2009 Oct;16(10):1068–73.

88. Fillingame RH, Girvin ME, Zhang Y. Correlations of structure and function in subunit c of Escherichia coli FoF1 ATP synthase. Biochemical Society Transactions. 1995 Nov 1;23(4):760–6.

89. Allegretti M, Klusch N, Mills DJ, Vonck J, Kühlbrandt W, Davies KM. Horizontal membrane-intrinsic α-helices in the stator a-subunit of an F-type ATP synthase. Nature. 2015 Maggio;521(7551):237–40.

90. Cain BD, Simoni RD. Proton translocation by the F1F0ATPase of Escherichia coli. Mutagenic analysis of the a subunit. J Biol Chem. 1989 Feb 25;264(6):3292–300.

91. Kuruma Y, Suzuki T, Ono S, Yoshida M, Ueda T. Functional analysis of membranous Fo-a subunit of F1Fo-ATP synthase by in vitro protein synthesis. Biochem J. 2012 Mar 15;442(3):631–8.

92. Angevine CM, Herold KAG, Vincent OD, Fillingame RH. Aqueous access pathways in ATP synthase subunit a. Reactivity of cysteine substituted into transmembrane helices 1, 3, and 5. J Biol Chem. 2007 Mar 23;282(12):9001–7.

93. Angevine CM, Herold KAG, Fillingame RH. Aqueous access pathways in subunit a of rotary ATP synthase extend to both sides of the membrane. Proc Natl Acad Sci U S A. 2003 Nov 11;100(23):13179–83.

94. Collinson IR, van RaaiJ MJ, Runswick MJ, Fearnley IM, Skehel JM, Orriss GL, et al. ATP Synthase from Bovine Heart Mitochondria. Journal of Molecular Biology. 1994 Sep 29;242(4):408–21.

95. Rees DM, Leslie AGW, Walker JE. The structure of the membrane extrinsic region of bovine ATP synthase. Proc Natl Acad Sci U S A. 2009 Dec 22;106(51):21597–601.

96. Hahn A, Parey K, Bublitz M, Mills DJ, Zickermann V, Vonck J, et al. Structure of a Complete ATP Synthase Dimer Reveals the Molecular Basis of Inner Mitochondrial Membrane Morphology. Mol Cell. 2016 Aug 4;63(3):445–56.

97. Teese MG, Langosch D. Role of GxxxG Motifs in Transmembrane Domain Interactions. Biochemistry. 2015 Aug 25;54(33):5125–35.

98. Arselin G, Giraud M-F, Dautant A, Vaillier J, Brèthes D, Coulary-Salin B, et al. The GxxxG motif of the transmembrane domain of subunit e is involved in the dimerization/oligomerization of the yeast ATP synthase complex in the mitochondrial membrane. Eur J Biochem. 2003 Apr;270(8):1875–84.

99. Everard-Gigot V, Dunn CD, Dolan BM, Brunner S, Jensen RE, Stuart RA. Functional analysis of subunit e of the F1Fo-ATP synthase of the yeast Saccharomyces cerevisiae: importance of the N-terminal membrane anchor region. Eukaryotic Cell. 2005 Feb;4(2):346–55.

100. Soubannier V, Rusconi F, Vaillier J, Arselin G, Chaignepain S, Graves PV, et al. The second stalk of the yeast ATP synthase complex: identification of subunits showing cross-links with known positions of subunit 4 (subunit b). Biochemistry. 1999 Nov 9;38(45):15017–24.

101. Bonora M, Bononi A, De Marchi E, Giorgi C, Lebiedzinska M, Marchi S, et al. Role of the c subunit of the FO ATP synthase in mitochondrial permeability transition. Cell Cycle. 2013 Feb 15;12(4):674–83.

102. Alavian KN, Beutner G, Lazrove E, Sacchetti S, Park H-A, Licznerski P, et al. An uncoupling channel within the c-subunit ring of the F1FO ATP synthase is the mitochondrial permeability transition pore. PNAS. 2014 Jul 22;111(29):10580–5.

103. Carraro M, Giorgio V, Šileikytė J, Sartori G, Forte M, Lippe G, et al. Channel formation by yeast F-ATP synthase and the role of dimerization in the mitochondrial permeability transition. J Biol Chem. 2014 Jun 6;289(23):15980–5.

104. Huberts DHEW, van der Klei IJ. Moonlighting proteins: An intriguing mode of multitasking. Biochimica et Biophysica Acta (BBA) - Molecular Cell Research. 2010 Apr;1803(4):520–5.

105. Ow Y-LP, Green DR, Hao Z, Mak TW. Cytochrome c: functions beyond respiration. Nat Rev Mol Cell Biol. 2008 Jul;9(7):532–42.

106. Hao Z, Duncan GS, Chang C-C, Elia A, Fang M, Wakeham A, et al. Specific ablation of the apoptotic functions of cytochrome C reveals a differential requirement for cytochrome C and Apaf-1 in apoptosis. Cell. 2005 May 20;121(4):579–91.

107. Kluck RM, Ellerby LM, Ellerby HM, Naiem S, Yaffe MP, Margoliash E, et al. Determinants of cytochrome c pro-apoptotic activity. The role of lysine 72 trimethylation. J Biol Chem. 2000 May 26;275(21):16127–33.

108. Koumandou VL, Kossida S. Evolution of the F 0 F 1 ATP Synthase Complex in Light of the Patchy Distribution of Different Bioenergetic Pathways across Prokaryotes. PLOS Comput Biol. 2014 set;10(9):e1003821.

109. Elofsson A, von Heijne G. Membrane protein structure: prediction versus reality. Annu Rev Biochem. 2007;76:125–40.

110. Wallace BA, Cascio M, Mielke DL. Evaluation of methods for the prediction of membrane protein secondary structures. Proc Natl Acad Sci U S A. 1986 Dec;83(24):9423–7.

111. Kyte J, Doolittle RF. A simple method for displaying the hydropathic character of a protein. Journal of Molecular Biology. 1982 May 5;157(1):105–32.

112. von Heijne G. Membrane protein structure prediction. Journal of Molecular Biology. 1992 May 20;225(2):487–94.

113. Krogh A, Larsson B, von Heijne G, Sonnhammer ELL. Predicting transmembrane protein topology with a hidden markov model: application to complete genomes1. Journal of Molecular Biology. 2001 Gennaio;305(3):567–80.

114. Bernsel A, Viklund H, Hennerdal A, Elofsson A. TOPCONS: consensus prediction of membrane protein topology. Nucleic Acids Res. 2009 Jul;37(Web Server issue):W465-468.

115. A guideline to proteome-wide α-helical membrane protein topology predictions - Tsirigos - 2012 - PROTEOMICS - Wiley Online Library [Internet]. [cited 2016 Sep 1]. Available from: http://onlinelibrary.wiley.com/doi/10.1002/pmic.201100495/full

116. Altschul SF, Madden TL, Schäffer AA, Zhang J, Zhang Z, Miller W, et al. Gapped BLAST and PSI-BLAST: a new generation of protein database search programs. Nucleic Acids Res. 1997 Sep 1;25(17):3389–402.

117. Finn RD, Clements J, Eddy SR. HMMER web server: interactive sequence similarity searching. Nucleic Acids Res. 2011 Jul 1;39(Web Server issue):W29–37.

118. Johnson LS, Eddy SR, Portugaly E. Hidden Markov model speed heuristic and iterative HMM search procedure. BMC Bioinformatics. 2010 Aug 18;11(1):431.

119. Söding J, Biegert A, Lupas AN. The HHpred interactive server for protein homology detection and structure prediction. Nucleic Acids Res. 2005 Jul 1;33(Web Server issue):W244-248.

120. Fiser A. Template-Based Protein Structure Modeling. Methods Mol Biol. 2010;673:73–94.

121. Edgar RC. MUSCLE: a multiple sequence alignment method with reduced time and space complexity. BMC Bioinformatics. 2004;5:113.

122. Wang L, Jiang T. On the complexity of multiple sequence alignment. J Comput Biol. 1994;1(4):337–48.

123. Notredame C, Higgins DG, Heringa J. T-Coffee: A novel method for fast and accurate multiple sequence alignment. J Mol Biol. 2000 Sep 8;302(1):205–17.

124. Kozma D, Simon I, Tusnády GE. PDBTM: Protein Data Bank of transmembrane proteins after 8 years. Nucl Acids Res. 2013 Jan 1;41(D1):D524–9.

125. Bernstein FC, Koetzle TF, Williams GJ, Meyer EF, Brice MD, Rodgers JR, et al. The Protein Data Bank: a computer-based archival file for macromolecular structures. J Mol Biol. 1977 May 25;112(3):535–42.

126. Pettersen EF, Goddard TD, Huang CC, Couch GS, Greenblatt DM, Meng EC, et al. UCSF Chimera--a visualization system for exploratory research and analysis. J Comput Chem. 2004 Oct;25(13):1605–12.

127. Benkert P, Tosatto SCE, Schomburg D. QMEAN: A comprehensive scoring function for model quality assessment. Proteins. 2008 Apr;71(1):261–77.

128. De Vivo M, Masetti M, Bottegoni G, Cavalli A. Role of Molecular Dynamics and Related Methods in Drug Discovery. J Med Chem. 2016 May 12;59(9):4035–61.

129. Phillips JC, Braun R, Wang W, Gumbart J, Tajkhorshid E, Villa E, et al. Scalable molecular dynamics with NAMD. J Comput Chem. 2005 Dec;26(16):1781–802.

130. Benkert P, Tosatto SCE, Schomburg D. QMEAN: A comprehensive scoring function for model quality assessment. Proteins. 2008 Apr;71(1):261–77.

131. MacKerell AD, Bashford D, Bellott M, Dunbrack RL, Evanseck JD, Field MJ, et al. All-Atom Empirical Potential for Molecular Modeling and Dynamics Studies of Proteins. J Phys Chem B. 1998 Apr 1;102(18):3586–616.

132. Huelsenbeck JP, Ronquist F. MRBAYES: Bayesian inference of phylogenetic trees. Bioinformatics. 2001 Aug 1;17(8):754–5.

133. Velasco JD. The prior probabilities of phylogenetic trees. Biol Philos. 2008 Jan 17;23(4):455–73.

134. Tusnády GE, Simon I. The HMMTOP transmembrane topology prediction server. Bioinformatics. 2001 Sep 1;17(9):849–50.

135. Cserzo M, Eisenhaber F, Eisenhaber B, Simon I. TM or not TM: transmembrane protein prediction with low false positive rate using DAS-TMfilter. Bioinformatics. 2004 Jan 1;20(1):136–7.

136. Käll L, Krogh A, Sonnhammer ELL. A Combined Transmembrane Topology and Signal Peptide Prediction Method. Journal of Molecular Biology. 2004 Maggio;338(5):1027–36.

137. Viklund H, Elofsson A. OCTOPUS: improving topology prediction by two-track ANN-based preference scores and an extended topological grammar. Bioinformatics. 2008 Aug 1;24(15):1662–8.

138. Bernsel A, Viklund H, Falk J, Lindahl E, von Heijne G, Elofsson A. Prediction of membrane-protein topology from first principles. Proc Natl Acad Sci USA. 2008 May 20;105(20):7177–81.

139. Viklund H, Elofsson A. Best alpha-helical transmembrane protein topology predictions are achieved using hidden Markov models and evolutionary information. Protein Sci. 2004 Jul;13(7):1908–17.

140. Altschul SF, Madden TL, Schäffer AA, Zhang J, Zhang Z, Miller W, et al. Gapped BLAST and PSI-BLAST: a new generation of protein database search programs. Nucl Acids Res. 1997 Sep 1;25(17):3389–402.

141. Notredame C, Higgins DG, Heringa J. T-Coffee: A novel method for fast and accurate multiple sequence alignment. J Mol Biol. 2000 Sep 8;302(1):205–17.

142. Clamp M, Cuff J, Searle SM, Barton GJ. The Jalview Java alignment editor. Bioinformatics. 2004 Feb 12;20(3):426–7.

143. Söding J, Biegert A, Lupas AN. The HHpred interactive server for protein homology detection and structure prediction. Nucleic Acids Res. 2005 Jul 1;33(Web Server issue):W244-248.

144. Liu Y, Richards TA, Aves SJ. Ancient diversification of eukaryotic MCM DNA replication proteins. BMC Evol Biol. 2009;9:60.

145. Schwede T, Kopp J, Guex N, Peitsch MC. SWISS-MODEL: an automated protein homology-modeling server. Nucleic Acids Res. 2003 Jul 1;31(13):3381–5.

146. Sali A, Potterton L, Yuan F, van Vlijmen H, Karplus M. Evaluation of comparative protein modeling by MODELLER. Proteins. 1995 Nov;23(3):318–26.

147. Zhang Y. I-TASSER server for protein 3D structure prediction. BMC Bioinformatics. 2008;9:40.

148. Polticelli F, Basran J, Faso C, Cona A, Minervini G, Angelini R, et al. Lys300 plays a major role in the catalytic mechanism of maize polyamine oxidase. Biochemistry. 2005 Dec 13;44(49):16108–20.

149. Walsh I, Minervini G, Corazza A, Esposito G, Tosatto SCE, Fogolari F. Bluues server: electrostatic properties of wild-type and mutated protein structures. Bioinformatics. 2012 Aug 15;28(16):2189–90.

150. Bassot C, Minervini G, Leonardi E, Tosatto SCE. Mapping pathogenic mutations suggests an innovative structural model for the pendrin (SLC26A4) transmembrane domain. Biochimie. 2017;132:109–20.

151. UniProt: a hub for protein information. Nucleic Acids Res. 2015 Jan 28;43(Database issue):D204–12.

152. UniProt Consortium. Activities at the Universal Protein Resource (UniProt). Nucleic Acids Res. 2014 Jan;42(Database issue):D191-198.

153. Kalli AC, Sansom MSP, Reithmeier RAF. Molecular Dynamics Simulations of the Bacterial UraA H+-Uracil Symporter in Lipid Bilayers Reveal a Closed State and a Selective Interaction with Cardiolipin. PLoS Comput Biol. 2015 Mar 2;11(3):e1004123.

154. Schaechinger TJ, Gorbunov D, Halaszovich CR, Moser T, Kügler S, Fakler B, et al. A synthetic prestin reveals protein domains and molecular operation of outer hair cell piezoelectricity. EMBO J. 2011 Jul 20;30(14):2793–804.

155. Giollo M, Martin AJ, Walsh I, Ferrari C, Tosatto SC. NeEMO: a method using residue interaction networks to improve prediction of protein stability upon mutation. BMC Genomics. 2014 May 20;15(Suppl 4):S7.

156. Laimer J, Hofer H, Fritz M, Wegenkittl S, Lackner P. MAESTRO - multi agent stability prediction upon point mutations. BMC Bioinformatics. 2015;16:116.

157. Yuan Y, Guo W, Tang J, Zhang G, Wang G, Han M, et al. Molecular epidemiology and functional assessment of novel allelic variants of SLC26A4 in non-syndromic hearing loss patients with enlarged vestibular aqueduct in China. PLoS ONE. 2012;7(11):e49984.

158. Chen K, Wang X, Sun L, Jiang H. Screening of SLC26A4, FOXI1, KCNJ10, and GJB2 in bilateral deafness patients with inner ear malformation. Otolaryngol Head Neck Surg. 2012 Jun;146(6):972–8.

159. Taylor JP, Metcalfe RA, Watson PF, Weetman AP, Trembath RC. Mutations of the PDS gene, encoding pendrin, are associated with protein mislocalization and loss of iodide efflux: implications for thyroid dysfunction in Pendred syndrome. J Clin Endocrinol Metab. 2002 Apr;87(4):1778–84.

160. Ishihara K, Okuyama S, Kumano S, Iida K, Hamana H, Murakoshi M, et al. Salicylate restores transport function and anion exchanger activity of missense pendrin mutations. Hear Res. 2010 Dec 1;270(1–2):110–8.

161. Miyagawa M, Nishio S-Y, Usami S-I, Deafness Gene Study Consortium. Mutation spectrum and genotype-phenotype correlation of hearing loss patients caused by SLC26A4 mutations in the Japanese: a large cohort study. J Hum Genet. 2014 May;59(5):262–8.

162. Van Hauwe P, Everett LA, Coucke P, Scott DA, Kraft ML, Ris-Stalpers C, et al. Two frequent missense mutations in Pendred syndrome. Hum Mol Genet. 1998 Jul;7(7):1099–104.

163. de Moraes VCS, dos Santos NZP, Ramos PZ, Svidnicki MCCM, Castilho AM, Sartorato EL. Molecular analysis of SLC26A4 gene in patients with nonsyndromic hearing loss and EVA: identification of two novel mutations in Brazilian patients. Int J Pediatr Otorhinolaryngol. 2013 Mar;77(3):410–3.

164. Ladsous M, Vlaeminck-Guillem V, Dumur V, Vincent C, Dubrulle F, Dhaenens C-M, et al. Analysis of the thyroid phenotype in 42 patients with Pendred syndrome and nonsyndromic enlargement of the vestibular aqueduct. Thyroid. 2014 Apr;24(4):639–48.

165. Pera A, Dossena S, Rodighiero S, Gandía M, Bottà G, Meyer G, et al. Functional assessment of allelic variants in the SLC26A4 gene involved in Pendred syndrome and nonsyndromic EVA. Proc Natl Acad Sci USA. 2008 Nov 25;105(47):18608–13.

166. Pera A, Villamar M, Viñuela A, Gandía M, Medà C, Moreno F, et al. A mutational analysis of the SLC26A4 gene in Spanish hearing-impaired families provides new insights into the genetic causes of Pendred syndrome and DFNB4 hearing loss. Eur J Hum Genet. 2008 Aug;16(8):888–96.

167. Yoon JS, Park H-J, Yoo S-Y, Namkung W, Jo MJ, Koo SK, et al. Heterogeneity in the processing defect of SLC26A4 mutants. J Med Genet. 2008 Jul;45(7):411–9.

168. Rebeh IB, Yoshimi N, Hadj-Kacem H, Yanohco S, Hammami B, Mnif M, et al. Two missense mutations in SLC26A4 gene: a molecular and functional study. Clin Genet. 2010 Jul;78(1):74–80.

169. Huang S, Han D, Yuan Y, Wang G, Kang D, Zhang X, et al. Extremely discrepant mutation spectrum of SLC26A4 between Chinese patients with isolated Mondini deformity and enlarged vestibular aqueduct. J Transl Med. 2011;9:167.

170. Yao G, Chen D, Wang H, Li S, Zhang J, Feng Z, et al. Novel mutations of SLC26A4 in Chinese patients with nonsyndromic hearing loss. Acta Otolaryngol. 2013 Aug;133(8):833–41.

171. Cirello V, Bazzini C, Vezzoli V, Muzza M, Rodighiero S, Castorina P, et al. Molecular and functional studies of 4 candidate loci in Pendred syndrome and nonsyndromic hearing loss. Mol Cell Endocrinol. 2012 Apr 4;351(2):342–50.

172. Pourová R, Janousek P, Jurovcík M, Dvoráková M, Malíková M, Rasková D, et al. Spectrum and frequency of SLC26A4 mutations among Czech patients with early hearing loss with and without Enlarged Vestibular Aqueduct (EVA). Ann Hum Genet. 2010 Jul;74(4):299–307.

173. Chattaraj P, Reimold FR, Muskett JA, Shmukler BE, Chien WW, Madeo AC, et al. Use of SLC26A4 mutation testing for unilateral enlargement of the vestibular aqueduct. JAMA Otolaryngol Head Neck Surg. 2013 Sep;139(9):907–13.

174. Rotman-Pikielny P, Hirschberg K, Maruvada P, Suzuki K, Royaux IE, Green ED, et al. Retention of pendrin in the endoplasmic reticulum is a major mechanism for Pendred syndrome. Hum Mol Genet. 2002 Oct 1;11(21):2625–33.

175. Lazarin GA, Haque IS, Nazareth S, Iori K, Patterson AS, Jacobson JL, et al. An empirical estimate of carrier frequencies for 400+ causal Mendelian variants: results from an ethnically diverse clinical sample of 23,453 individuals. Genet Med. 2013 Mar;15(3):178–86.

176. Park H-J, Shaukat S, Liu X-Z, Hahn SH, Naz S, Ghosh M, et al. Origins and frequencies of SLC26A4 (PDS) mutations in east and south Asians: global implications for the epidemiology of deafness. J Med Genet. 2003 Apr;40(4):242–8.

177. Walsh T, Abu Rayan A, Abu Sa'ed J, Shahin H, Shepshelovich J, Lee MK, et al. Genomic analysis of a heterogeneous Mendelian phenotype: multiple novel alleles for inherited hearing loss in the Palestinian population. Hum Genomics. 2006 Jan;2(4):203–11.

178. Dai P, Stewart AK, Chebib F, Hsu A, Rozenfeld J, Huang D, et al. Distinct and novel SLC26A4/Pendrin mutations in Chinese and U.S. patients with nonsyndromic hearing loss. Physiol Genomics. 2009 Aug 7;38(3):281–90.

179. Wang Q-J, Zhao Y-L, Rao S-Q, Guo Y-F, Yuan H, Zong L, et al. A distinct spectrum of SLC26A4 mutations in patients with enlarged vestibular aqueduct in China. Clin Genet. 2007 Sep;72(3):245–54.

180. Campbell C, Cucci RA, Prasad S, Green GE, Edeal JB, Galer CE, et al. Pendred syndrome, DFNB4, and PDS/SLC26A4 identification of eight novel mutations and possible genotype-phenotype correlations. Hum Mutat. 2001 May;17(5):403–11.

181. Choi BY, Stewart AK, Madeo AC, Pryor SP, Lenhard S, Kittles R, et al. Hypo-functional SLC26A4 variants associated with nonsyndromic hearing loss and enlargement of the vestibular aqueduct: genotype-phenotype correlation or coincidental polymorphisms? Hum Mutat. 2009 Apr;30(4):599–608.

182. Lai C-C, Chiu C-Y, Shiao A-S, Tso Y-C, Wu Y-C, Tu T-Y, et al. Analysis of the SLC26A4 gene in patients with Pendred syndrome in Taiwan. Metabolism. 2007 Sep;56(9):1279–84.

183. Huang C-J, Lei T-H, Chang W-L, Tu T-Y, Shiao A-S, Chiu C-Y, et al. A Novel mutation in the SLC26A4 gene in a Chinese family with Pendred syndrome. Int J Pediatr Otorhinolaryngol. 2013 Sep;77(9):1495–9.

184. Coyle B, Reardon W, Herbrick JA, Tsui LC, Gausden E, Lee J, et al. Molecular analysis of the PDS gene in Pendred syndrome. Hum Mol Genet. 1998 Jul;7(7):1105–12.

185. Reyes S, Wang G, Ouyang X, Han B, Du LL, Yuan HJ, et al. Mutation analysis of SLC26A4 in mainland Chinese patients with enlarged vestibular aqueduct. Otolaryngol Head Neck Surg. 2009 Oct;141(4):502–8.

186. Jiang L, Feng Y, Chen H, He C, Mei L. [An investigation of SLC26A4 gene mutation in nonsydromic hearing impairment in Hunan province of China]. Lin Chung Er Bi Yan Hou Tou Jing Wai Ke Za Zhi. 2010 Jul;24(13):587–91.

187. Dossena S, Rodighiero S, Vezzoli V, Nofziger C, Salvioni E, Boccazzi M, et al. Functional characterization of wild-type and mutated pendrin (SLC26A4), the anion transporter involved in Pendred syndrome. J Mol Endocrinol. 2009 Sep;43(3):93–103.

188. Lai R, Hu P, Zhu F, Zhu G, Vivero R, Peng A, et al. Genetic diagnosis and cochlear implantation for patients with nonsyndromic hearing loss and enlarged vestibular aqueduct. J Laryngol Otol. 2012 Apr;126(4):349–55.

189. Lee HJ, Jung J, Shin JW, Song MH, Kim SH, Lee J-H, et al. Correlation between genotype and phenotype in patients with bi-allelic SLC26A4 mutations. Clin Genet. 2014 Sep;86(3):270–5.

190. Song MH, Shin J-W, Park H-J, Lee K-A, Kim Y, Kim U-K, et al. Intrafamilial phenotypic variability in families with biallelic SLC26A4 mutations. Laryngoscope. 2014 May;124(5):E194-202.

191. Reardon W, OMahoney CF, Trembath R, Jan H, Phelps PD. Enlarged vestibular aqueduct: a radiological marker of pendred syndrome, and mutation of the PDS gene. QJM. 2000 Feb;93(2):99–104.

192. Li XC, Everett LA, Lalwani AK, Desmukh D, Friedman TB, Green ED, et al. A mutation in PDS causes non-syndromic recessive deafness. Nat Genet. 1998 Mar;18(3):215–7.

193. Prasad S, Kölln KA, Cucci RA, Trembath RC, Van Camp G, Smith RJH. Pendred syndrome and DFNB4-mutation screening of SLC26A4 by denaturing high-performance liquid chromatography and the identification of eleven novel mutations. Am J Med Genet A. 2004 Jan 1;124A(1):1–9.

194. Landa P, Differ A-M, Rajput K, Jenkins L, Bitner-Glindzicz M. Lack of significant association between mutations of KCNJ10 or FOXI1 and SLC26A4 mutations in pendred syndrome/enlarged vestibular aqueducts. BMC Medical Genetics. 2013 Aug 21;14(1):85.

195. Babanejad M, Fattahi Z, Bazazzadegan N, Nishimura C, Meyer N, Nikzat N, et al. A comprehensive study to determine heterogeneity of autosomal recessive nonsyndromic hearing loss in Iran. Am J Med Genet A. 2012 Oct;158A(10):2485–92.

196. Shearer AE, Eppsteiner RW, Booth KT, Ephraim SS, Gurrola J, Simpson A, et al. Utilizing ethnic-specific differences in minor allele frequency to recategorize reported pathogenic deafness variants. Am J Hum Genet. 2014 Oct 2;95(4):445–53.

197. Chai Y, Huang Z, Tao Z, Li X, Li L, Li Y, et al. Molecular etiology of hearing impairment associated with nonsyndromic enlarged vestibular aqueduct in East China. Am J Med Genet A. 2013 Sep;161A(9):2226–33.

198. López-Bigas N, Melchionda S, de Cid R, Grifa A, Zelante L, Govea N, et al. Identification of five new mutations of PDS/SLC26A4 in Mediterranean families with hearing impairment. Hum Mutat. 2001 Dec;18(6):548.

199. Fugazzola L, Cerutti N, Mannavola D, Crino A, Cassio A, Gasparoni P, et al. Differential diagnosis between Pendred and pseudo-Pendred syndromes: clinical, radiologic, and molecular studies. Pediatr Res. 2002 Apr;51(4):479–84.

200. Blons H, Feldmann D, Duval V, Messaz O, Denoyelle F, Loundon N, et al. Screening of SLC26A4 (PDS) gene in Pendred's syndrome: a large spectrum of mutations in France and phenotypic heterogeneity. Clin Genet. 2004 Oct;66(4):333–40.

201. Oh S-H, Choi BY, Son KR, Lee KJ, Chang SO, Kim C-S. Can magnetic resonance imaging provide clues to the inner ear functional status of enlarged vestibular aqueduct subjects with PDS mutation? Otol Neurotol. 2008 Aug;29(5):593–600.

202. Anwar S, Riazuddin S, Ahmed ZM, Tasneem S, Ateeq-ul-Jaleel null, Khan SY, et al. SLC26A4 mutation spectrum associated with DFNB4 deafness and Pendred's syndrome in Pakistanis. J Hum Genet. 2009 May;54(5):266–70.

203. Chen K, Zong L, Liu M, Wang X, Zhou W, Zhan Y, et al. Developing regional genetic counseling for southern Chinese with nonsyndromic hearing impairment: a unique mutational spectrum. J Transl Med. 2014;12:64.

204. Jonard L, Niasme-Grare M, Bonnet C, Feldmann D, Rouillon I, Loundon N, et al. Screening of SLC26A4, FOXI1 and KCNJ10 genes in unilateral hearing impairment with ipsilateral enlarged vestibular aqueduct. Int J Pediatr Otorhinolaryngol. 2010 Sep;74(9):1049–53.

205. Kim M, Kim J, Kim SH, Kim SC, Jeon JH, Lee WS, et al. Hemorrhage in the endolymphatic sac: a cause of hearing fluctuation in enlarged vestibular aqueduct. Int J Pediatr Otorhinolaryngol. 2011 Dec;75(12):1538–44.

206. Adato A, Raskin L, Petit C, Bonne-Tamir B. Deafness heterogeneity in a Druze isolate from the Middle East: novel OTOF and PDS mutations, low prevalence of GJB2 35delG mutation and indication for a new DFNB locus. Eur J Hum Genet. 2000 Jun;8(6):437–42.

207. Han B, Dai P, Qi Q, Wang L, Wang Y, Bian X, et al. [Prenatal diagnosis for hereditary deaf families assisted by genetic testing]. Zhonghua Er Bi Yan Hou Tou Jing Wai Ke Za Zhi. 2007 Sep;42(9):660–3.

208. Hu H, Wu L, Feng Y, Pan Q, Long Z, Li J, et al. Molecular analysis of hearing loss associated with enlarged vestibular aqueduct in the mainland Chinese: a unique SLC26A4 mutation spectrum. J Hum Genet. 2007;52(6):492–7.

209. Cama E, Alemanno MS, Bellacchio E, Santarelli R, Carella M, Zelante L, et al. Identification of a novel mutation in the SLC26A4 gene in an Italian with fluctuating sensorineural hearing loss. Int J Pediatr Otorhinolaryngol. 2009 Oct;73(10):1458–63.

210. Volo T, Sathiyaseelan T, Astolfi L, Guaran V, Trevisi P, Emanuelli E, et al. Hair phenotype in non-syndromic deafness. Int J Pediatr Otorhinolaryngol. 2013 Aug;77(8):1280–5.

211. Kahrizi K, Mohseni M, Nishimura C, Bazazzadegan N, Fischer SM, Dehghani A, et al. Identification of SLC26A4 gene mutations in Iranian families with hereditary hearing impairment. Eur J Pediatr. 2009 Jun;168(6):651–3.

212. Madden C, Halsted M, Meinzen-Derr J, Bardo D, Boston M, Arjmand E, et al. The influence of mutations in the SLC26A4 gene on the temporal bone in a population with enlarged vestibular aqueduct. Arch Otolaryngol Head Neck Surg. 2007 Feb;133(2):162–8.

213. Rendtorff ND, Schrijver I, Lodahl M, Rodriguez-Paris J, Johnsen T, Hansén EC, et al. SLC26A4 mutation frequency and spectrum in 109 Danish Pendred syndrome/DFNB4 probands and a report of nine novel mutations. Clin Genet. 2013 Oct;84(4):388–91.

214. Wu C-C, Yeh T-H, Chen P-J, Hsu C-J. Prevalent SLC26A4 mutations in patients with enlarged vestibular aqueduct and/or Mondini dysplasia: a unique spectrum of mutations in Taiwan, including a frequent founder mutation. Laryngoscope. 2005 Jun;115(6):1060–4.

215. Courtmans I, Mancilla V, Ligny C, Hilbert P, Mansbach AL, Van Maldergem L. Clinical findings and PDS mutations in 15 patients with hearing loss and dilatation of the vestibular aqueduct. J Laryngol Otol. 2007 Apr;121(4):312–7.

216. Gonzalez Trevino O, Karamanoglu Arseven O, Ceballos CJ, Vives VI, Ramirez RC, Gomez VV, et al. Clinical and molecular analysis of three Mexican families with Pendred's syndrome. Eur J Endocrinol. 2001 Jun;144(6):585–93.

217. Kühnen P, Turan S, Fröhler S, Güran T, Abali S, Biebermann H, et al. Identification of PENDRIN (SLC26A4) mutations in patients with congenital hypothyroidism and "apparent" thyroid dysgenesis. J Clin Endocrinol Metab. 2014 Jan;99(1):E169-176.

218. Banghova K, Al Taji E, Cinek O, Novotna D, Pourova R, Zapletalova J, et al. Pendred syndrome among patients with congenital hypothyroidism detected by neonatal screening: identification of two novel PDS/SLC26A4 mutations. Eur J Pediatr. 2008 Jul;167(7):777–83.

219. Ogawa A, Shimizu K, Yoshizaki A, Sato S, Kanda Y, Kumagami H, et al. A case of palmoplantar lichen planus in a patient with congenital sensorineural deafness. Clin Exp Dermatol. 2013 Jan;38(1):30–2.

220. Suzuki H, Oshima A, Tsukamoto K, Abe S, Kumakawa K, Nagai K, et al. Clinical characteristics and genotype-phenotype correlation of hearing loss patients with SLC26A4 mutations. Acta Otolaryngol. 2007 Dec;127(12):1292–7.

221. Dai P, Yuan Y, Huang D, Zhu X, Yu F, Kang D, et al. Molecular etiology of hearing impairment in Inner Mongolia: mutations in SLC26A4 gene and relevant phenotype analysis. J Transl Med. 2008;6:74.

222. Mercer S, Mutton P, Dahl H-HM. Identification of SLC26A4 mutations in patients with hearing loss and enlarged vestibular aqueduct using high-resolution melting curve analysis. Genet Test Mol Biomarkers. 2011 May;15(5):365–8.

223. Bogazzi F, Russo D, Raggi F, Ultimieri F, Berrettini S, Forli F, et al. Mutations in the SLC26A4 (pendrin) gene in patients with sensorineural deafness and enlarged vestibular aqueduct. J Endocrinol Invest. 2004 May;27(5):430–5.

224. Kozma D, Simon I, Tusnády GE. PDBTM: Protein Data Bank of transmembrane proteins after 8 years. Nucl Acids Res. 2013 Jan 1;41(D1):D524–9.

225. Fleishman SJ, Ben-Tal N. Progress in structure prediction of alpha-helical membrane proteins. Curr Opin Struct Biol. 2006 Aug;16(4):496–504.

226. Hunte C, Screpanti E, Venturi M, Rimon A, Padan E, Michel H. Structure of a Na+/H+ antiporter and insights into mechanism of action and regulation by pH. Nature. 2005 Jun 30;435(7046):1197–202.

227. Yamashita A, Singh SK, Kawate T, Jin Y, Gouaux E. Crystal structure of a bacterial homologue of Na+/Cl--dependent neurotransmitter transporters. Nature. 2005 Sep 8;437(7056):215–23.

228. Screpanti E, Hunte C. Discontinuous membrane helices in transport proteins and their correlation with function. J Struct Biol. 2007 Aug;159(2):261–7.

229. Choi S, Jeon J, Yang J-S, Kim S. Common occurrence of internal repeat symmetry in membrane proteins. Proteins. 2008 Apr;71(1):68–80.

230. Forrest LR, Rudnick G. The rocking bundle: a mechanism for ion-coupled solute flux by symmetrical transporters. Physiology (Bethesda). 2009 Dec;24:377–86.

231. Taylor JP, Metcalfe RA, Watson PF, Weetman AP, Trembath RC. Mutations of the PDS gene, encoding pendrin, are associated with protein mislocalization and loss of iodide efflux: implications for thyroid dysfunction in Pendred syndrome. J Clin Endocrinol Metab. 2002 Apr;87(4):1778–84.

232. Rotman-Pikielny P, Hirschberg K, Maruvada P, Suzuki K, Royaux IE, Green ED, et al. Retention of pendrin in the endoplasmic reticulum is a major mechanism for Pendred syndrome. Hum Mol Genet. 2002 Oct 1;11(21):2625–33.

233. Porra V, Bernier-Valentin F, Trouttet-Masson S, Berger-Dutrieux N, Peix J-L, Perrin A, et al. Characterization and semiquantitative analyses of pendrin expressed in normal and tumoral human thyroid tissues. J Clin Endocrinol Metab. 2002 Apr;87(4):1700–7.

234. Compton ELR, Karinou E, Naismith JH, Gabel F, Javelle A. Low Resolution Structure of a Bacterial SLC26 Transporter Reveals Dimeric Stoichiometry and Mobile Intracellular Domains. J Biol Chem. 2011 Jul 29;286(30):27058–67.

235. Reithmeier RAF, Moraes TF. Solute carriers keep on rockin'. Nat Struct Mol Biol. 2015 Oct;22(10):752–4.

236. Currall B, Rossino D, Jensen-Smith H, Hallworth R. The roles of conserved and nonconserved cysteinyl residues in the oligomerization and function of mammalian prestin. Journal of Neurophysiology. 2011 Nov 1;106(5):2358–67.

237. Bernardi P, Vassanelli S, Veronese P, Colonna R, Szabó I, Zoratti M. Modulation of the mitochondrial permeability transition pore. Effect of protons and divalent cations. J Biol Chem. 1992 Feb 15;267(5):2934–9.

238. Szabó I, Bernardi P, Zoratti M. Modulation of the mitochondrial megachannel by divalent cations and protons. J Biol Chem. 1992 Feb 15;267(5):2940–6.

239. Du Z, Tucker WC, Richter ML, Gromet-Elhanan Z. Assembled F1-(alpha beta) and Hybrid F1-alpha 3beta 3gamma -ATPases from Rhodospirillum rubrum alpha, wild type or mutant beta, and chloroplast gamma subunits. Demonstration of Mg2+versus Ca2+-induced differences in catalytic site structure and function. J Biol Chem. 2001 Apr 13;276(15):11517–23.

240. Carraro M, Bernardi P. Calcium and reactive oxygen species in regulation of the mitochondrial permeability transition and of programmed cell death in yeast. Cell Calcium. 2016 Aug;60(2):102–7.

241. Piovesan D, Minervini G, Tosatto SCE. The RING 2.0 web server for high quality residue interaction networks. Nucl Acids Res. 2016 May 19;gkw315.

242. Zhou A, Rohou A, Schep DG, Bason JV, Montgomery MG, Walker JE, et al. Structure and conformational states of the bovine mitochondrial ATP synthase by cryo-EM. eLife. 2015 Oct 6;4:e10180.

243. Chen C, Natale DA, Finn RD, Huang H, Zhang J, Wu CH, et al. Representative Proteomes: A Stable, Scalable and Unbiased Proteome Set for Sequence Analysis and Functional Annotation. PLOS ONE. 2011 Apr 27;6(4):e18910.

244. Dudkina NV, Sunderhaus S, Braun H-P, Boekema EJ. Characterization of dimeric ATP synthase and cristae membrane ultrastructure from Saccharomyces and Polytomella mitochondria. FEBS Letters. 2006 Jun 12;580(14):3427–32.

245. Lis R van, Mendoza-Hernández G, Groth G, Atteia A. New Insights into the Unique Structure of the F0F1-ATP Synthase from the Chlamydomonad Algae Polytomella sp. and Chlamydomonas reinhardtii. Plant Physiol. 2007 Jun 1;144(2):1190–9.

246. Karlovsky P, Fartmann B. Genetic code and phylogenetic origin of oomycetous mitochondria. J Mol Evol. 1992 Mar;34(3):254–8.

247. Rasola A, Bernardi P. The mitochondrial permeability transition pore and its involvement in cell death and in disease pathogenesis. Apoptosis. 2007 May;12(5):815–33.